POLITECNICO DI TORINO

Master's Degree in Biomedical Engineering

Master's Degree Thesis

Analysis of Intraoperative MER Signals in Pediatric Patients with Dystonia Undergoing DBS of the Globus Pallidus Internus

Supervisor

Prof. LUCA MESIN

Candidate

VALENTINA FORESTIERE

March 2025

Abstract

Dystonia is a movement disorder characterized by abnormal postures and repetitive movements, often treated with Deep Brain Stimulation (DBS) in cases resistant to other therapies. Intraoperative MicroElectrode Recordings (MER) are typically used to guide electrode placement during DBS surgery, but this process remains largely subjective. This study explores an automated method to analyze MER data and identify optimal implantation sites, aiming to improve surgical outcomes.

MER recordings were collected from five pediatric patients undergoing DBS targeting the globus pallidus internus (GPi), with data obtained on three trajectories—anterior, central, and posterior—at multiple depths. Preprocessing involved filtering high-energy interferences and applying an automated spike-sorting pipeline to extract features such as firing rate, firing regularity, and oscillatory activity.

Statistical analysis showed that the selected trajectory was associated with the highest neural activity in terms of number of spikes (131.70 ± 20.13 vs. 98.57 ± 9.55, $p < 0.05$). Analysis of patients with positive outcomes (4 out of the 5 patients of our dataset) at the selected implant depth revealed significantly lower theta peak frequency. GPi neurons of the patient with negative outcome showed higher firing rates (109.43 ± 73.70 Hz vs. 19.90 ± 5.29 Hz, $p < 0.001$) with respect to the neurons of the GPi of the positive outcome group.

These findings show potential for a relationship between features obtained from automatic analysis and the identification of the optimal trajectory and depth for DBS permanent electrode implantation and provide information on possible outcomes.

Table of Contents

List of Tables

List of Figures

Acronyms

DBS
Deep Brain Stimulation

GPi
Globus Pallidus internus

MRI
Magnetic Resonance Imaging

MER
Microelectrode Recording

PD
Parkinson's Disease

HIV
Human Immunodeficiency Virus

CC
Creative Commons

GP
Globus Pallidus

VP
Ventral Posterior nucleus

SNC
Substantia Nigra pars compacta

SNr

Substantia Nigra pars reticulata

MSNs

Medium Spiny Neurons

VTA

Ventral Tegmental Area

EEG

Electroencephalography

EMG

Electromyography

VIM

Ventral Intermediate nucleus

ET

Essential Tremor

IPG

Implantable Pulse Generator

LFP

Local Field Potential

AP

Action Potential

MEA

Microelectrode Array

IIR

Infinite Impulse Response

PCA

Principal Component Analysis

CFD
: Cumulative Distribution Function

BFMDRS
: Burke-Fahn-Marsden Dystonia Rating Scale

BFMMS
: Burke-Fahn-Marsden Movement Scale

BFMDS
: Burke-Fahn-Marsden Disability Scale

SNR
: Signal to Noise Ratio

ISI
: Inter-Spike Interval

CV
: Coefficient of Variation

LV
: Local Variation

BI
: Burst Index

RS
: Rank Surprise

ESM
: Exhaustive Surprise Maximization

PSD
: Power Spectral Density

RMS
: Root Mean Square

NaN
: Not a Number

Chapter 1

Introduction

Dystonia is defined as "a movement disorder characterized by sustained or intermittent muscle contractions causing abnormal, often repetitive, movements, postures, or both. Dystonic movements are typically patterned and twisting, and may be tremulous. Dystonia is often initiated or worsened by voluntary action and associated with overflow muscle activation" [1]. An infographic presenting dystonia is shown in Figure 1.1.

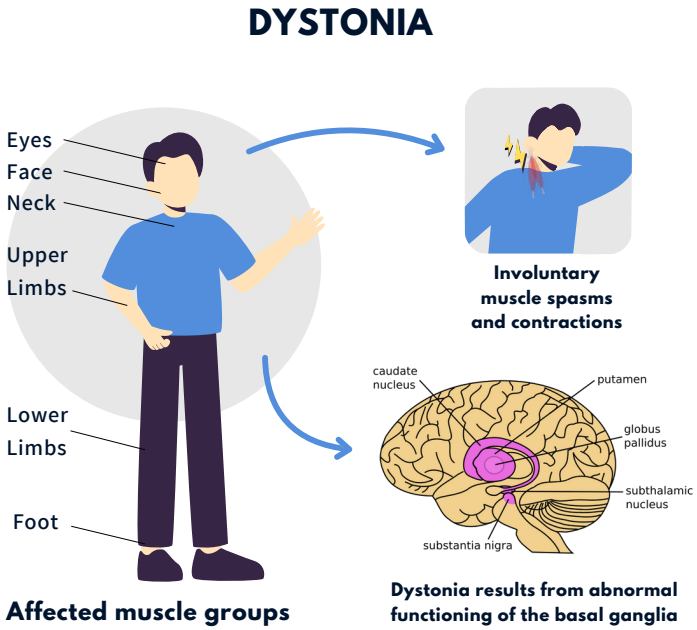

Figure 1.1: An infographic about dystonia, with the main body parts affected by the disorder and relative symptoms. Figure adapted from [2].

Dystonia is among the most prevalent movement disorders in pediatric clinical

settings, which often manifests as a generalized illness affecting the whole body [3], [4]. It can appear in various forms, with symptoms typically affecting multiple body parts at once, complicating both diagnosis and treatment. Dystonia can arise from genetic mutations, as seen in primary dystonias, or from secondary insults to the brain, such as trauma or neurodegenerative diseases.

Although medical therapy remains the first line of treatment, many patients do not respond adequately to medications [5]. As a result, surgical procedures are often investigated and have the potential to significantly reduce caregiving responsibilities and enhance quality of life [6]. From this perspective, Deep Brain Stimulation (DBS), particularly targeting the internal Globus Pallidus (GPi), has taken on an increasingly important role. An illustration of the location of GP in the brain is represented in Figure 1.2.

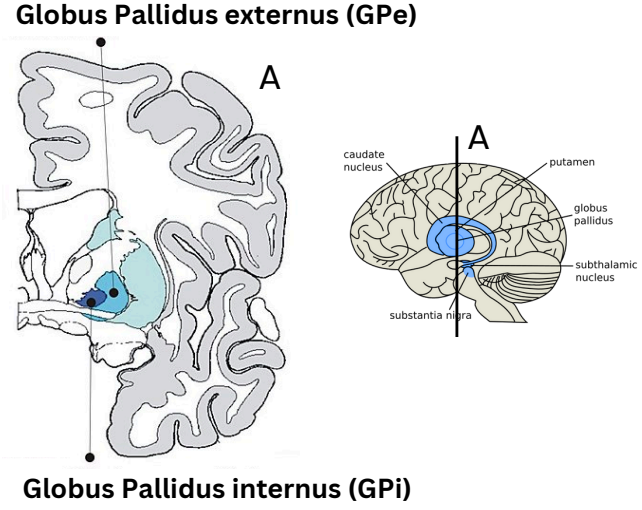

Figure 1.2: Coronal view of the globus pallidus region in the human brain, highlighted in blue. Figure adapted from [7].

For patients with medically refractory dystonia, DBS has frequently yields better results than traditional medications, which may have unfavorable side effects and limited effectiveness. The procedure involves the insertion of brain electrodes into the GPi, with a preoperative Magnetic Resonance Imaging (MRI), spatially registered with respect to the stereotactic frame, used to select the target point in the brain. An example of a Typical DBS implant setup is presented in Figure 1.3 and Figure 1.4.

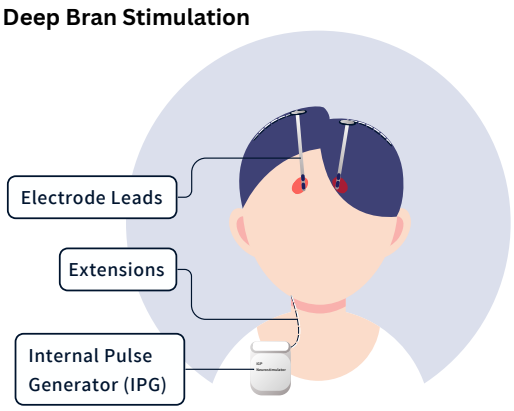

Figure 1.3: Typical deep brain stimulation setup in a pediatric patient, presenting stimulator leads implanted in the brain, extension wires, and neurostimulator. Figure adapted from [8].

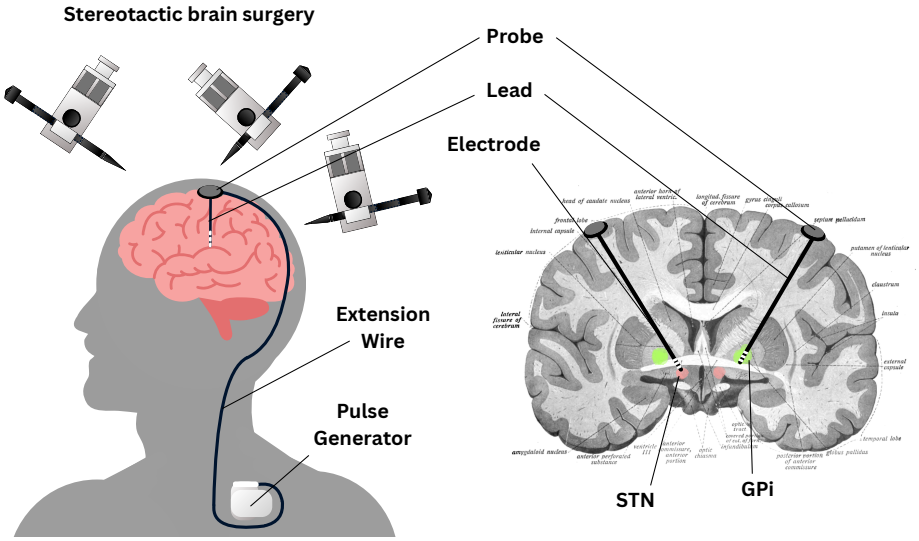

Figure 1.4: Typical DBS surgery setup, correlated by an indication of the main DBS targets in the brain. Figure adapted from [9].

Intraoperative MicroElectrode Recording (MER) is routinely used by surgeons during DBS surgery in order to improve target localization [10]. MER is used to confirm or refine the position of the target to maximize therapeutic benefits and minimize side effects, though this process still relies heavily on manual inspection, requiring substantial expertise and time [11]. Automating the process of determining

the best locations for DBS implantation has been the focus of recent efforts, especially in patients with Parkinson's Disease (PD) [12]. This work aims to expand these efforts by analyzing MER recordings obtained during GPi-DBS in pediatric patients with dystonia, to identify features that could enable automatic classification of the optimal trajectory and implantation depth, as well as offer insights into the potential outcome of the procedure.

Chapter 2

Dystonia

The term "dystonia" was first used in 1911 by Oppenheim to describe patients who presented with muscle spasms that led to distorted postures and rapid, rhythmic movements, characterized by a progressive nature and variable muscle tone ranging from hypotonic to tonic [13]. Over the years, numerous attempts have been made to define dystonia more accurately and comprehensively, culminating in a consensus statement by a Working Group of the International Parkinson and Movement Disorder Society in 2013. This group defined dystonia as: “A movement disorder characterized by sustained or intermittent muscle contractions, repetitive and with a fixed pattern, causing twisting movements and other abnormal postures, often repetitive” [1]. The phrase "with a fixed pattern" describes the recurring activation of the same muscle group, which aids in distinguishing dystonia from other hyperkinetic conditions.

Various conditions have been recognized that cause abnormal movements, postures, or spasms, but are not associated with the specific phenomenology of dystonia. These are termed "pseudo-dystonias" and are characterized by a known or presumed cause, which is thought to differ from the causes of the broader group of dystonias. Examples include Arnold-Chiari malformation, head tilt due to vestibulopathy (inner ear disturbs) or palsy of the trochlear nerve (nerve that sends signals from brain to one of the muscles that controls eye movement), and dystonic tics [1].

2.1 Classification

The classification of dystonia has evolved over the years with different categories that have developed throughout time. Initially, the "DYT" designation was introduced, to indicate chromosomal regions associated with familial disorders [14]. Subsequently, the Task Force of the International Parkinson and Movement Disorder Society recommended a set of criteria for naming genetic movement disorders

[15] to avoid having multiple names for the same disorder or failing to specify an identified gene or locus [14], published in 2016.

Since new genes causing dystonia and other disorders are constantly being found, the lists of confirmed genetic forms are updated every two years. Two primary axes are used in the current clinical classification of dystonia [15]: while **Axis I** describes clinical features such as age of onset, body distribution, temporal pattern, and associated characteristics, **Axis II** focuses on etiology, including idiopathic, hereditary, acquired, structural, and degenerative causes. Albanese et al. (2013) [1] is the source of the information in the following subsections.

2.1.1 Axis I - Clinical Features

Age of onset
This plays an important role both diagnostically and prognostically. For instance, dystonia that manifests in childhood is more often associated with an identifiable cause and has a higher likelihood of evolving from a focal to a generalized form [15]. Initially, a classification into three age groups was proposed (childhood, 0–12 years; adolescence, 12–20 years; adult onset, >20 years) [15], but later, the need for further subdivision became evident. This was due to findings such as the fact that dystonia starting in the first year of life is likely to be a hereditary disorder [14]. Therefore, the need for a more detailed age classification system was identified. The following age groups of onset were thus distinguished:

- **Infancy:** From birth to 2 years
- **Childhood:** 3–12 years
- **Adolescence:** 13–20 years
- **Young adulthood:** 21–40 years
- **Late adulthood:** >40 years

Body distribution
This is particularly relevant for diagnosis and treatment, as it helps to evaluate the evolution of motor symptoms over time. The body regions involved in dystonia include the upper or lower cranial region, cervical region, larynx, trunk, upper or lower limbs. These areas can be affected individually or in various combinations, and the body distribution can change over time, generally with a progressive involvement of areas that were initially unaffected. The spatial progression and, consequently, the spread of dystonia can be monitored through repeated evaluations. The following forms of dystonia can be distinguished:

- **Focal:** Involvement of a single body region.
- **Segmental:** Involvement of two or more contiguous body regions.
- **Multifocal:** Involvement of two or more body regions, which may be contiguous or not.
- **Generalized:** Involvement of the trunk and at least two other body areas.
- **Hemidystonia:** Involvement of multiple body regions, but limited to one side of the body.

Temporal pattern
Another important clinical characteristic both from a prognostic and treatment perspective. Dystonia can evolve with the progression of the disease or show momentary or daily variability depending on voluntary actions, external triggering factors, compensatory phenomena, relieving maneuvers (gestes antagonistes), or psychological state. Hence, variable, diurnal, and paroxysmal forms of dystonia can be distinguished from dystonia that regularly appears under the same circumstances, whether it be task-specific, action-specific, or spontaneous. It is crucial to differentiate between paroxysmal dystonia, in which the same triggering factor may or may not cause an episode, and task-specific dystonia, which is dystonia brought on by the same activity or action and is even predictable. Furthermore, while task-specific dystonia disappears after the triggering activity is finished, paroxysmal dystonia usually continues even after the trigger has stopped.

- **Persistent**: Dystonia that persists with more or less the same intensity throughout the day.
- **Action-specific**: Dystonia that manifests only during a particular activity or task.
- **Diurnal fluctuations**: Dystonia that varies throughout the day, with recognizable circadian fluctuations in onset, severity, and phenomenology.
- **Paroxysmal**: Sudden, self-limiting episodes of dystonia, usually triggered by a specific factor, with a return to the pre-existing neurological state.

The disease course can be static or progressive.

Associated characteristics
Dystonia can present as the sole phenotype, but it can also be associated with other movement disorders. Therefore, it can be further subdivided into three subgroups:

- **Isolated dystonia**: Phenotypes in which dystonia is the only motor feature, except for tremor.
- **Combined dystonia**: Occurs when dystonia presents with other movement disorders, such as parkinsonism, myoclonus, or dyskinesia.
- **Complex dystonia**: Describes syndromes characterized by dystonia associated with other neurological or systemic manifestations. In many of these syndromes, dystonia may not be the primary manifestation of the disease or may be an inconsistent feature, with wide phenotypic variability among individual patients. Examples of such syndromes include neurodegenerative diseases, disorders leading to brain calcification, heavy metal metabolism disorders, neurodegeneration with brain iron accumulation (NBIA), lipid storage diseases, and mitochondrial disorders.

Further details on these three categories can be found in the following articles: Domingo et al. (2020) [16], Weissbach et al. (2021) [17]; Herzog et al. (2021) [18].

When considering the frequency of dystonic signs regardless of the underlying primary condition, dystonia most commonly manifests as a clinical sign in other more common conditions, such as PD, or as a side effect of medications used to treat psychiatric disorders [19] (Figure 2.1).
The characteristics related to Axis I can be summarized in Figure 2.2).

2.1.2 Axis II - Etiology

Despite the growing knowledge of the etiology of dystonia, a complete explanation remains uncertain for most forms. The classification based on etiology will need to be continually updated as new clinical, genetic, and basic science information becomes available [20].

Nervous System Pathology
There is no uniform anatomical description of dystonia. This reflects its heterogeneity and broad spectrum, which includes both degenerative and non-degenerative conditions. Regarding isolated dystonia, many studies report no signs of degeneration or macroscopic irregularities in the brain [21], [22], [23]. As for other forms of dystonia, a relevant discriminant factor is the identification or absence of degeneration, whether macroscopic, microscopic, or at the molecular level. Based on this, three subgroups can be identified: a first subgroup presenting degeneration; a second characterized by static lesions, non-progressive anomalies, or acquired lesions; and a third that is free from any degeneration or structural lesions [1].

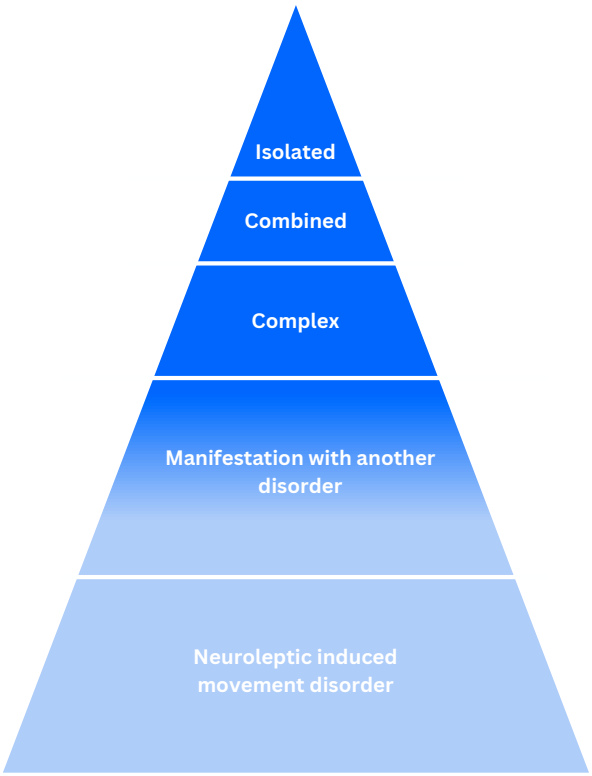

Figure 2.1: Schematic overview of the frequency of dystonia as a clinical sign, regardless of the underlying primary condition Figure adapted from Grütz K., Klein C. (2021) [20].

Hereditary Dystonia

These forms require confirmation of a genetic origin. Based on the type of inheritance, they can be distinguished as autosomal dominant, autosomal recessive, X-linked recessive, and mitochondrial. Most recessive forms, whether autosomal or X-linked, and mitochondrial forms are classified as complex forms; all isolated dystonias with a known genetic cause are, however, autosomal dominant [24].

Acquired Dystonia

Numerous possible causes have been identified [20]:

- **Perinatal brain lesions:** dystonic cerebral palsy, late-onset dystonia.
- **Infections/inflammations:** viral encephalitis, Human Immunodeficiency Virus (HIV) infection, autoimmune causes, tuberculosis, syphilis.

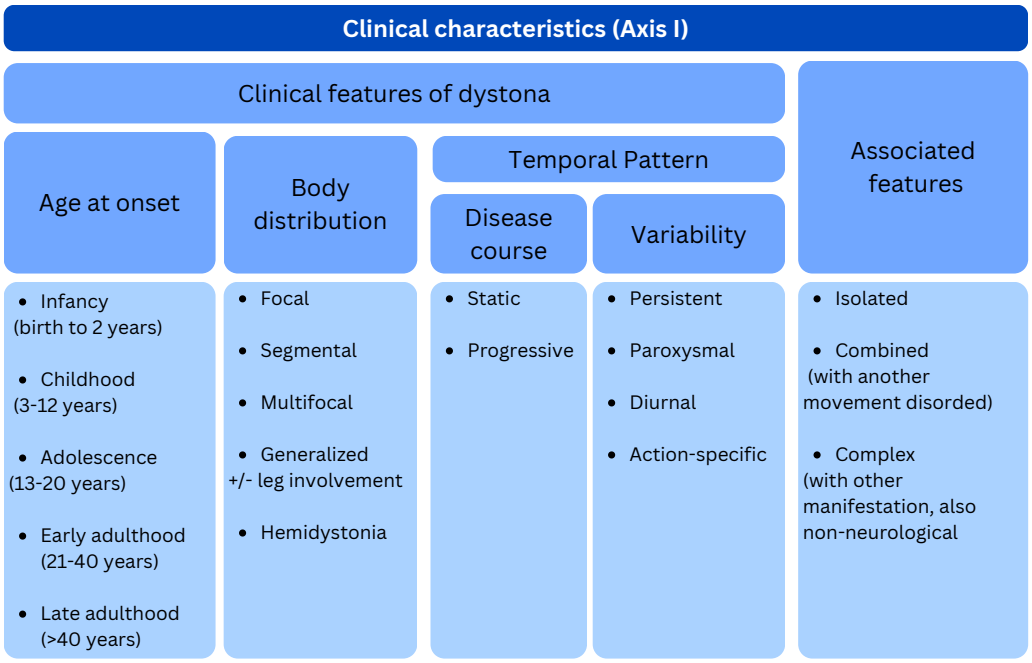

Figure 2.2: Axis I of Dystonia classification based on clinical features. Figure adapted from Grütz K., Klein C. (2021) [20].

– **Medications:** levodopa and dopamine agonists, neuroleptics, anticonvulsants, calcium channel blockers.

– **Toxic:** manganese, cobalt, cyanide.

– **Vascular:** ischemia, hemorrhage, arteriovenous malformations.

– **Neoplastic:** brain tumor, paraneoplastic encephalitis.

– **Brain lesions:** head trauma, brain surgery (including stereotactic ablation), and electrical injuries.

– **Functional.**

Dystonia of Unknown Etiology
This can be further subdivided into sporadic and familial forms. Regarding familial forms, it seems there is a genetic contribution, and with the discovery of new genes involved in the pathogenesis of dystonia (e.g., GNAL [25], ANO3 [26], KMT2B [27]), these subtypes have been included in the hereditary forms group.

The characteristics related to Axis II can be summarized in Figure 2.3).

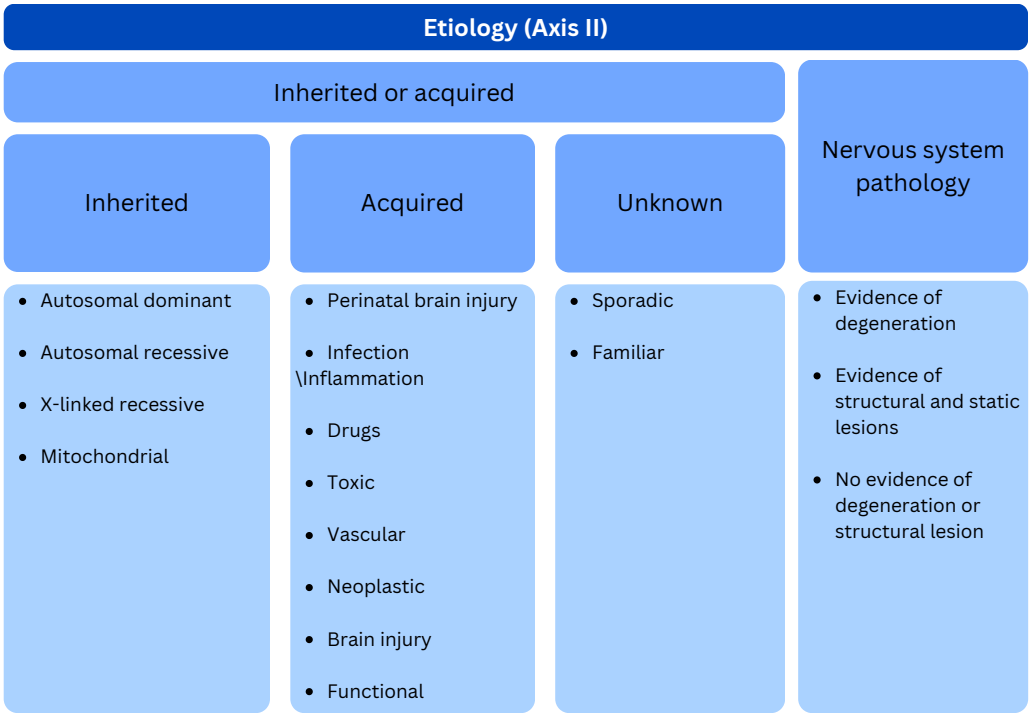

Figure 2.3: The etiological Axis II consists of the contribution of the nervous system, from a genetic or acquired origin of dystonia. Figure adapted from Grütz K., Klein C. (2021) [20].

The clinical classification is significant because it can lead to more defined genetic tests. A specific diagnosis can also help identify a model of disease progression and predict the response to treatment [28]. To date, large-scale genetic association studies have not been conducted, due to both the great heterogeneity of dystonia

and its associated syndromes, as well as the rarity of the disease. Genetic forms explain the condition only in a minority of cases; in fact, most patients do not exhibit a monogenic origin for dystonia. However, it is important to emphasize that models linking the probability of a genetic cause to certain phenotypic expressions do exist.

2.2 Epidemiology

According to the European Union, dystonia affects less than 1 in 2,000 people, making it a rare disease [29]. Recent epidemiological research, however, suggests that the prevalence of isolated dystonia may be somewhat higher, with estimates of 52.7 or 30.9 cases per 100,000 people [30], [31]. Furthermore, a large number of other cases are probably still undiagnosed or incorrectly diagnosed.

While combined dystonias are uncommon, focal dystonia is more prevalent than widespread involvement. Cervical dystonia is the most common type of idiopathic isolated dystonia, occurring in 3–13 people per 100,000 [32]. Dystonia affects both sexes, with a higher incidence in females, and its prevalence rises with age. Differences in geography, race, and ethnicity have also been noted [33].

2.3 Etiopathogenesis

Despite the fact that dystonia is a very diverse neurological condition in terms of both clinical and genetic characteristics, it is becoming more and more evident that para-physiological pathways and common molecular mechanisms underlie this pathology [29]. Indeed, it is evident that dystonia is the result of a malfunctioning network that includes the thalamus, cortex, cerebellum, and basal ganglia. Of particular interest are the cortico-striato-thalamo-cortical and cortico-cerebello-thalamo-cortical circuits, which interact to produce and regulate movement. While neurodegeneration or changes in the development of the cerebellum or basal ganglia have been found in combined and complex forms of dystonia, the majority of studies on isolated dystonia have not found any notable neuronal loss or neuroanatomical changes.

Computed tomography and MRI imaging studies of patients with acquired dystonia have indicated a basal ganglia origin; specifically, focal lesions in the putamen or GPi have been found. According to this model, dystonia is caused by both hyperfunction and hypofunction of the direct and indirect pathways, which leads to increased excitatory stimulation of the motor cortex and decreased GPi inhibition of the thalamus [34]. While imaging studies for genetic and idiopathic

dystonia have revealed subtle abnormalities in all of these brain regions, even in the absence of apparent structural lesions, additional research on lesions has also revealed frequent involvement of the thalamus, cortex, cerebellum, and brainstem in acquired dystonia [35] [36].

It is now possible to determine the temporal and spatial patterns of brain activity in the putamen, GPi, cerebellum, and motor cortex using positron emission tomography with fluorodeoxyglucose. These patterns were found to be different in dystonia patients than in controls, indicating that dystonia may be caused by abnormal connectivity and that these structures are interconnected in a network [37]. At least for certain subtypes of dystonia, the efficacy of GPi-DBS in treating various forms of the disorder has demonstrated the role of the basal ganglia in the disease's pathophysiology [29]. Thus, it is essential to comprehend the structure and operation of the thalamo-cortical-basal ganglia circuits in order to comprehend the pathophysiology of dystonia.

2.3.1 Functional Anatomy of the Basal Ganglia

The basal ganglia are a group of subcortical nuclei responsible for motor control, but they also have additional roles such as motor learning, executive functions, behavior, and emotions [38]. They include the striatum (consisting of the caudate nucleus, putamen, and nucleus accumbens), the STN, the GPi,Globus Pallidus externus (GPe), and Ventral Pallidum (VP)), and the Substantia Nigra (compact part SNc and reticular part SNr) [39] (Figure 2.4). The basal ganglia can be divided into input nuclei, output nuclei, and intrinsic nuclei [38].

Input Nuclei:
Among the input nuclei, we identify the caudate nucleus, the putamen, and the nucleus accumbens; these receive information primarily from cortical, thalamic, and nigral sources. 90% of the neurons present are projection neurons, also known as Medium-Sized Spiny Neurons (MSNs), while the remaining 10% consists of interneurons. All MSNs are inhibitory GABAergic neurons and can be further subdivided based on their projection targets:

- Those innervating the GPe and expressing the D2 dopamine receptor subtype (D2R), which inhibits intracellular adenylate cyclase, thus leading to the indirect pathway.

- Those projecting directly to the GPi and SNr and expressing the D1 dopamine receptor subtype (D1R), which activates adenylate cyclase signaling, leading to the direct pathway.

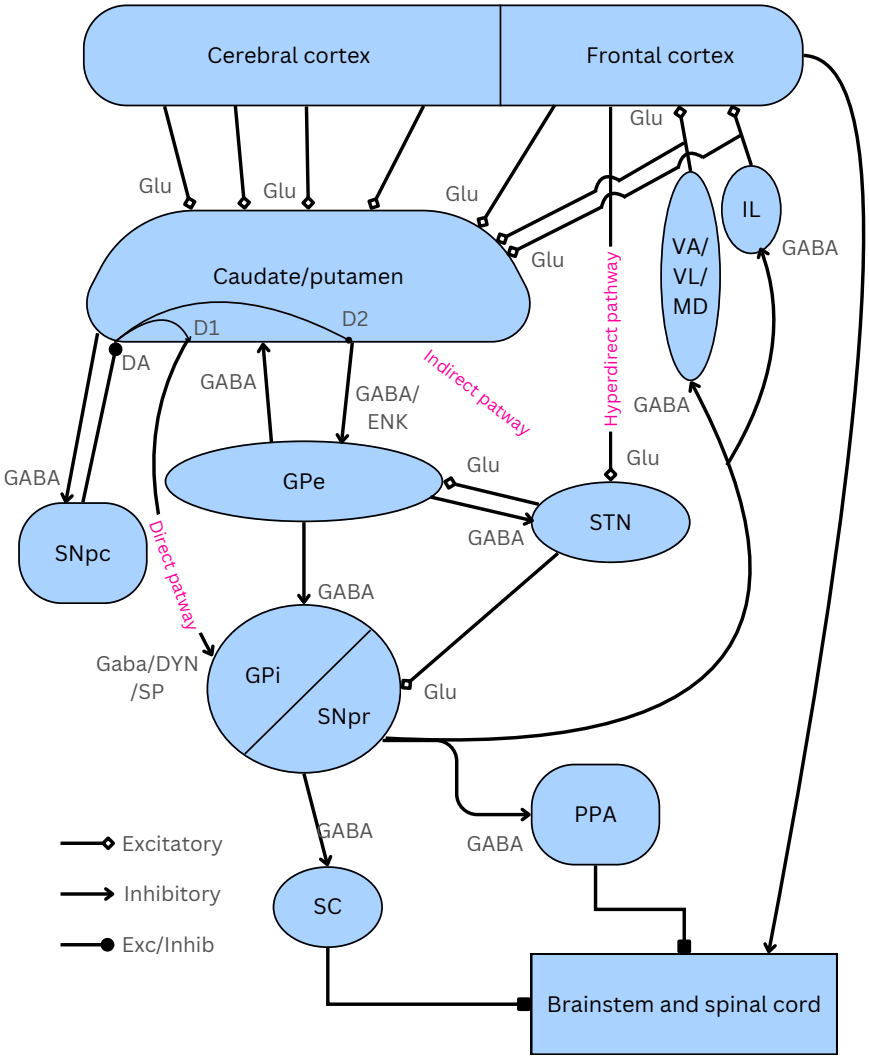

Figure 2.4: A simplified schematic diagram of the basal ganglia circuit adapted from [39].

Output Nuclei:
The output nuclei are represented by GPi and SNr. These consist of inhibitory GABAergic neurons with a high firing rate that are tonically active to inhibit their targets, which are the thalamic and brainstem nuclei. They are inhibited by D1R-type MSNs as part of the direct pathway, while being excited by glutamatergic neurons from the STN [40].

Intrinsic Nuclei:
Among the intrinsic nuclei, we have the GPe, STN, and SNc. The GPe is the

only structure in the indirect pathway and receives inhibitory projections from D2R-type MSNs. It also inhibits the STN via GABAergic connections and, in turn, receives excitatory glutamatergic projections from the STN. The STN, besides being part of the indirect pathway, receiving inhibitory projections from the GPe, and sending excitatory projections to the output nuclei, receives glutamatergic projections directly from the motor, premotor, and frontal cortices, bypassing the input nuclei of the basal ganglia and forming the so-called hyperdirect pathway, a rapid cortical excitation of the inhibitory output of the basal ganglia that leads to a quick halt of an action or decision [40], [41]. The SNc, located in the midbrain, is the source of dopaminergic modulation in the basal ganglia [40].

A schematic representation of these pathways is shown in Figure 2.5

2.4 Diagnosis

To effectively manage dystonia, it is important first to make an accurate diagnosis by identifying the type of dystonia (whether idiopathic, genetic, or acquired) and whether it is isolated or associated with other movement or neurological disorders that may require specific treatments. Most dystonic syndromes present normal laboratory and imaging results, so the diagnosis often relies on identifying the signs of dystonia. However, if idiopathic dystonia is suspected, which typically presents with late onset, no further diagnostic investigations are necessary [33]. It is crucial to distinguish between functional dystonia and idiopathic dystonia, as suggested by the diagram (Figure 2.6).

The first laboratory tests may include measuring copper, ceruloplasmin, and 24-hour urinary copper to rule out Wilson's disease [33]. Additional useful tests include leukocyte enzymes, acanthocytes, lactate, pyruvate, creatine kinase, and antinuclear antibody screening to detect possible systemic disorders associated with neurological conditions. Electrophysiological studies can assess the presence of myopathy or neuropathy [43]. ElectroEncephaloGram (EEG) is mainly performed in patients with paroxysmal (periodically, especially with brief episodes) symptoms or when there is a risk of seizures, while ElectroMyoGraphy(EMG) is generally used when neuromuscular dystonia is suspected, but can also helpful in identifying other dystonic features. If rare conditions such as metabolic, mitochondrial, amino acid, or lysosomal storage disorders are suspected, muscle or skin biopsy and metabolic blood or urine tests may be required. A brain MRI is not always necessary. However, it can help identify structural causes or detect iron or copper metabolism disorders. Additionally, cerebrospinal fluid analysis may be performed if neurotransmitter or metabolic disorders are suspected. Genetic testing is particularly useful for early-onset, combined, or complex phenotypes. If no specific mutation is identified, gene

panels are recommended. In cases with a strong suspicion of genetic etiology but negative standard genetic tests, next-generation exome or whole-genome sequencing may be considered, although these are more complex procedures [33].

2.5 Treatment Options

To date, there is no targeted causal treatment for most forms of dystonia, and therapeutic options primarily include symptomatic treatment. The most suitable choice for each individual case is based on clinical characteristics such as the distribution and severity of symptoms, as well as the etiology [29]; therefore, treatment must be personalized. The goal of symptomatic therapy is to provide relief from abnormal movements or postures, associated pain and discomfort, contractures, or other orthopedic complications resulting from prolonged abnormal postures, as well as medical comorbidities, including neuropsychiatric symptoms [33].

Physical, Occupational and Speech Therapy, and Rehabilitation
It is important to encourage the patient to experiment with sensory tricks or gestures, which can help improve dystonic movements in addition to other treatments. Depending on the type of dystonia, physical therapy, occupational therapy, or speech therapy can also be very helpful. Rehabilitation helps to improve functional capacity, prevent contractures due to persistent or fixed postures, and facilitate sensorimotor retraining [33].

Botulinum Toxin Chemodenervation
Botulinum toxin has revolutionized the treatment of focal dystonias, with serotypes A and B being most commonly used. Injections are routinely administered every 12 weeks, including to the tongue, vocal cords, and masticatory muscles. Proper muscle selection and dosing are critical, as incorrect choices can lead to inadequate response or worsened symptoms, while high doses may cause excessive weakness.

Pharmacotherapy
Oral pharmacotherapy is generally considered for generalized dystonia or in cases of severe disease. In particular, in dopa-responsive dystonia, low-dose levodopa therapy may be effective, also helping to treat other forms of combined dystonia, such as X-linked dystonia-parkinsonism, although with a lesser response. For other forms of dystonia, however, the response is often poor Thomsen2024. An alternative is anticholinergic drugs, which are useful in most types of dystonia and are mainly used for generalized forms, though less frequently for segmental dystonia. They are typically tried in younger patients due to better tolerance compared to older patients, in whom they may induce anticholinergic delirium.

Side effects can include dry mouth, constipation, blurred vision, cognitive changes, hallucinations, and drowsiness. Other treatment options include antidopaminergic therapy, such as antipsychotics or neuroleptics, and dopamine-depleting agents, which are mainly used in late-onset dystonia, though with variable responses and often dominant side effects [29]. Benzodiazepines are used as adjuncts in second or third-line therapy [33].

Non-Invasive Brain Stimulation
This is an emerging area as a potential therapy for dystonia, but it is still in the experimental phase and is mainly used for research purposes. Examples of non-invasive brain stimulation include repetitive transcranial magnetic stimulation and transcranial direct current stimulation [33]. These can be used as a complement to rehabilitation [44].

Surgical Treatments
Among the surgical treatment options are ablation (such as thalamotomy or pallidotomy), focused ultrasound, and DBS. Pallidotomy and thalamotomy were the first effective therapeutic options and are still used in selected patients. There is evidence of effectiveness for focused ultrasound guided by MRI, although there may often be recurrences that require repeated lesions. These procedures are performed unilaterally, as it is unclear whether bilateral use would be safe. DBS is used as an alternative therapy in case of failure of botulinum toxin treatment and works by correcting the network dysfunction that is believed to be the cause of dystonic movement. Compared to focused ultrasound, DBS seems to have fewer side effects, potential reversibility, and the ability to adjust the direction and field of stimulation. In most cases, the target is the GPi, although increasing evidence suggests effectiveness for the STN and thalamus as well. In the past, peripheral denervation was widely used for cervical dystonia; however, it was poorly tolerated, had a high recurrence rate, and many side effects, so it is no longer recommended today.

The various treatment options for dystonia can be summarized in Figure 2.7.

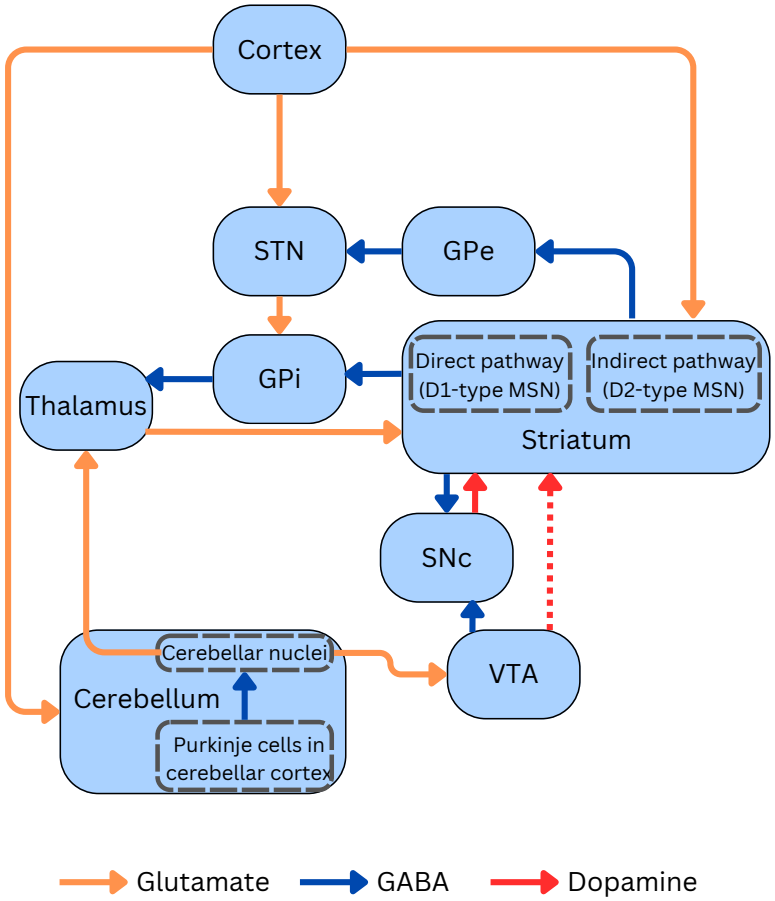

Figure 2.5: A detailed schematic diagram of the dystonia involved circuits. The striatum receives modulatory dopaminergic input from the SNc, which can stimulate the MSN of either the direct or indirect pathway. The direct pathway (MSN type D2R) passes through the GPe and STN, leading to the excitation of GPi neurons that inhibit thalamic neurons and reduce movement. Conversely, stimulation of the direct pathway (MSN type D1R) inhibits GPi neurons, removing the inhibitory input to the thalamus and facilitating movement via excitatory stimulation of the cortex. The involvement of the cerebellum in dystonia is increasingly being considered. GABAergic Purkinje cells in the cerebellar cortex project to the downstream deep cerebellar nuclei, which in turn have direct connections with the basal ganglia through the thalamus. Additionally, GABAergic neurons in the Ventral Tegmental Area (VTA) send inhibitory inputs to dopaminergic neurons in the SNc, altering dopaminergic input to the striatum. The VTA also contains dopaminergic neurons that project directly to the striatum, but they are thought to play a lesser role in motor function (indicated by the dashed red line). Adapted from [29]. Abbreviations: SNc – Substantia Nigra pars compacta, MSN – Medium Spiny Neurons, GPe – External segment of the Globus Pallidus, STN – Subthalamic Nucleus, GPi – Internal segment of the Globus Pallidus, VTA – Ventral Tegmental Area.

Difference betweeen functional and ideopathic isolated dystonia

Feature	Functional dystonia	Ideopathic isolated dystonia
Onset	• Sudden onset	• Not sudden, evolves over years or months
Fixed dystonia	• Present	• Absent
Symptoms progression	• Rapid, fluctuating	• Gradual, no fluctuation
Precipitanting event	• Injury, traumatic experience, physical event	• Low connection to injury or stress
Resolution	• Spontaneous remissions may occur	• Rare spontaneous remission
Clinical Exams	• Incongrous, highly inconsistent and variable movements	• Congrous and highly internally consistent

Figure 2.6: Differences between functional dystonia and isolated idiopathic dystonia, adapted from [42].

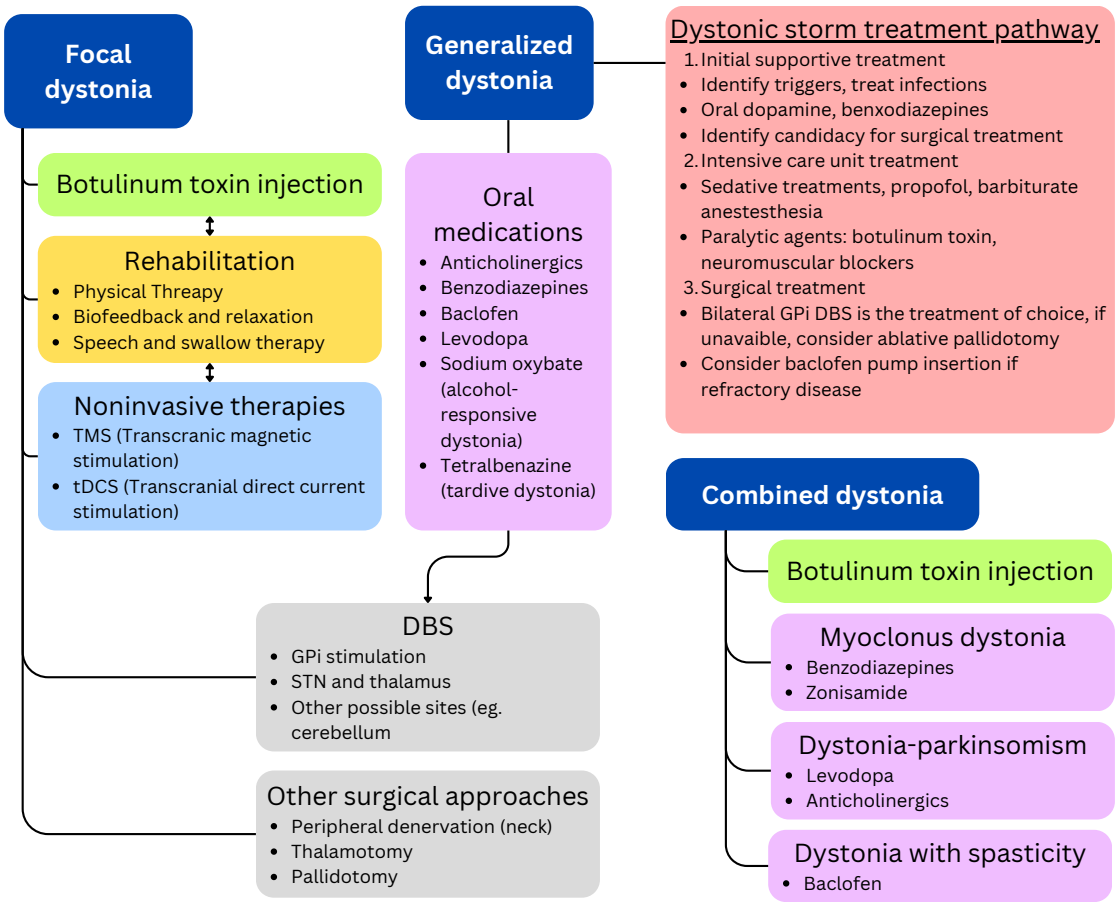

Figure 2.7: Summary chart of dystonia treatment options, adapted from [33]. DBS = deep brain stimulation; GPi = globus pallidus internus; OT = occupational therapy; PED = paroxysmal exercise-induced dyskinesia/dystonia; PKD = paroxysmal kinesigenic dyskinesia/dystonia; PNKD = non-kinesigenic paroxysmal dyskinesia/dystonia; PT = physical therapy; rTMS = repetitive transcranial magnetic stimulation; SLP = speech and language pathology; SPR = sepiapterin reductase; STN = subthalamic nucleus; tDCS = transcranial direct current stimulation; TMS = transcranial magnetic stimulation.

Chapter 3

Deep Brain Stimulation

DBS is a neurosurgical procedure that permits reversible and targeted neuromodulation of specific circuits. In 1948, neurosurgeon Lawrence Pool of Columbia University conducted the first electrode implantation, obtaining a positive outcome [45]. With FDA approval and CE certification, it is now a standard treatment for essential tremor, Parkinson's disease, and dystonia [46, 47, 48]. Additionally, it has been used to treat epilepsy and pain syndromes like neuropathic pain and cluster headaches [49, 50, 51]. It is also being studied for a variety of treatment-resistant mental illnesses, including major depressive disorder, Alzheimer's disease, and Tourette syndrome, all of which are characterized by disruptions in brain circuits [52].

The Ventral InterMediate nucleus (VIM) of the thalamus, the STN, and the GPi are among the targets that have been investigated for DBS treatment of dystonia. These sites, corresponds to where the electrodes are implanted and are key areas for muscle contractility. Nonetheless, the sensorimotory region of GPi is the main target [53]. By acting at the axonal terminals, the external source of activation determined by the DBS device triggers the release of neurotransmitters, which in turn encourages non-functional areas to resume their normal functions. The works of Frey et al. (2022) [54], Sironi (2011) [55], and Krauss et al. (2020) [56] are the sources of the information in this chapter.

3.1 History of DBS

Spiegel and Wycis introduced a stereotactic apparatus (Figure 3.1) in 1947, which was initially used for ablative procedures [57]. This marked the beginning of the development of modern DBS technology.

The first person to investigate the therapeutic potential of subcortically implanted electrodes was Columbia University neurosurgeon Lawrence Pool. After

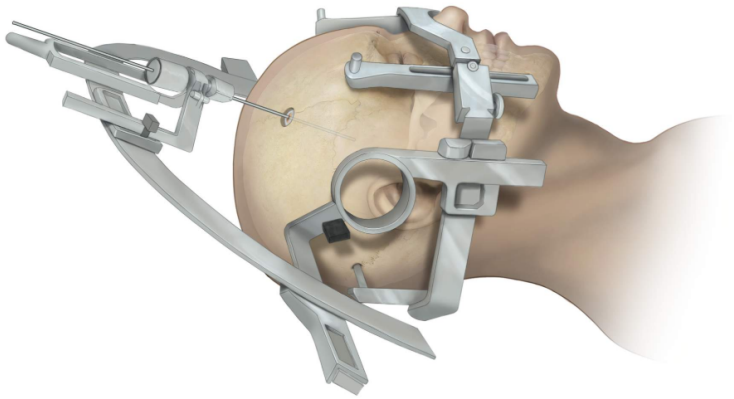

Figure 3.1: Framed stereotactic setup [58].

implanting an electrode into the caudate nucleus of a lady suffering from anorexia and depression in 1948, Pool reported positive outcomes for a few weeks until the wire broke [45]. DBS was investigated as a therapy for chronic pain and neurological problems throughout the 1970s. With the first commercially accessible stimulators used for spinal cord stimulation to alleviate pain, the area owes a lot to the technology of cardiac pacemakers. Mazars and Hosobushi made important contributions to the development of neurostimulation for the treatment of movement disorders, which eventually led to DBS targeting the sensory thalamus [59, 60].

In 1975, Medtronic Inc. became the first company to trademark the term "DBS" for DBS [61]. The 1980s marked the first reports of DBS for the treatment of neurological symptoms like tremor, dystonia, and speech impairment. In the late 1980s, Benabid and his colleagues reported successful chronic electrode implantation in the VIM of the thalamus to treat tremor in both Essential Tremor (ET) and PD patients [62]. DBS became the favored method, particularly for bilateral surgeries, since research showed that it had less persistent side effects than lesional treatments.

The first Implantable Pulse Generator (IPG) for DBS, launched by Medtronic, had a maximum frequency of 130 Hz, which remains the standard for most DBS applications today. The device initially supported only unilateral stimulation. In 1999, Medtronic introduced a dual-channel IPG with a frequency of up to 250 Hz, a device that became widely used, particularly for STN stimulation in PD patients. By 1993 and 1997, DBS targeted at the VIM nucleus for ET and severe PD tremor received CE Mark and FDA approval, respectively. Since then, DBS's list of approved uses has grown to include a variety of neuropsychiatric and movement diseases, such as epilepsy, PD, dystonia, and obsessive-compulsive disorder. With

a humanitarian device exemption for obsessive compulsive disorder (anterior limb of the internal capsule), the device has been authorized for use in PD (VIM, STN, GPi), epilepsy (anterior nucleus of the thalamus), and dystonia (STN, GPi) [63].

With encouraging but limited findings, DBS is currently being studied for its ability to treat various illnesses such Tourette syndrome, serious depression, and Alzheimer's disease. Additionally, DBS has been experimentally used to treat problems including chronic pain, obesity, addiction, and anorexia [64].

The main stepstones in the history of DBS are illustrated in Figure 3.2.

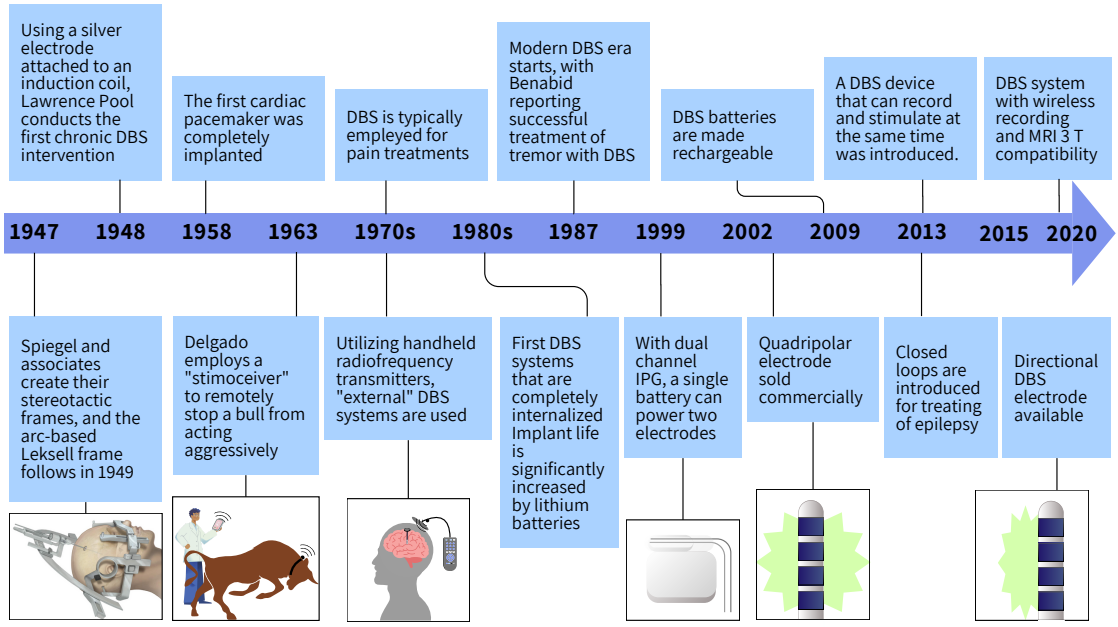

Figure 3.2: Timeline of technology development for DBS, adapted from [56].

3.2 Components of DBS System

The DBS system is composed by an **IPG** or neurostimulator that acts as the waveform generator and power source, **DBS leads** (electrodes) that are implanted in the brain tissue, and the **extensions** that connect the IPG to the leads Okun2008, as shown in Figure 3.3.

3.2.1 Implantable Pulse Generator

The IPG is the core active component in contemporary DBS systems. It contains a battery, power module, CPU with program memory, and a microprocessor that

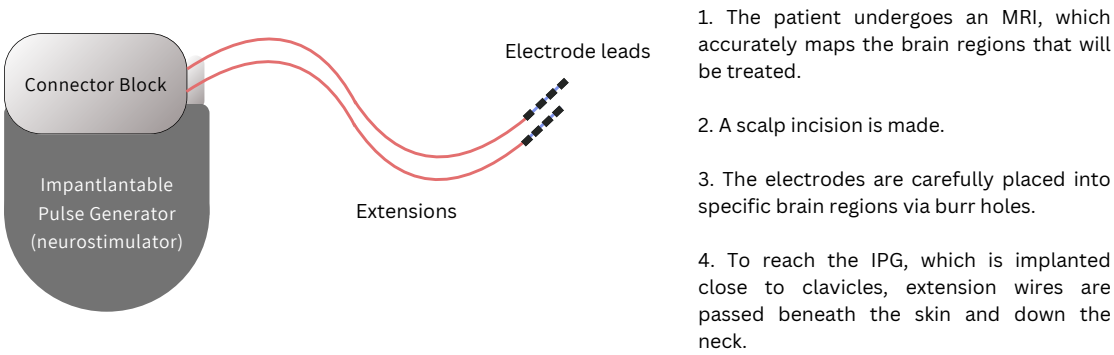

Figure 3.3: The deep brain stimulation system is composed of the Implantable Pulse Generator (IPG), the extensions that connect the IPG to the leads, and the electrode leads that are implanted into the brain, adapted from [65].

manages the device's functions. Functionalities including activation, deactivation, pulse settings, internal diagnostics, and communication with external devices. Certain IPGs also feature additional capabilities, such as recharging functions, built-in accelerometers, Local Field Potential (LFP) sensing, as well as onboard signal processing and analytical functions. The technical characteristics of commercially available IPGs are shown in Figure 3.4 [66] The IPG is commonly placed inferior to the clavicle superficial to the pectoralis fascia.

Model	St. Jude (Abbott) Infinity 5	St. Jude (Abbott) Infinity 7	Boston Scientific Vercise PC	Boston Scientific Vercise Gevia	Boston Scientific Vercise Genus P8/P16
No. of channels	2	2	2	2	1/2
Weight (gram)	49	58	55	26	58
Size (mm)	56×50×13	67×50×14	71×50×11	51×46×11	72×50×12
RC	No	No	No	Yes	No
Freq. range (Hz)	2–240	2–240	2–255	2–255	2–255
Pulse width (μs)	20–500	20–500	10–450	20–450	20–450
TF	MSS	MSS	A	A	A
CF	CA	CA	MICC	MICC	MICC
Directional lead	Yes	Yes	Yes	Yes	Yes
MRI safety	C	C	U	C	C
LFP sensing	No	No	No	No	No

Model	Boston Scientific Vercise Genus R16	Medtronic Activa PC	Medtronic Activa RC	Medtronic Activa SC	Medtronic Percept PC
No. of channels	2	2	2	1	2
Weight (gram)	27	67	40	44	61
Size (mm)	52×46×11	65×49×15	54×54×9	55×60×11	68×51×12
RC	Yes	No	Yes	No	No
Freq. range (Hz)	2–255	2–250	2–250	3–250	2–250
Pulse width (μs)	20–450	60–450	60–450	60–450	20–450
TF	A	IL	IL	IL	IL
CF	MICC	No	No	No	No*
Directional lead	Yes	No	No	No	No
MRI safety	C	C	C	C	C
LFP sensing	No	No	No	No	Yes

Figure 3.4: Features of currently available internal pulse generators on the market. Abbreviations: A, areas; C, conditional; CA, coactivation; CF, current fractionation; Freq., frequency; Hz, Hertz; IL, interleaving; LFP, local field potential; MICC, multiple independent current control; MRI, magnetic resonance imaging; MSS, multi-stimulation set; PC, primary cell; RC, rechargeable cell; SC, single cell; TF, temporal fractionation; U, unsafe. Availability of features or devices may vary by region, and some are subject to local regulatory approvals. Image sourced from [66], lincensed for use under CC BY 4.0.

3.2.2 Electrode Leads

DBS involves using a small electrode or lead to deliver electrical impulses to targeted regions of the brain. Key attributes of an electrode are biocompatibility, inertness, durability, long-term stability, ease of implantation, good conductivity, suitable electrical characteristics, effective current delivery and spatial arrangement. MRI compatibility and the possibility of sensing capabilities are further crucial considerations.

Platinum-iridium wires and nickel alloy connections, all enclosed in a polyurethane sheath, are commonly found in DBS electrodes. Platinum-iridium is favored because of its excellent conduction qualities and low toxicity. Currently, several electrode configurations are available (Figure 3.5). The most common design is quadripolar, with four stimulating contacts located at the tip of a 1.27 mm diameter probe. Each cylindrical contact is 1.5 mm long, with spacing of either 0.5 mm or 1.5 mm between them. During stimulation, an electrode contact can function as a cathode (or current sink) or as an anode (source of current) relative to the implantable pulse generator or to other electrode contacts. The electrode configurations in Figure 3.5 allow for shaping the electric field along the z-axis of the lead by adjusting combinations of anodes and cathodes during programming [56].

Commercially available leads vary and are selected based on the brain area being targeted and the therapeutic indication (Figure 3.6, Figure 3.7).

A 2015 consensus paper [67] highlighted the lack of studies comparing clinical outcomes of regulated current versus regulated voltage DBS, suggesting that current-controlled DBS would provide more stable effects due to dynamic changes in electrode impedance over time caused by inflammation.

The shape of the stimulation waveform, which refers to the current or voltage over time, can influence the number and type of neural elements activated Grill2015. Waveforms or pulses can be repeated at different intervals to create specific stimulation patterns (Figure 3.8). Research indicates that symmetric biphasic pulses are more effective at suppressing PD motor symptoms compared to conventional asymmetric waveforms, although they may cause more battery drain. In patients with ET, symmetric biphasic pulses also showed better tremor suppression than asymmetric DBS waveforms. At the same intensity, symmetric biphasic pulses likely activate a greater number of neurons since both the cathodic and anodic phases of the waveform contribute to neural activation. Additional factors that may enhance neuron activation and entrainment include selecting the right waveform polarity, reversing the usual pulse phase order, and introducing a gap between the two phases of charge-balanced biphasic pulses. The shape of the waveform can

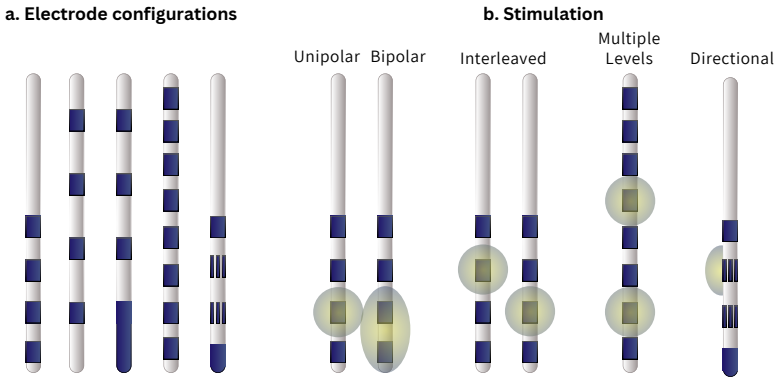

Figure 3.5: Common electrode configurations and modes of stimulation for Deep Brain Stimulation (DBS). a) Various electrode designs for DBS, with dark grey regions representing electrode contacts that can be activated to deliver current. The configurations vary in the spacing between contacts and their number and shape. Larger spacing between contacts increases the range of neural targets, while smaller spacing offers more precise control over stimulation. b) Different stimulation modes used in DBS systems. Unipolar stimulation: current is directed from the battery to the electrode contact or vice versa. Bipolar stimulation: Current flows between at least two electrode contacts, one functioning as the anode and the other as the cathode. Interleaving stimulation: Alternates between different stimulation settings. Multiple level stimulation: Stimulation of multiple neural targets along the electrode path. Directional stimulation: Current is directed or "shaped" based on the local anatomy or clinical symptoms for more targeted stimulation. Adapted from [56].

also affect the desynchronizing effects of DBS techniques, where pulse amplitude is adjusted in a **closed-loop** system using linear or nonlinear delayed feedback [56].

3.2.3 Extensions

The stretch-coil extensions, which connect the IGP to the electrodes, are coated with silicone [68], which is frequently used in medical equipment due to its excellent electrical insulating properties and biocompatibility. Silicone also permits the secure transfer of electrical signals from the electrodes to the pulse generator and shields the cables from electrical interference. These extensions are placed under the skin, extending from scalp to chest, behind the ears, and along the neck. Due to the flexibility and strength of the silicone coating, the extensions resist normal daily pressures and movements without the loss of integrity of the system. The stability of the leads may be assessed using a variety of techniques and observations. Finding any unstable impedance is crucial: physical faults may cause changes in

Manufacturer	Lead Type	Number of Contacts	Lead Diameter (mm)	Length of Contacts (mm)	Spacing Between Contacts (mm)
Medtronic	3387	4	1.27	1.5	1.5
	3389	4	1.27	1.5	0.5
	3391	4	1.27	3.0	4.0
	Sensight BM33005	8 (1-3-3-1)	1.36	1.5	0.5
	Sensight BM33015	8 (1-3-3-1)	1.36	1.5	1.5
Abbott	6166 and 6168	4	1.29	1.5	0.5
	6167 and 6169	4	1.29	1.5	1.5
	6170 and 6172	8 (1-3-3-1)	1.29	1.5	0.5
	6171 and 6173	8 (1-3-3-1)	1.29	1.5	1.5
Boston Scientific	Linear 8-contact lead (DB-2201-30DC/DB-2201045DC)	8	1.3	1.5	0.5
	Cartesia directional lead (DB-2202-30/DB-2202-45)	8 (1-3-3-1)	1.3	1.5	0.5
PINS medical	L301 and L301S	4	1.3	1.5	0.5
	L302 and L302S	4	1.3	1.5	1.5
SceneRay	1200	4	1.27	1.5	0.5
	1210	4	1.27	1.5	1.5

Figure 3.6: Description of present available commerical leads and their parameters including number and sizes of contacts. Image sourced from [54], with license CC BY 4.0.

the system's impedance when it is in vivo, disruptupting the normal operation of pacemaker treatment or DBS [69], [65].

3.3 Chirurgical Procedure

DBS leads are implanted using stereotactic techniques and monitored with MER to attain the highest level of precision. Using information about depth obtained using preoperative MRI imaging, MER signals aid in fine-tuning the initial targeting and correcting for errors brought on by patient anatomical variances or brain movement. Four spindles are placed percutaneously along the outside edge of the skull to secure the stereotactic frame while the patient is conscious. To identify the exact target inside the brain, preoperative MRI is aligned with the stereotactic frame.

Once the DBS lead is positioned in the target brain region, the neurostimulator is implanted under general anesthesia, typically in the subclavicular area, though it may be placed in the abdomen for pediatric patients. To ensure accurate placement, radiological imaging is usually performed at the end of the procedure, an example of which is shown in Figure 3.9.

3.4 Adversarial Effects and Complications

Rigidity, dysphonia, dysarthria, postural instability, and impairment of coordination are the possible adverse effects if the surrounding GPi structures are inadvertently

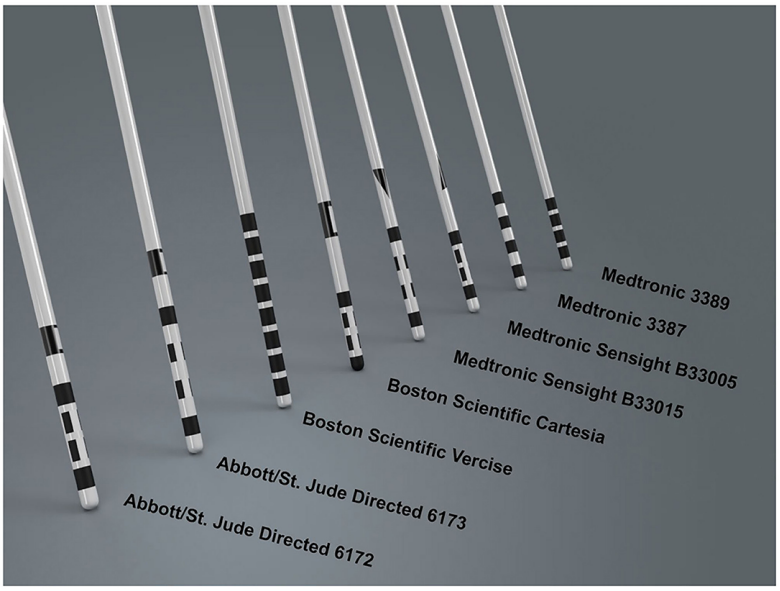

Figure 3.7: The lead designs available from various Deep Brain Stimulation (DBS) manufacturers feature different configurations. Some leads have full-ring contacts, which enable omnidirectional stimulation, while others are equipped with segmented electrodes on the middle two levels, allowing for directional stimulation. Many manufacturers incorporate stereotactic markers above the DBS contacts to assist with post-operative orientation of the lead in relation to its intended direction. Image sourced from [54], with license CC BY 4.0.

affected. Hardware-related complications include infection of the skin or implant, malfunction or erosion of the IPG, and electrode or extension wire fractures. Another concern is also battery life, particularly in young patients who, throughout their lives, are doomed to have several surgeries to replace those batteries, which carries a great risk of surgical complications. This problem was partially resolved in recent times with the use of rechargeable devices [71].

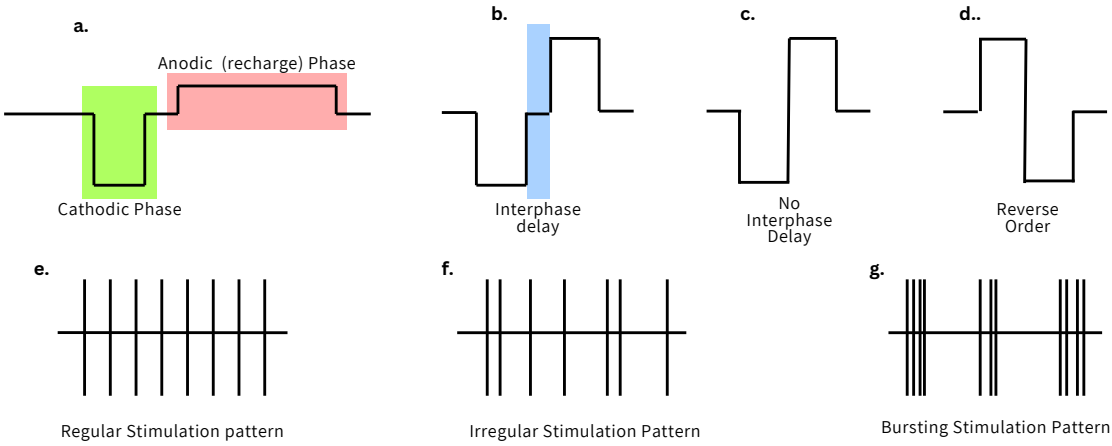

Figure 3.8: In Deep Brain Stimulation (DBS), stimulation patterns are generated by repeating waveform shapes at specific intervals between pulses. a) A conventional asymmetric biphasic DBS waveform consisting of a brief cathodic phase, followed by an interphase delay, and a prolonged anodic (recharge) phase. b) A symmetric biphasic DBS waveform with cathodic and anodic phases of equal duration. c) A symmetric biphasic DBS waveform with no interphase delay. d) A variation in which the standard pulse phase order of the symmetric biphasic waveform is reversed. e) A regular stimulation pattern where the interpulse intervals are consistent, typically around 7.7 ms or 130 Hz. f) An irregular stimulation pattern where the interpulse intervals are randomized. g) A burst stimulation pattern featuring multiple pulses at short intervals, followed by a longer interpulse interval. Figure adapted from [56].

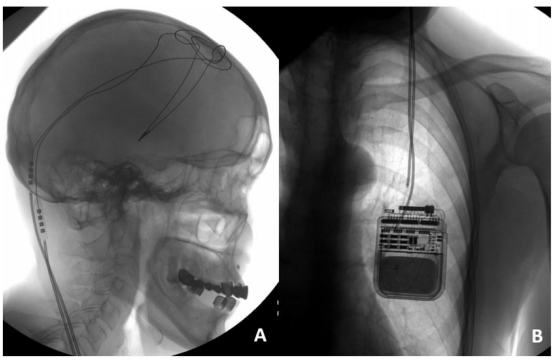

Figure 3.9: Postoperative X-rays of the neck and chest showing a DBS system with implanted electrodes and extension wires (left image) and the IPG positioned at the thoracic level (right image). Image sourced from [70], under licence CC (Creative Commons) BY 4.0.

Chapter 4

Microelectrode Recordings

Many studies have shown that the use of MER is essential in DBS surgery [72], [73], as was mentioned in the previous chapters. The surgical target, which may be different from the preoperative target established by imaging methods like MRI, can be assessed with higher accuracy using MER during surgery [74]. This chapter provides an overview of how the MER signal is generated, acquired, and processed to extract relevant information about the surgical target. Spike sorting techniques are specifically examined in order to examine the properties of individual neurons as well as the overall signal, including oscillatory and temporal features.

The anatomical origin of the signal and the acquisition system are based on the insights from the book by E. B. Montgomery Jr. "Intraoperative Neurophysiological Monitoring for Deep Brain Stimulation: Principles, Practice and Cases" [75]. An example of MER signals is shown in Figure 4.1.

4.1 Generation of MER Signals in the Brain

The electrical signals captured during surgery in the context of intraoperative neurophysiological monitoring are derived from the ion movement-induced voltage changes across the neuron's membrane. When there is a separation of charges, electrical current is generated, and this flow of ions through the cell membrane produces the electrical signals that are recorded by the acquisition system.

4.1.1 Neuron Structure

A neuron is composed by the cell body, or soma, which houses the nucleus and other vital components, and axons, which are in charge of transmitting information over long distances. A schematic representation of a neuron, picturing its basic structures, is illustrated in Figure 4.2.

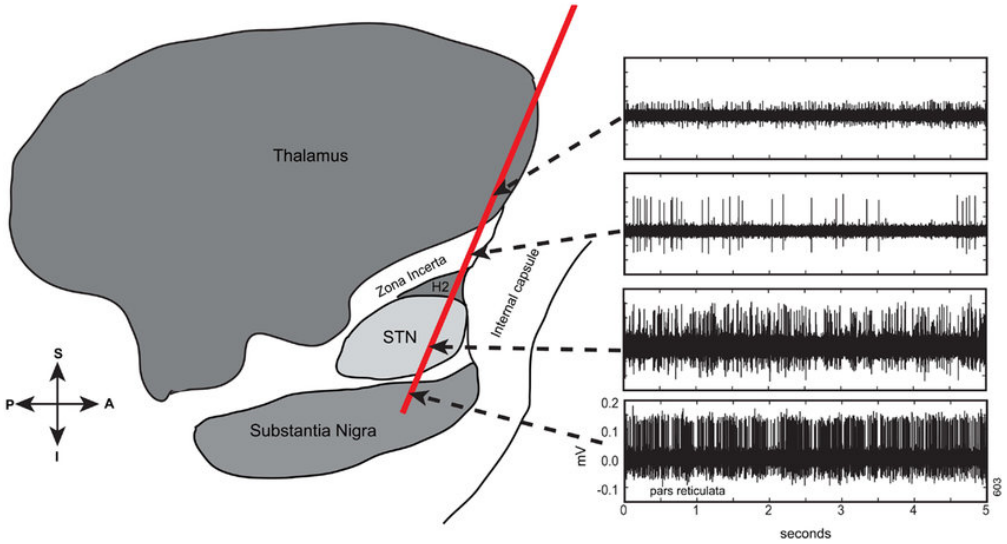

Figure 4.1: An illustration of microelectrode recordings along a trajectory and characteristic electrophysiological activity when passing through the thalamus, zona incerta, SubThalamic Nucleus (STN) and Substantia Nigra pars reticulata (SNr). Figure sourced from [76], under license CC BY 3.0.

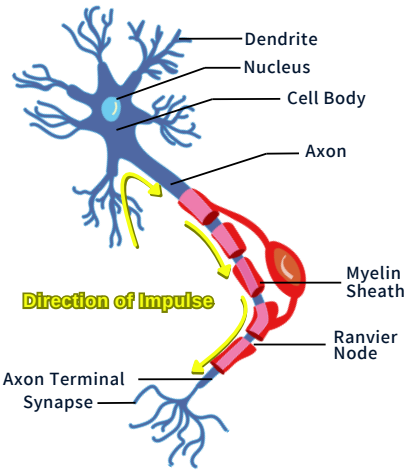

Figure 4.2: Schematic representation of a neuron. A neuron consists of a cell body containing a nucleus, and two type of branches: axons (long branches which permit conduction of information between neurons) and dendrites (short branches which receive information from other neurons).

Axons can extend from the cerebral cortex up to the spinal cord, and their terminals connect with other neurons to form connections called synapses. There are two types of synapses. Chemical synapses use neurotransmitters and are in charge of chemical transmission between neurons, while structures called gap junctions enable direct electrical transmission. The cell membrane that surrounds a neuron acts as a barrier to protect it and controls the flow of chemicals into and out of the cell. The properties of the internal environment of the neuron is maintained by the cell membrane, which also produces an electrochemical gradient, essential for neural activity. The lipid bilayer that composes a large part of this membrane is selectively permeable, letting some ions and molecules flow through while obstructing others.

4.1.2 Action Potential

Electricals signal generated by neurons and used for intraoperative neurophysiological monitoring is the result of the separation of ions, particularly sodium (Na+) and potassium (K+). An electrochemical gradient is produced by the different Na+ and K+ ion concentrations inside and outside the neuron. The charge difference across the membrane is a result of mechanisms in neurons' membranes that actively transport these ions, ensuring that more K+ is inside and more Na+ is outside.

In order for the electric current to flow, the neuron's membrane has to allow ions to pass through protein channels that act as pores in the membrane. These channels remain closed in the resting state to prevent the flow of current, which results in no signal. The generation of an electrical signal depends on the opening and closing of these channels, which can be regulated with different mechanisms. One method involves the release of neurotransmitters, which attach to the channel's receptors and cause it to open, another technique uses G protein-coupled receptors to open channels by initiating enzymatic cascades. Additionally, when a threshold is reached, voltage-gated channels open, permitting an influx of ions and initiating the Action Potential (AP). As shown schematically in Figure 4.3, the movement of Na+ and K+ ions across the membrane is the main factor of the AP generation process.

The resulting change in membrane voltage is propagated along the axon and its myelin sheath, allowing the neuron to transmit the AP over long distances without any loss of signal through saltatory conduction. The signal propagates in only one direction because of the refractary period, in which Na+ channels are deactivated, preventing any subsequent polarization and generation of AP.

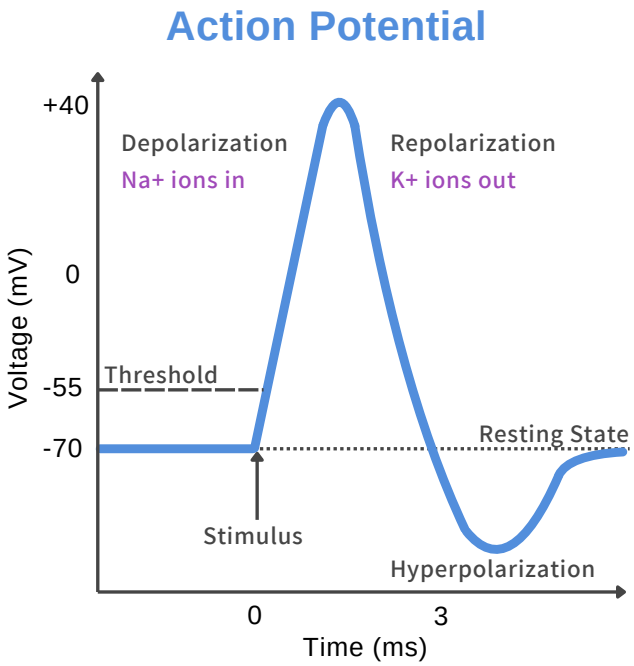

Figure 4.3: The action potential generation process begins when a neuron is at its resting membrane potential, with ion channels closed to prevent sodium (Na+) from entering and potassium (K+) from exiting. When a stimulus increases the membrane voltage to a threshold, Na+ channels open, allowing an influx of Na+, leading to depolarization. This triggers a chain reaction, further opening Na+ channels. As the potential rises, K+ channels open, allowing K+ to exit, repolarizing the membrane. Hyperpolarization follows before the neuron returns to its resting state [75].

4.2 Acquisition System, Noise and Artifacts

Recording an AP requires the measurement of a difference in the voltage or potential across two points. MER systems feature an active contact and a reference. Since each contact must experience a distinct electrical field potential or voltage in order to register a signal, no detectable voltage difference is produced if two contacts of the same material are placed within the same electrical field (Figure 4.4 A). The two contacts are located relatively close to the neural element (B) in bipolar recordings. In monopolar recording, a fine contact is placed near the neural element that is the source of the signal, while a large contact is located some distance away from the source (C).

Axons produce exceptionally small voltages that are impractical to record using anything other than high amplification and small electrode tips. However, using

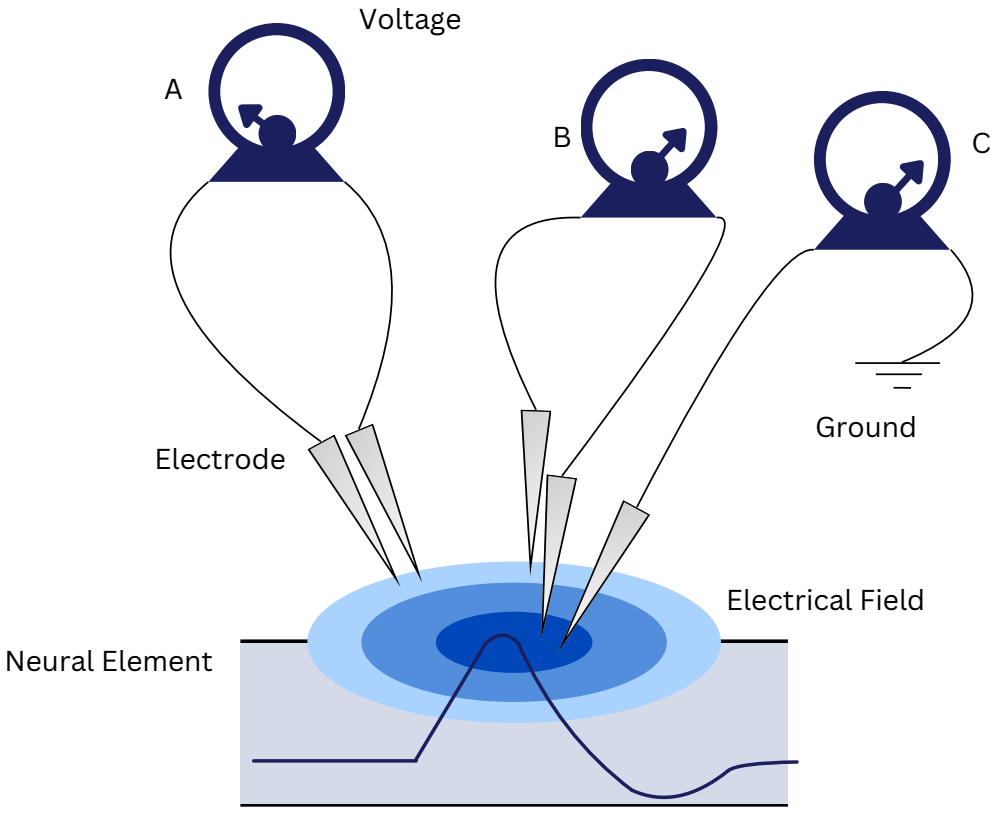

Figure 4.4: Schematic representation of different types of acquisition. A and B represent bipolar recordings, while C is a monopolar recording [75].

such electrodes leads to high impedance. This renders normal MER extremely challenging, especially when combined with the high gain needed. One must then decide which neural elements to record. The dendrites and cell body are the usual chosen elements because the axons' APs are too brief and low voltage to record under typical circumstances.

Orthodromic conduction is the path taken by an AP that is generated and travels down the axon to the synaptic terminals. The AP simultaneously backfires into the dendrites and cell body. Antidromic conduction is the term for its movement in this opposite direction. The volume occupied by the dendritic tree and cell body, as well as the relative synchronization of voltage changes due to the antidromic invasion of the dendrites and cell body by the AP 4.5, are two factors that significantly amplify the antidromically conducted APs and thus enable recording.

Microelectrodes are typically made with tungsten or a platinum-iridium alloy metal, with fine-tip of conic shape on the order of 20 μm diameter and impedance

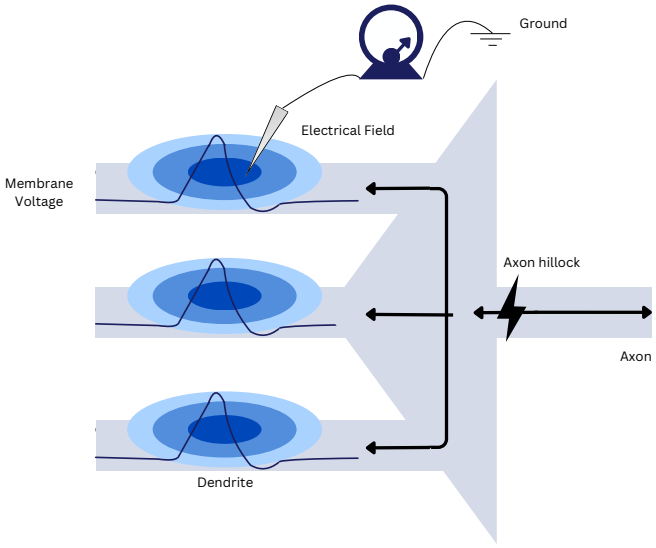

Figure 4.5: An antidromic action potential is shown schematically. When the neuronal membrane potential at the axon hillock depolarizes to a threshold, an action potential starts. The action potential is conducted orthodromically along the axon. The force of the action potential, however, conducts antidromically through the cell body and dendrites in the form of a graded potential, producing the signal that microelectrodes record. The resulting electric field is amplified to a range that allows recording by conventional methods due to the larger volume of the dendritic tree. [75].

around 0.6 to 1 $M\omega$. A raffiguration of a bipolar microelectrode is shown in Figure 4.6.

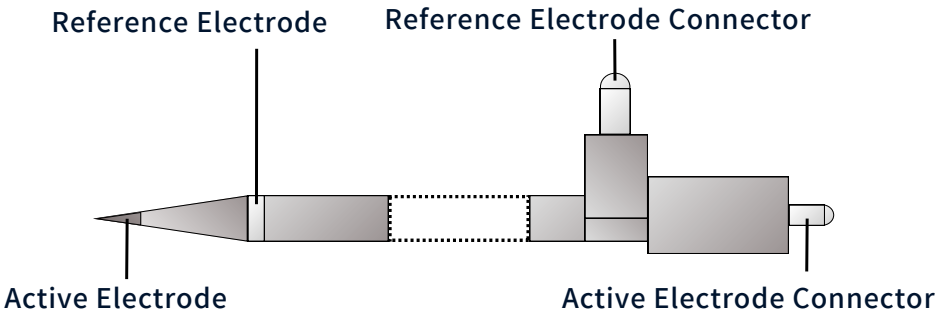

Figure 4.6: Schematic view of a bipolar microelectrode. the active electrode is the tip, and the indifferent or reference electrode is the band of conductive material at few mm from the tips [75].

Microstimluation through microelectrode tip can be used during the surgery to simulate clinical effects of the final DBS lead impantation, by using similar stimulation parameter to those employed in clinical DBS. Platinum-iridium microelectrode are better suited to perform intraoperative stimulation than the tungsten one, as they tend to better withstand stimulations. Stimulation currents are typically less than 100 µA. Microstimulation can also elicit a physiological response from structures near the microelectrode, which may give informations about electrode localizations.

MER allow the identification of extracellular APs from individual neurons, which are in the range 50 μV to 100 μV. The extremely low voltages of AP may require an ampilifaction of 10000 or so. The high gain amplifies not only the signal of interest but also a great deal of noise and artifacts, making filtering essential.

Noise arrives for the most part from electrical sources. Noise from the amplifier system can be of a thermal origin, arising from random movement of electrical charges. "Shot noise" is caused by the discetization of charge as an electron, causing high frequency transient; while "flicker noise", which is frequency dependant, has greater impact at lower frequency (DC). AC power line interference at 50 or 60 Hz can be present, as also noise generated by capacitive coupling with devices producing electrostatic charges. If an artifact is common to to electrodes, it can be canceled using differential amplifiers.

While noise is usually persistent in the MER signal, mechanical sources can generate artifacts, for example a mechanical vibration transitted to the connectors, particularly those connecting the preamplifier. Artifacts are heuristically defined as transient, are mechanical in nature and can occur as a result of unstable electrical connections. To drive the electrodes in the skull mechanical gears are used to move the microelectrodes along a guide canula. A type of artifact called microdrive chatter occurs when the microelectrode slides unevenly along its guide canula. Damage or wear of the gears can also create artifacts. Microelectrode can cause a tear in the neuronal membrane, permitting Na+ ions to enter the neuron. This brings a massive depolarization and concomitant repetitive APs, as waters enters wth Na+ and causes the neuron to burst.

MER systems are composed of a microelectrode (4.7 B) capting signal from a neural source (A), an high impendence amplifier or unity-gain amplifier used for impedence matching (C), an amplifier (D), a filtering system (E), an analog to digital converter (F) and finally the computer system (G) used for analysis with possible visual display (H) and audio presentation (I). This system is schematized in Figure 4.7.

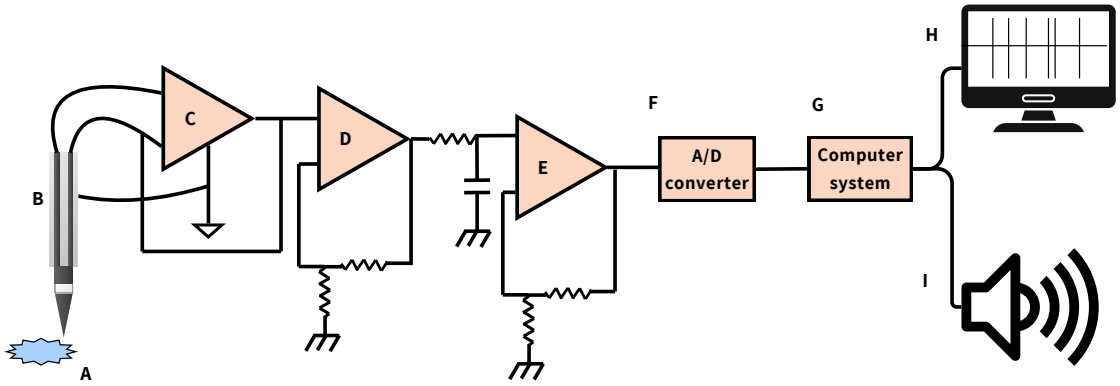

Figure 4.7: Scheme of a typical microelectrode recording system, where A is the neural source, B is the microelectrode capting the signal. Following, there is an high impendence amplifier or unity-gain amplifier used for impedence matching (C), an amplifier (D), a filtering system (E), an analog to digital converter (F) and finally the computer system (G) used for analysis with possible visual display (H) and audio presentation (I) [75].

4.3 Intraoperatory Use of MER

Centers that perform MER-guided DBS typically use a BenGun multielectrode holder which allows up to 5 microelectrodes to be lowered to the target simultaneously [77], following different trajectories. A schematic representation of the five possible trajectories of the BenGun setup (anterior, posterior, central, lateral, medial) is shown in Figure 4.8, while an example of a commercialy available microdrive system is shown in Figure 4.9. The electrode is lowered into the skull at small steps of 1 mm or even 0.5 mm.

4.4 Processing of the MER Signal

Summarizing, MER are used to record and analyze action potentials using microelecrodes with extra-fine tips, corresponing to high impedances. Action potentials in MER signal are also commonly refferred to as "spikes". The MER signal can be studied focusing on two aspects, the Single-Unit Activity (SUA) and the Multi-Unit Activity (MUA).

MUA refers to the action potentials of neurons recorded in a radius of 140-300 μm from the electrode tip [79], without undergoind spikes separations to assign each spike to its corresponding neuron. MUA can be characterized using informations from the time and spectral domain. SUA refers to the ensamble of action potentials of a single neuron [79, 80], which can be distinguished from spikes of other neurons

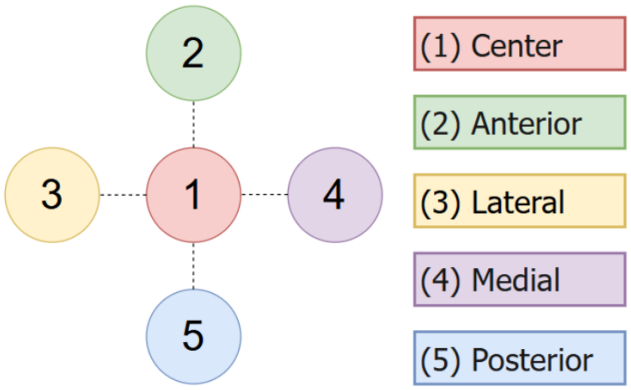

Figure 4.8: Graphic representation of electrode configuration in a standard Ben's Gun system. the elctrode are typically distant 2 mm from each other.

Figure 4.9: Photo of a microdrive system commercially available at "inomed", with a zoom on the five electrode tips [78].

using a variety of techniques known as Spike Sorting. The frequency content of neural spikes has a frequency content around 300-500 Hz to 3000-6000 Hz [81, 82, 83].

Another kind of signal that can be recorded during DBS surgery is the LFP. LFP are not made to identify extracellular AP, so their electronical characteristics are much less demanding. Electrodes can be larger and thus have lower impedances. Using LFP, one records the summing of neural activity over a wider volume of tissue (0.5 - 3 mm), containing lower frequency content with respect to MER. LFP emphasizes presinaptic dendritic inputs over extracellullar AP [75]. Since they are easier to record, they are well suited for use in closed-loop DBS, where therapeutic stimulation over the DBS leads is regulated based on the recorded LFP by the lead itself [84]. LFP can also be obtained by recording with a typical microelectrode by

keeping it more distant to neurons or by recording the comprehensive broadband electrical signal and then isolating the 0-300 Hz component.

An infographic distinguishing MUA, SUA and LFP is shown in Figure ref-fig:muasua.

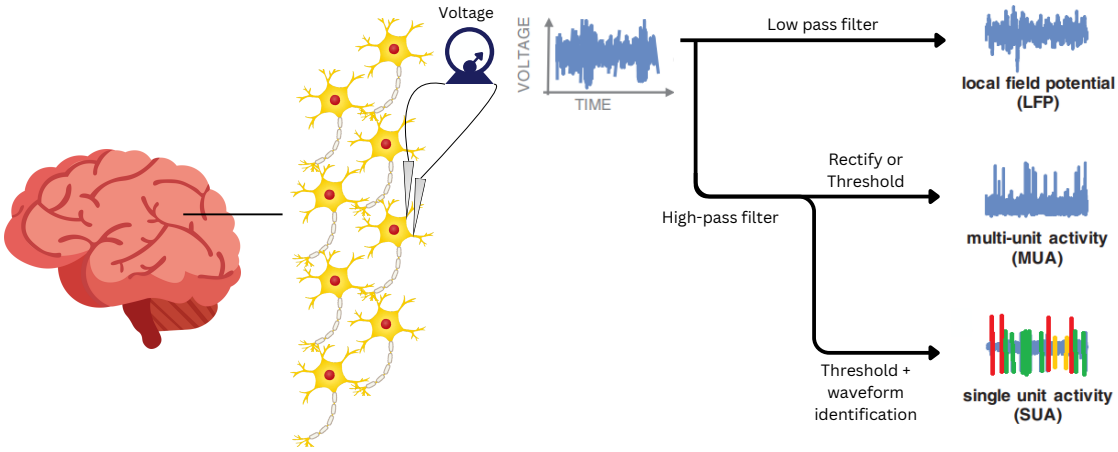

Figure 4.10: Different types of extracellular neurophysiological signals. They are typically discriminated in three classes. (1) Limiting the broad band raw data into low frequencies results in a signal called Local Field Potentials (LFP), which is a summed average of action potentials. (2) Multi Unit Activity (MUA) is the activity of a large population of neurons in the high frequency spiking activity range. MUA is often thresholded or rectified in order to obtain the time-varying envelope. (3) Single Unit Activity (SUA) is composed of the ensamble of isolated action potentials of a single neuron, obtained through a spike sorting process (highlighted by different colors of red, green and yellow for each identified neuron). Figure adapted from [85].

4.4.1 Spike Sorting

Spike sorting refers to a series of techniques used to extract information about the activity of single neurons from extracellular recordings. Close neurons can fire in response to different stimuli, therefore, it's crucial to understand which spike corresponds to which neurons. Spike sorting techniques are used to analyze signals acquired both in-vivo and in-vitro applications, especially from MicroElectrode Arrays (MEA) which contain multiple microelectrodes. Informations about the spike sorting process reported in this sections are elaborated from the review of Rey et al. (2015) [86], "Past, present and future of spike sorting techniques".

The classic spike sorting process is shown in Figure 4.11. Each step is explored more in depth in the following.

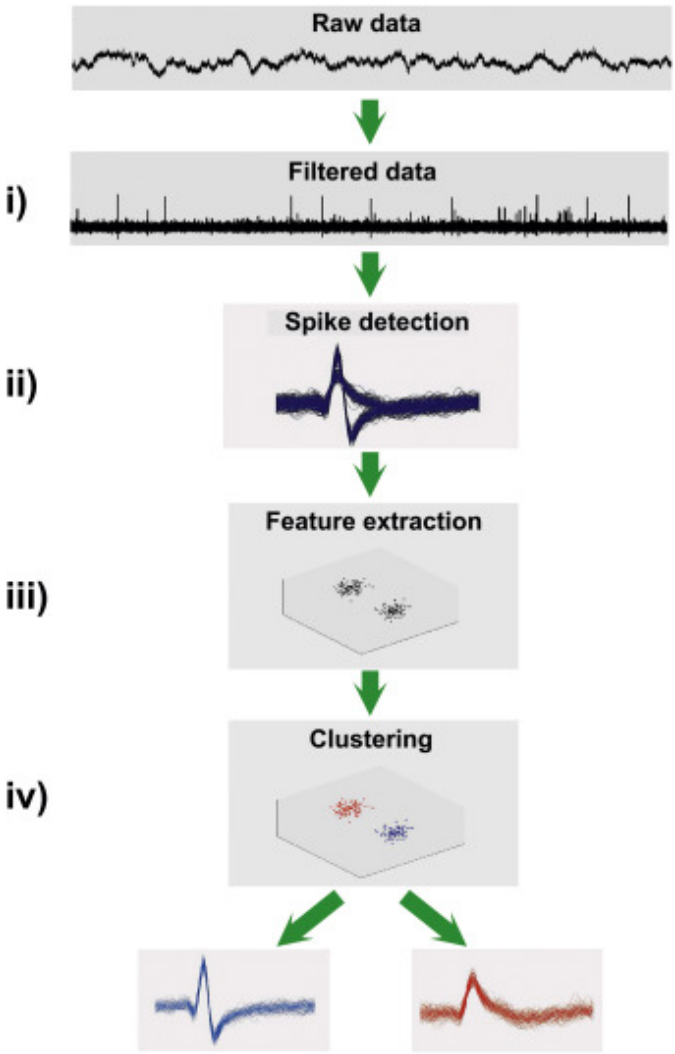

Figure 4.11: Flowchart containing the main steps of spike sorting. Starting from recorded bradband data, (i) a bandpass filter is applied, usually between 300-3000 Hz. (ii) Spikes are detected using an aplitude threshold to data previously filtered. (iii) Relevant feature are extracted from each spike to achieve dimensionality reduction. (iv) these features are used to perform a clustering algorithm and classify each waveform to each cluster, which corresponds to a different neuron. Figure sourced from [86] under 4.0 CC license.

Filtering

To detect spikes the signal is typically bandpass filtered, usually in the bandwidth 300 to 3000 Hz, to exclude the contribute of LFPs. Regarding filtering, it's essential

to consider phase non-linearity, as it can distort spike shape and alter artifacts to make them look similar to spikes. Using offline processing, the best solution is to use zero-phase filtering, to obtain zero pahse response for all the frequencies. In the case online processing is desired a nearly linear phase Infinite Response Filters (IIR) can be used.

Detection
Subsequent to filtering, detection is performed using, for example, an amplitude threshold. to select an automatic threshold, it's reasonable to estimate the threshold based on the noise level. In principle, it should be sufficient to use a value based on the standard deviation of the filtered signal. However, such a theshold can result in high error rates, especially in cases with large amplitude spikes and high firing rates that can lead to an increase of the threhshold even when the noise is constant. A better estimate was proposed by Quiroga et al. (2004) [87]. For a normally distributed noise N, it can be shown that

$$\sigma_n = \frac{\text{median}(|N|)}{0.6745} \tag{4.1}$$

in which the denominator comes from the cumulative distribution function for the standard normal distribution evaluated at 0.75. The fact the signal X is typically sparse in spikes leads to the presence of spikes not affecting the mean absoute deviation as much, so median(|X|) $\approx$ median(|N|). The estimate for the threshold becomes

$$\sigma_n = \frac{\text{median}(|X|)}{0.6745}. \tag{4.2}$$

Some techniques explores also extra-transformations before detection, as applying an energy operator or the wavelet transform. Concluding detection, each putative waveform, which is 2 to 3 ms in duration, is stored. Alignment of the spikes can be performed interpolating with cubic splines to improve the detection of the peak, and finally returning to the decimated original sampling rate.

Feature extraction
The most simple feature to extract is the amplitude of the spike, but it's relevant to consider that neurons can have different shape but same peak amplitude. Another technique is based on creating a template for each nuerons and then assigning each spike to a template using a distance metric. This approach cannot easily distinguish nonstationary neurons, epecially if the firing of the neuron is not present when the templates are established.

High dimensionality is also a concern, since if M samples are stored for each waveform, its shape is represented in an M-dimensional space. The complexity of performering clustering operations in high-dimensional spaces requires dimensionality reduction, to obtain the minimal set of features that best discriminate the neurons.

To perform dimensionality reduction, **Principal Component Analysis** (PCA) is one of the most common methods. PCA is a dimensionality reduction and feature extraction technique used to identify the principal directions of variability in a dataset (Figure 4.12). By organizing the signals (waveforms) into a matrix

$$X \in \mathbb{R}^{N \times M} \tag{4.3}$$

where M is the number of samples and N is the number of signals, and centering them with respect to their mean $\bar{X}$, we obtain:

$$\tilde{X} = X - \bar{X} \tag{4.4}$$

The covariance matrix is then computed as:

$$C = \frac{1}{M-1}\tilde{X}\tilde{X}^T = V\Lambda V^T \tag{4.5}$$

which is decomposed into the eigenvector matrix V and the eigenvalue matrix Λ of C [88]. Usually a certain number K of principal components is mantained, keeping a high percentage of energy of the signal. So the feature space is reduced from dimensionality K to M, with K « M.

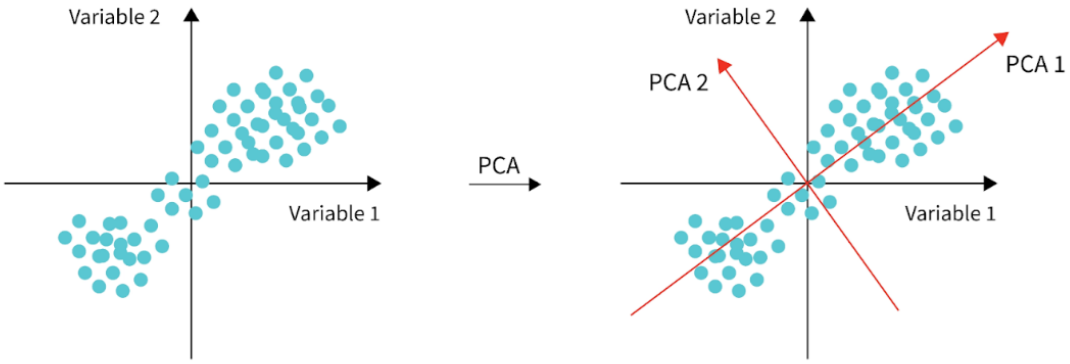

Figure 4.12: Example of the first two principal components for an example of data represented in a two-dimensionality space [89].

The most common alternative technique to PCA for feature reduction is the use of wavelets coefficients. The signal is decomposed using convolution between detected waveforms and wavelets functions, that are dilated and shifted versions of a "mother wavelet", leading to a set of coefficient that represent signal decomposition. To automatically select wavelets coefficient to actually discriminate neurons, Kolmogorov- Smirnov test for normality can be used to select only the first 10 coefficients with the most deviation from normal distribution.

Clustering
Clustering groups points (waveforms) into clusters, where every cluster correspons to a different neuron. Clustering can be performed manually by an expert user, analyzing a 2 or 3 dimensionality space, but this can bring error in the clustering process caused by low dimensionality visualization and human bias. Clusters can be estimated using an Expectation Maximization procedure assuming a for clusters to have a Gaussian distribution. since this assumption is not always true, an alternative is to use a mixture of distributions, like t-distributions, with a wider tail. Another option is the use of hierarchical clustering. Other commonly used clustering algorithms are k-means, Fuzzy c-means, Watershed algorithms, and Superparamagnetic clustering [90].

K-means [91] is a partitioning clustering algorithm designed to categorize a given dataset into k distinct clusters. This method iteratively refines cluster assignments, converging towards a local minimum.

The algorithm operates in two main stages. Initially, k cluster centers are randomly chosen, where k is predefined. Then, each data point is assigned to its nearest cluster center based on Euclidean distance. Once all points are assigned, an initial clustering is established. The next step involves recalculating the centroid of each cluster, and this iterative process continues until a stopping criterion, such as minimizing the objective function, is met.

Let x be a data point and $\bar{x}_i$ represent the centroid of cluster C_i. The objective function, which measures the sum of squared errors, is defined as:

$$E = \sum_{i=1}^{k} \sum_{x \in C_i} \|x - \bar{x}_i\|^2 \tag{4.6}$$

where E denotes the total squared error across all clusters.

The Euclidean distance, which determines the similarity between a point $x = (x_1, x_2, \ldots, x_n)$ and another point $y = (y_1, y_2, \ldots, y_n)$, is computed as:

$$d(x, y) = \sqrt{\sum_{i=1}^{n}(x_i - y_i)^2} \tag{4.7}$$

Procedure:

1. Randomly select k data points from D as initial cluster centers.
2. Repeat:
    1. Compute the distance between each data point d_i $(1 \leq i \leq n)$ and all cluster centers c_j $(1 \leq j \leq k)$.
    2. Assign each data point to the cluster with the nearest center.
    3. Recalculate the centroid for each cluster.
3. Continue iterating until convergence is achieved.

Chapter 5

Materials and Methods

5.1 Dataset

In this observational, descriptive, retrospective, monocentric, and non-profit study, data regarding patients affected by primary and secondary dystonia treated with GPi-DBS between 2020 and 2024 at the Meyer University Hospital IRCCS in Florence were examined by the team of Professor Flavio Giordano.

5.1.1 Patients and Clinical Evaluation

The study population consisted of 5 patients, including 2 males and 3 females. Robotic techniques were used to perform bilateral GPi-DBS surgery on each patient. Primary or secondary dystonia diagnosis, any age at diagnosis, any length of disease before surgery, GPi-DBS surgery, and the availability of MER obtained during the procedure were the inclusion criteria. As for the exclusion criteria: absence of available MER, stimulation of anatomical targets different from GPi (e.g., STN or thalamus). For each patient, the following variables were available: sex, clinical picture, cause of dystonia, age at the time of surgery, types of IPG and electrodes used, implant site, follow-up duration, presence of complications, MER used for electrode placement on the right and left sides, and trajectory and depth of electrode implantation on the right and left sides.

The process was carried out with complete patient anonymity, as the MER signals were not saved by name but by the patient's surgery date. From this, it was then possible to trace the patients' identities and proceed with the collection and analysis of clinical data. Subsequently, each patient was assigned a number from 1 to 5 to allow for unique identification of each study participant while ensuring complete anonymity.

Table 5.1 summarizes the patients' characteristics, clinical picture, and etiology of dystonia, while table 5.2 summarizes the data related to the surgical procedure.

Patient	**Sex**	**Clinical Picture**	**Etiology**
P1	F	Spastic dystonic tetraparesis	Genetic
P2	F	Generalized dystonia	Genetic (KMT2B)
P3	M	Generalized dystonia	PCI
P4	M	Generalized dystonia	Genetic (PRKARA - DYT16)
P5	F	Generalized dystonia	PCI

Table 5.1: Sex, clinical picture, and etiological cause of dystonia for each of the five patients.

Patient	**Age**	**Target**	**R. T.**	**IPG Model**	**Electrode Model**	**IPG Location**	**Compl.**
P1	12	Bi. GPi	Yes	Med. Activa RC	Med. 3387	Subclavicular	None
P2	16	Bi. GPi	Yes	Med. Activa RC	Med. 3387	Subclavicular	None
P3	11	Bi. GPi	Yes	Med. Activa RC	Med. B33015	Subclavicular	None
P4	6	Bi. GPi	Yes	Med. Activa RC	Med. 3387	Abdomen	None
P5	12	Bi. GPi	Yes	Med. Percept RC	Med. B33015	Subclavicular	None

Table 5.2: Age at the time of GPi-DBS surgery (years), surgical target, surgical technique, IPG model, electrode model, IPG location, and complications. Abbreviations: Bi. (Bilateral), R.T. (Robotic Techniques), Med. (Medtronic), compl. (complications).

Regarding the assessment of patient outcomes, the Burke-Fahn-Marsden Dystonia Rating Scale (BFMDRS) was used. This scale consists of a preoperative clinical evaluation and an evaluation during patient follow-up. The BFMDRS values are based on data collected during telephone interviews, follow-up visits, and electronic medical records.

The BFMDRS was the first assessment scale historically developed for dystonia. It is now a standard tool used to evaluate the severity of generalized dystonia. It consists of two subscales: the Burke-Fahn-Marsden Movement Scale (BFMMS) and the Burke-Fahn-Marsden Disability Scale (BFMDS).

The BFMMS evaluates two separate factors: a severity factor, which measures the intensity of dystonic movements, and a provocative factor, which assesses

the circumstances that trigger dystonia, such as whether the patient is at rest or active. The scale measures dystonia in nine body regions: eyes, mouth, speech and swallowing, neck, left and right arms, left and right legs, and trunk. Each area is assigned a score from 0 (no dystonia) to 4 (severe dystonia) for severity, and from 0 (no dystonia at rest or during activity) to 4 (dystonia at rest) for the provocative factor. The severity factor is multiplied by the provocative factor, and the result is then multiplied by a weighting factor (0.5 for eyes, mouth, and neck; 1 for the other areas). This gives a final score for each area, and the scores are summed. The maximum possible score on the BFMMS is 120.

The BFMDS asks the patient to self-assess their disability in performing seven daily activities: speech, writing, eating, swallowing, personal hygiene, dressing, and walking. Each activity is assigned a score from 0 (no disability) to 4 (complete disability), except for walking, which is scored from 0 to 6, considering whether the patient needs assistance and, if so, the type of assistance. The scores are summed, with a maximum possible score of 30 [92].

Table 5.3 summarizes the data relative to preoperative and most current follow up evaluation, with the corresponding percentage of improvement.

Patient	**BFMDRS Motor t-0**	**BFMDRS Motor t-uf**	**BFMDRS Disability t-0**	**BFMDRS Disability t-uf**	**BFMDRS Motor variation (%)**	**BFMDRS Disability variation (%)**
P1	35	59.5	20	21	70.0%	5.0%
P2	42	31.5	17	12	-25.0%	-29.4%
P3	94.5	49.5	25	20	-47.6%	-20.0%
P4	50.5	2	21	18	-96.0%	-14.3%
P5	73	53	21	14	-27.4%	-33.3%

Table 5.3: BFMDRS scores and improvements for each patient. t-0: pre-surgery, t-uf: follow-up.

From Table 5.3 it can be noted that patient 1 is the only one who underwent a deterioration following the surgery, with an increase of both motor and disbility BFMDRS with respect to preoperatory evaluation. The outcome is classified as negative. The remaining patients, from 2 to 4, experienced a a reduction in the BFMDRS score, indicating an improvement in clinical conditions.

5.1.2 Recordings

Electrophysiological MER recordings were acquired for each of the five patients during the GPi-DBS surgery. For patients 1 to 4, the recordings were made using the LeadPoint system (Medtronic [93]) at a sampling frequency of 24000 Hz, while for patient 5, the NeuroSmart system (Alpha Omega Engineering [94]) was used at

a sampling frequency of 24341 Hz.

Data were collected from each cerebral hemisphere (right and left) using three of the five microelectrodes that make up the standard "Ben's-Gun" cross model, as cited in previous chapters. The selected electrodes were the anterior, central, and posterior ones. Each of the three electrodes will be referred to as a 'trajectory'. The target position was initially estimated using preoperative imaging. Considering the target position at 0 mm, the MER recordings were performed at depth intervals of 1 mm, 2 mm, or 0.5 mm, starting from a maximum of 10 mm above the target (negative depth) to a minimum of 2.5 mm below the target (positive depth). In Figure 5.1 an infographic about dataset structure is shown.

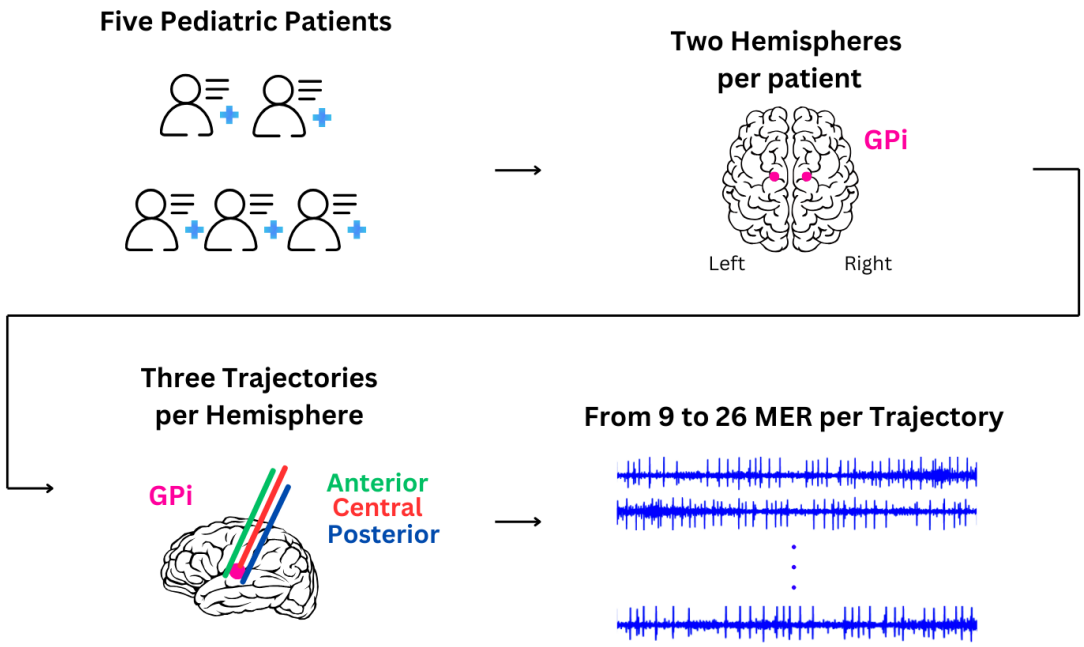

Figure 5.1: Infographic about dataset structure. The dataset is composed of five pediatric patients, operated bilaterally of DBS GPi. Three trajectories were used to record MER data intraoperativelly, anterior, central and posterior. For each trajectory, a number of recordings varying from 9 to 26 were acquired.

Table 5.4 details the number of recordings made for each patient and hemisphere. The number of recordings (or traces) and the depths explored for each hemisphere are identical across the three trajectories, as the data are simultaneously acquired along them. The table should be interpreted as follows: for patient 1, from the right hemisphere, 18 traces of 3 seconds were recorded from the anterior electrode,

18 traces of 3 seconds from the central electrode, and 18 traces of 3 seconds from the posterior electrode. A total of 486 MER traces were available.

Patient	Hemisphere	Number of Recordings	Duration (s)
P1	Left	18	3
P1	Right	26	3
P2	Left	23	10
P2	Right	18	10
P3	Left	18	10
P3	Right	12	10
P4	Left	9	3
P4	Right	12	3
P5	Left	11	6
P5	Right	15	6

Table 5.4: Number of MER recordings and their duration for each hemisphere of each patient.

The data were labeled using the information regarding the depth at which the DBS device was actually implanted, along with the outcome of the surgery, which is either positive or negative. A positive outcome is determined by an improvement in the patient's condition, while a negative outcome indicates a worsening. The outcome for each patient was determined following the procedure described in the previous paragraph. Table 5.5 provides an indication of the trajectory chosen for the implantation, as well as the depth at which the DBS stimulation electrode was positioned for each patient and each hemisphere.

The visualization and analysis of the data were performed using MATLAB software [95]. In Figure 5.2, an example of a MER trace can be found, while in Figure 5.3, all the available MER for patient 1 are shown.

5.2 Data Conversion

The data acquired with the Leadpoint system was already saved in μV in a format ".txt" file. Depth of each recording was gathered from a file having ".xml" format, unique for each patient. The signals were bandpass-filtered in the bandwidth 500-5000 Hz during the surgery using the acquisition system.
Regarding data acquired with the Neurosmart system, they were initially saved in ".mpx" format. Each recording was converted into a ".mat" format file using the proprietary software. The converted files contained each spike recording in

Patient	Hemisphere	Trajectory	Depth (mm)	Outcome
P1	Right	Anterior	0	Negative
	Left	Central	0	
P2	Right	Central	+0.5	Positive
	Left	Central	+0.5	
P3	Right	Posterior	0	Positive
	Left	Central	0	
P4	Right	Central	-1	Positive
	Left	Posterior	-1	
P5	Right	Central	0	Positive
	Left	Posterior	0	

Table 5.5: Information on the trajectory and depth chosen by the surgeon for the DBS electrode implantation for each patient. The last column contains the patient's outcome, which was used to classify the recordings.

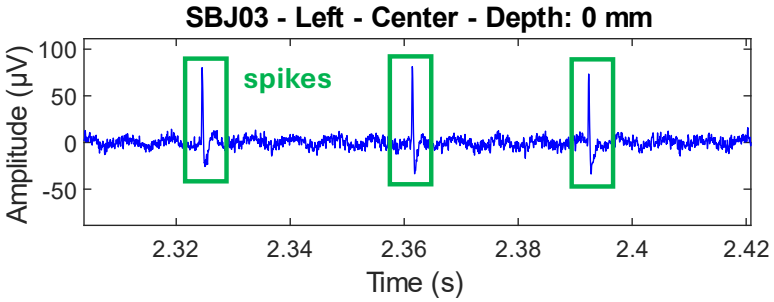

Figure 5.2: Example of MER extract gathered from patient 3, left side, central trajectory at 0 mm depth. In blue, the raw MER signal is shown. In green, neuronal spikes are highlighted.

A/D values, already bandpass filtered in 300-9000 Hz bandwidth. Using a Gain of 1392 and a Bit Resolution of 630 μV / A/D value, signals in μV were obtained by multiplying original signal for the Bit Risolution and dividing by the Gain. For the patient acquired with Neurosmart system, LFPs were also available, but not for other patients, so LFPs were excluded from the following analysis.

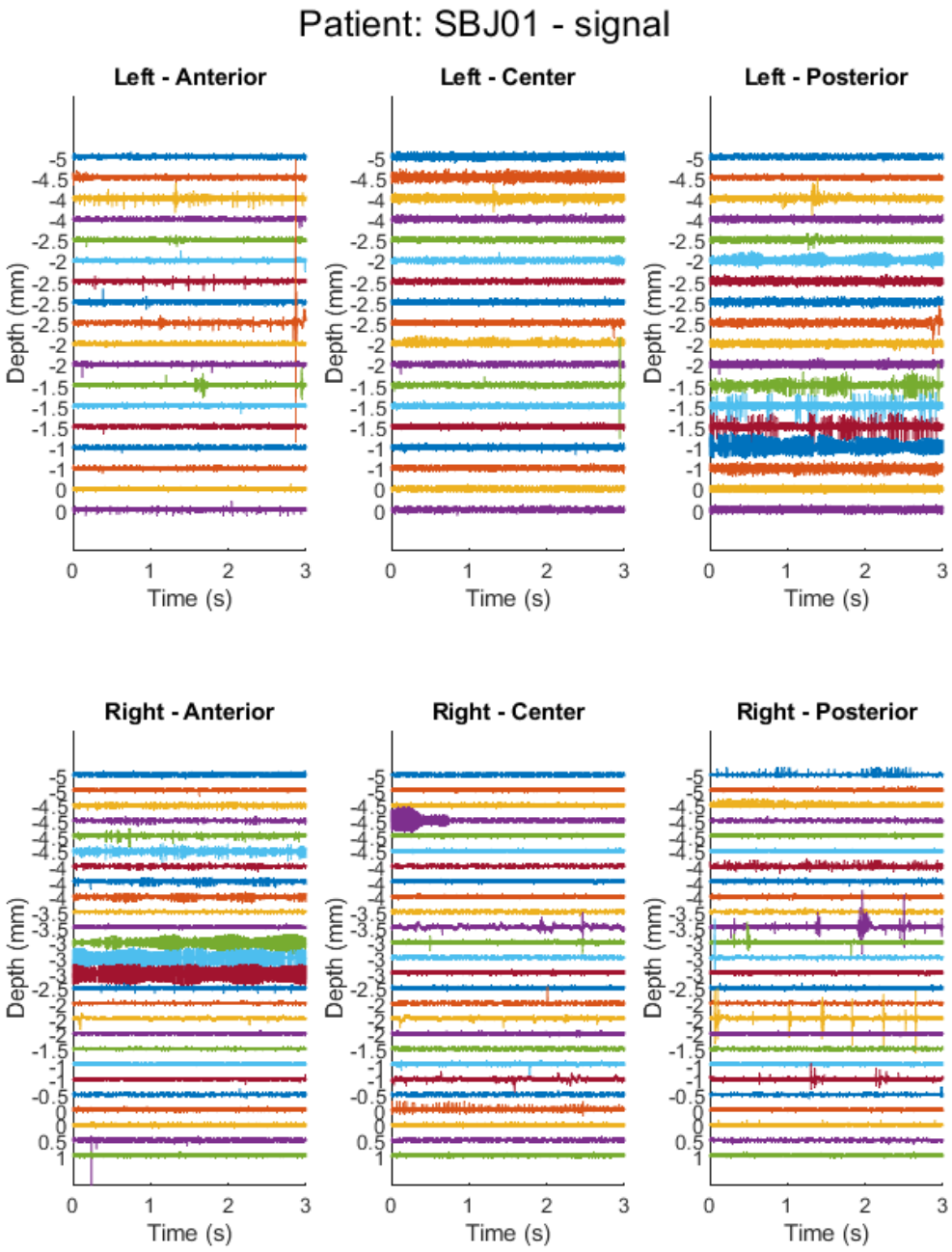

Figure 5.3: Example of MER for patient 1, with indications about the depth of each MER.

5.3 Processing Steps

The MER signal processing steps were designed to automatically analyze the neural activity recorded during the GPi-DBS procedure in detail. Initially, the SUA of neurons was examined. The SUA analysis was preceded by a band-pass filtering process aimed at isolating the characteristic frequencies of action potentials, followed by artifact identification. Next, an automatic spike sorting algorithm was applied, allowing the identification and classification of action potentials from different neurons. Various features were obtained from stable neurons. Subsequently, the signal was processed to extract spectral information related to MUA. Afterward, temporal features were extracted from the signal. Finally, the totality of extracted features were statistically analyzed to identify the most significant ones concerning the implantation depth of the device during the procedure. A flowchart of the followed pipeline is shown in Figure 5.4.

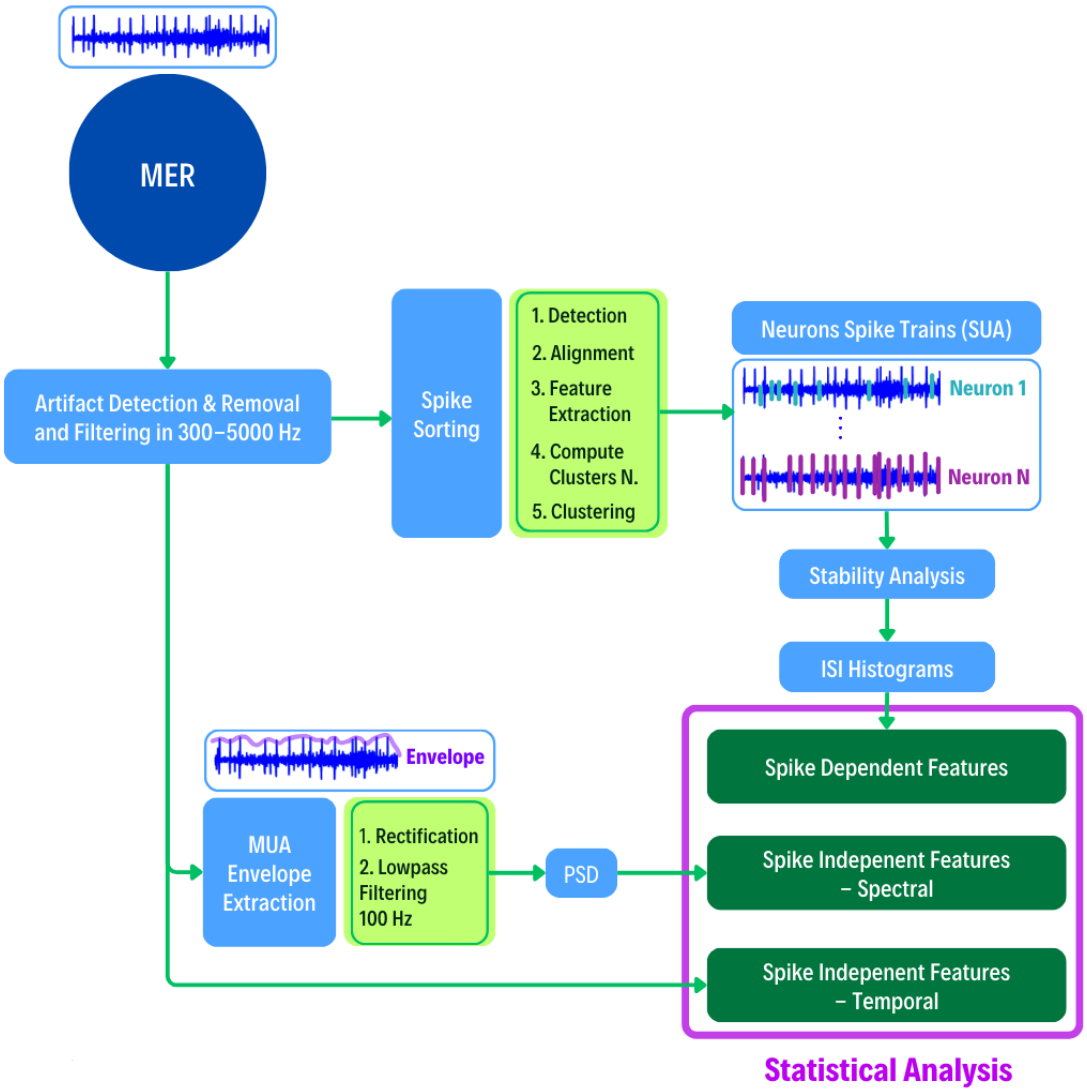

Figure 5.4: Flowchart of the proposed processing pipeline. Starting from the MicroElectrode Recording (MER), the signal is cleaned and filtered. This signal undergoes spike sorting to identify Single Unit Activity (SUA). From each neuron SUA, a neuron is determined to be stable or not. From stable neurons their InterSpike Interval (ISI) histogram is computed, and from it a variety of spike dependent features are determined for each neuron. The cleaned and filtered signal is also used to compute Multi Unit Activity (MUA) envelope, from which Power Spectral Density (PSD) is derived. Spectral features are obtained from PSD. Temporal features are also computed from the cleaned signal.

5.3.1 Artifacts removal and filtering

Initially, corrupted signals were excluded by assessing the percentage of MER absolute samples exceeding 100 µV, as action potentials (APs) typically have amplitudes around 50-100 µV [75]. If this percentage exceeded 3%, the MER track was not analyzed. A signal was considered corrupted if the artifact was not localized to specific time intervals but rather distributed throughout the entire recording, indicating contamination that could compromise its reliability for subsequent analysis. Corrupted signals are shown in Figure 5.5.

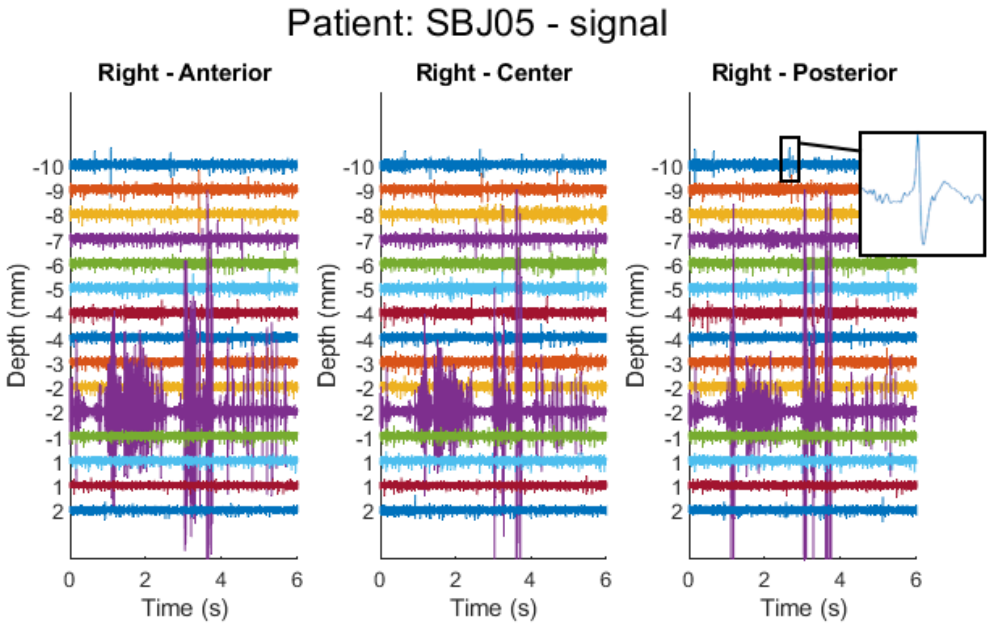

Figure 5.5: Example of corrupted signals (indicated in purple at depth -2 mm) and a zoom of a clean portion of data, where a spikes is visible. Recording from patient 5, right hemisphere.

Denoising of valid MER was performed through a two-step procedure:

2) High-amplitude and energy artifact of transient nature were identified using variance. The signal was split into 50 ms overlapping epochs with a 10% overlap in order to detect high-energy artifacts and interferences unrelated to spikes. Epochs were deemed artifacts and disqualified from further analysis stages if their variance was more than 5.5 times the signal's global variance. Epochs identified as noise were removed using cubic spline interpolation. The use of variance for the exclusion of epochs and noisy spikes has been employed in other studies, such as those by Koirala et al. (2020) [96] and Toosi et al. (2021) [97]. An example of epoch identified as artifact is shown in Figure 5.6.

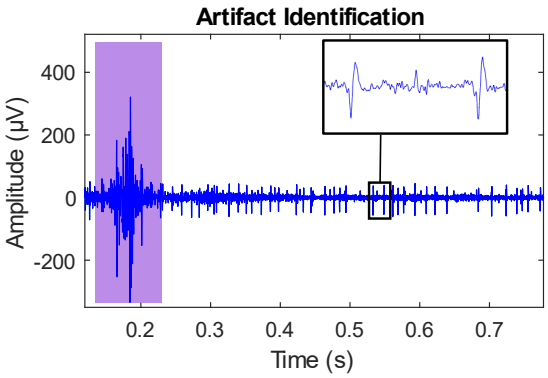

Figure 5.6: Example of an artifact (indicated in purple) and a zoom of a clean portion of data, where two spikes are clearly visible. Recording from patient 2, left hemisphere, anterior trajectory, at depth -4 mm.

3) Frequency components between 300 and 5000 Hz were isolated using a fourth-order Butterworth band-pass filter [82, 81]. In order to ensure phase correction and maintain the action potentials' original shape, the filter was implemented using zero-phase filtering technique.

5.3.2 Spike Sorting

The current section will describe the automatic spike sorting pipeline used to obtain SUA from the MER signals.

Spikes Detection

The spike detection phase was implemented using a median-based threshold approach, as described in Reference [87] and previous chapters, with a factor k of 4.5, as shown in Equation 5.1.

$$\text{Threshold} = k \cdot \frac{\text{median}(|X|)}{0.6745} \tag{5.1}$$

The threshold was applied to both signal polarities (positive and negative). The detected spikes that were contained in epochs previously identified as artifacts were excluded from subsequent analysis to prevent noisy components from compromising the final results. Furthermore, a minimum interval of 1.5 ms was enforced between detected peaks, which corresponds to about half of the absolute refractory period of a neuron. Figure 5.7 shows an example of identified spikes in a MER trace using

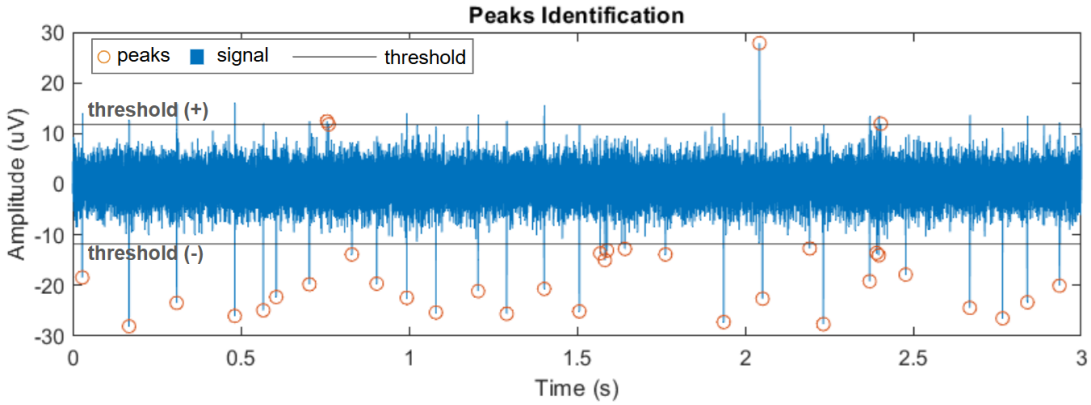

Figure 5.7: Example of spikes identified through the threshold in Equation 5.1 for patient 1, left hemisphere, anterior trajectory, depth 0 mm.

this method.

Next, starting from each detected minimum or maximum, a time window of 2 ms was opened (0.50 ms before and 1.50 ms after the peak), from which the waveform of the single spike was extracted. Finally, each detected event was temporally aligned so that the actual maximum or minimum of the waveform was at the same sample for all detected waveforms, optimizing detection accuracy and improving the precision of the following analysis steps. This was achieved by oversampling the signal with a factor of 10 using cubic spline interpolation, aligning the peak to a fix sample, and then downsampling to the original sampling frequency.

Feature extraction

The waveforms were standardized using z-score, meaning the removal of the mean and division by the standard deviation. Subsequently, PCA was performed on the precedently standardized waveforms. The components explaining 95% of the total variance were selected, to make sure of the preservation of most of the significant information in the data. However, the number of components was limited to 15 [97] to mitigate the negative effects of the Curse of Dimensionality, a phenomenon that can decrease the effectiveness of clustering techniques in high-dimensional spaces [98]. Figure 5.8 shows an example of the representation of the waveforms through their projection along the first 3 principal components. An additional feature was included in the PCA-derived features, which is the signal value at the peak (minimum or maximum) identified by the waveform, to account for the

polarity and amplitude of the waveform during the clustering phase.

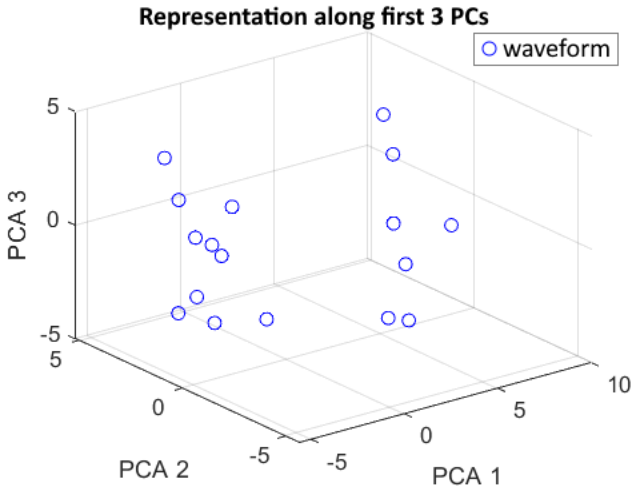

Figure 5.8: Example of waveforms represented in the first 3 principal components space for MER of patient 1, left hemisphere, anterior trajectory, depth -2.5 mm.

Clustering

For clustering, the Gap Statistic [99] was used to determine the optimal number of clusters k by comparing the log of the within-cluster sum of distances to its expected value under a reference distribution. The Gap Statistic is defined as:

$$\text{Gap}_k = E^*[\log(W_k)] - \log(W_k), \tag{5.2}$$

where W_k represents the within-cluster sum of distances.

Our dataset consists of p features measured on n independent observations, denoted as x_{ij}, where $i = 1, 2, \ldots, n$ and $j = 1, 2, \ldots, p$. The pairwise distance between observations i and i' is defined as:

$$d_{ii'} = \sum_j (x_{ij} - x_{i'j})^2. \tag{5.3}$$

If the data is clustered into k clusters $C_1, C_2, \ldots, C_k$, with C_r denoting the indices of observations in cluster r, and $n_r = |C_r|$, the total within-cluster sum of distances is:

$$D_r = \sum_{i,i' \in C_r} d_{ii'}, \tag{5.4}$$

$$W_k = \sum_{r=1}^{k} D_r. \tag{5.5}$$

The optimal number of clusters is chosen as the smallest k such that:

$$\text{Gap}_k \geq \text{GAP}_{\max} - SE(\text{GAP}_{\max}), \tag{5.6}$$

where:

- K is the number of clusters,
- Gap_k is the gap value for the clustering solution with K clusters,
- $\text{GAP}_{\max}$ is the maximum observed gap value,
- $SE(\text{GAP}_{\max})$ is the standard simulation error associated with $\text{GAP}_{\max}$.

The simulation error for the k-cluster is:

$$\text{SE}_k = \sqrt{1 + \frac{1}{B}} \cdot \text{sd}(k), \tag{5.7}$$

with B being the number of bootstrap samples.
The computation of the Gap Statistic follows these steps:

1. Cluster the observed data for $k = 1, 2, \ldots, K$, computing W_k.
2. Generate B reference datasets, cluster each, and compute W_k^*.
3. Estimate the Gap Statistic as:

$$\text{Gap}_k = \frac{1}{B} \sum_{b=1}^{B} \log(W_k^*) - \log(W_k). \tag{5.8}$$

4. Compute the standard deviation:

$$\text{SE}_k = \sqrt{\frac{1}{B} \sum_{b=1}^{B} \left(\log(W_k^*) - \bar{W_k}\right)^2}. \tag{5.9}$$

5. Select the optimal k using the Gap Statistic condition.

The reference distribution is generated by sampling data points uniformly within a hyper-rectangle aligned with the principal components of the data matrix X. Given an $n \times p$ data matrix X, assuming zero-mean columns, we compute its singular value decomposition (SVD):

$$X = UDV^T. \tag{5.10}$$

The data is then transformed using:

$$X' = XV. \tag{5.11}$$

Reference features Z' are sampled uniformly within the range of each column of X', then back-transformed:

$$Z = Z'V^T. \tag{5.12}$$

This ensures that reference features are uniformly distributed within a box aligned with the principal components of the dataset.

The optimal k is determined as the smallest value between 1 and 8 [100] that satisfies:

$$\text{Gap}_k \geq \max(\text{Gap}_k) - \text{SE}(\text{Gap}_k), \tag{5.13}$$

where $\text{SE}(\text{Gap}_k)$ is the standard error of the Gap Statistic.

An example of identification of the number of clusters is shown in Figure 5.9.

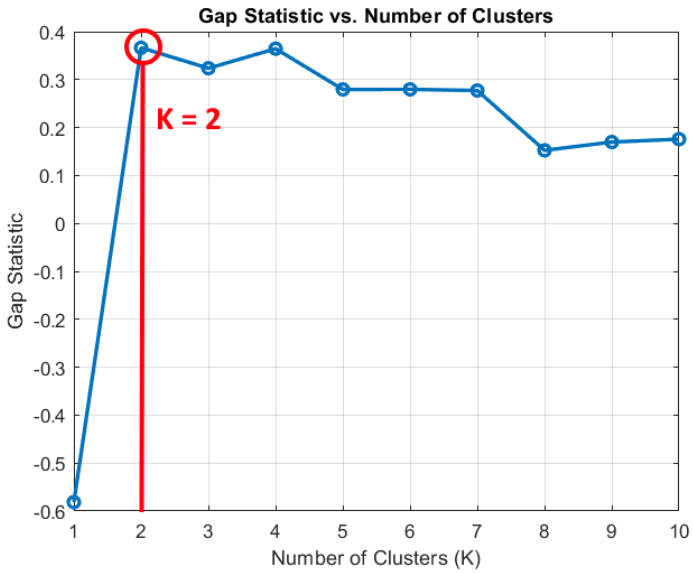

Figure 5.9: Gap Statistic value calculated for a certain number of clusters (from 1 to 10) for Patient 1, left side, anterior trajectory, depth 2.5 mm. The cluster value with the best Gap is marked in red.

Once the optimal k is identified, the k-means algorithm assigns each spike to its respective cluster by minimizing the Euclidean distance to the centroids:

$$C_i = \arg\min_j ||x_i - \mu_j||^2, \tag{5.14}$$

where x_i is a data point, and μ_j represents the centroid of cluster j.

An example of clustering result is shown in Figure 5.10 and 5.11.

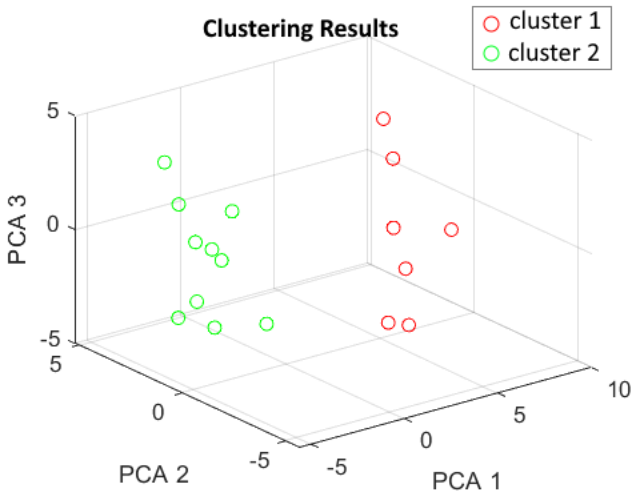

Figure 5.10: Example of clustering results in the first 3 principal components space for MER of patient 1, left hemisphere, anterior trajectory, depth -2.5 mm. Two clusters are obtained from the clustering process.

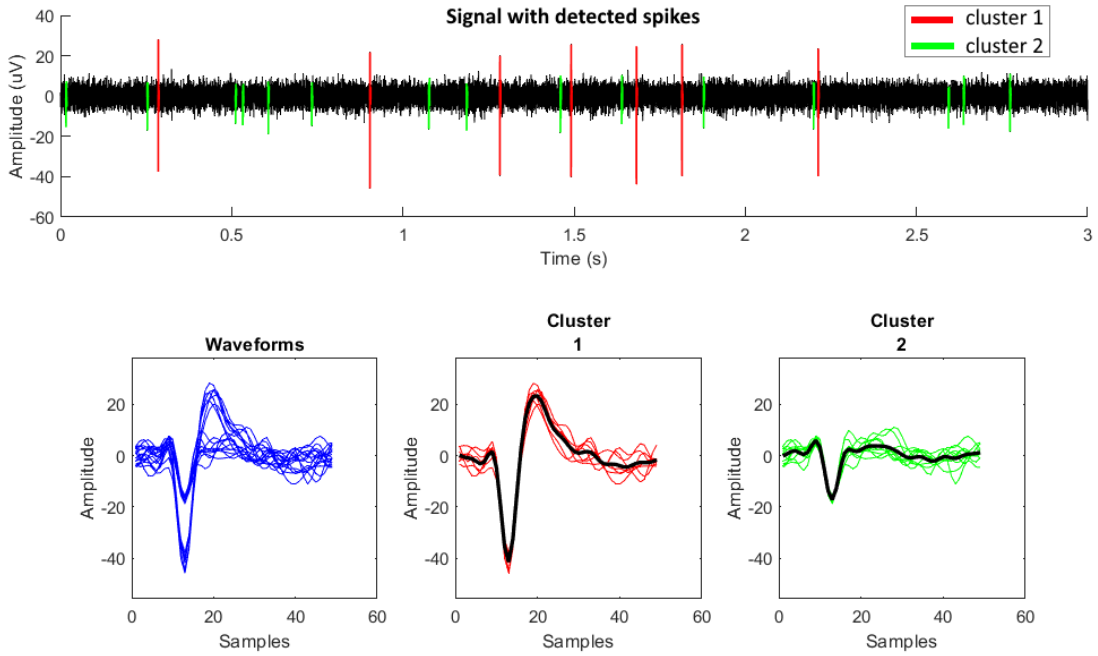

Figure 5.11: Example of waveform separation from patient 1, left side, anterior trajectory, depth -2.5 mm. On top, representation of the signal with identified waveforms highlighted in different colors, each corresponding to a different cluster. On the second row, aligned waveforms of each cluster, with the average template shown in black.

5.3.3 Spike-Dependent Features

From firing istants of each identified neuron, the Inter-Spike Interval (ISI) histogram was computed for each neuron. This histogram represents the temporal distribution of intervals between consecutive spikes, giving information about firing dynamics of the neuron. An example of ISI histogram in shown in Figure 5.12.

Neural Stability

Before proceeding with the extraction of features, neural stability criteria were applied to ensure the reliability of the following analyses. A neuron is considered stable if less than 5% of the neuron's waveforms have an ISI shorter than 3 ms (corresponding to the absolute refractory period of a neuron) [101]. Also, a minimum of 10 waveforms per neuron to ensure statistically meaningful and robust considerations. To be stable, the Signal-to-Noise Ratio (SNR) of the cluster, calculated as the difference between the maximum and minimum values of the mean waveform, divided by the detection threshold (Equation 5.1, must be greater

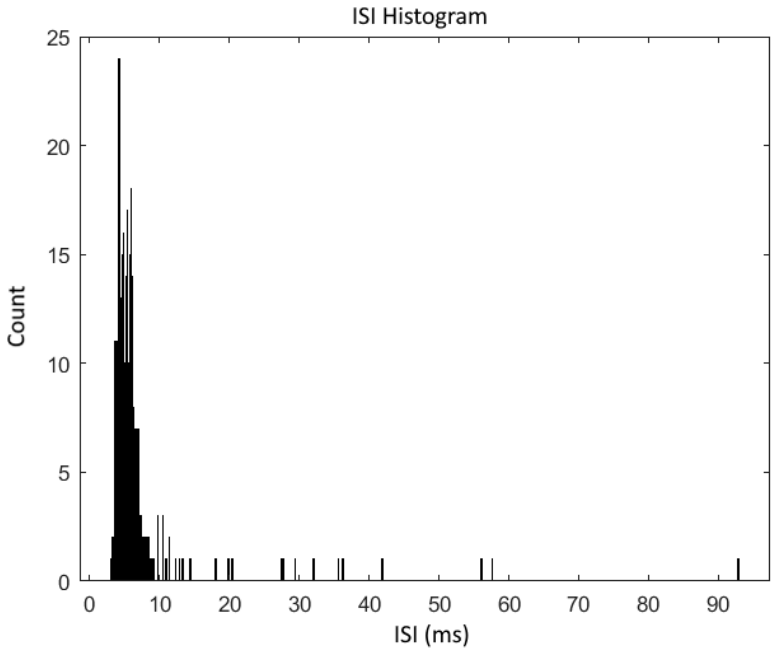

Figure 5.12: Example of an ISI histogram of a neuron, showing the count of ISI intervals with a given duration (ms). Example taken from Patient 1, left side, posterior electrode, depth -1 mm.

than 1.5 [102].

These quantities calculated to perform the stability check were saved for stable neurons and used as features to characterize the various recording groups. These features, called stability features, are listed below for completeness:

- **Number of spikes**:
  The total number of spikes recorded for each neuron.
- **SNR**:
  The signal-to-noise ratio of the waveform template, calculated as:
  $$\text{SNR} = \frac{\min(\text{waveform}) - \max(\text{waveform})}{4.5 \cdot \sigma} \tag{5.15}$$
- **Percentage of close spikes**:
  The percentage of spikes with an Inter-Spike Interval (ISI) shorter than 3 ms, calculated as:
  $$\%\ \text{Close Spikes} = \frac{\sum(\text{ISI} < 3\ \text{ms}) \cdot 100}{N} \tag{5.16}$$
  where N is the total number of spikes for the neuron.

Single-Unit-Activity Features

Starting from the ISI histogram, a series of features were calculated that describe in detail the firing behavior of neurons over time. The following features, inspired by the works of Kaymak et al. (2023) [103] and Chaovalitwongse et al. (2011) [104], will be listed and described.

- **Firing Rate**:
  The firing rate (λ) represents the average number of spikes per second of a neuron and provides a direct measure of its activity. It is one of the most widely used biomarkers in neural data analysis, because it reflects the overall activation level of the neuron. It is calculated by fitting the ISI histogram with a Gamma distribution, as shown in Equation 5.17 [105]:

$$g_{\lambda,\kappa}(I) = \frac{(\lambda k)^{\kappa} I^{\kappa-1} e^{-\lambda k I}}{\Gamma(\kappa)} \tag{5.17}$$

  Where I is the duration of a given interspike interval (ISI), λ and κ represent the firing rate and the shape factor, respectively, and $\Gamma(\kappa)$ is the Gamma function. The firing rate is obtained by calculating the scale factor of the distribution and taking its inverse.

- **Regularity**:
  This metric quantifies the regularity of a neuron's firing, calculated from the logarithm of the shape parameter κ estimated from the Gamma distribution fit to the ISI curve. It has been used to classify neurons into subcategories based on their behavior, dividing them into bursting, tonic, and irregular categories. Formula 5.18 describes how regularity is calculated and how neurons are classified based on it. In the case of the additional criterion, it checks that 70% of the ISI values lie within an interval dependent on the firing rate [106].

  The regularity criterion is given by the logarithm of the shape parameter k (estimated from the Gamma distribution fit to the ISI data):

$$\text{Regularity} = \log(k) \tag{5.18}$$

  Based on the value of $\log(k)$, the classification is as follows:

$$\text{Neuron classification:} \begin{cases} \log(k) > 0.3 & \text{Neuron is Bursting,} \\ -0.3 \leq \log(k) \leq 0.3 & \text{Neuron is Irregular,} \\ \log(k) < -0.3 & \text{Neuron is Tonic.} \end{cases} \tag{5.19}$$

$$\text{Additional Criterion:} \begin{cases} 70\% \text{ of samples } > |\lambda \pm 0.5\lambda| & \text{Neuron is Bursting,} \\ 70\% \text{ of samples } \leq |\lambda \pm 0.5\lambda| & \text{Neuron is Irregular.} \end{cases} \tag{5.20}$$

- **Coefficient of Variation (CV)**:
  The coefficient of variation of the spike train sequence was used to quantify the width of the ISI distribution. It serves as an additional measure of the irregularity of the spike train sequence, and it is calculated as in Equation 5.21 [107]:
  $$\mathrm{CV} = \frac{\mathrm{variance}^2(\mathrm{ISI})}{\mathrm{mean}} \tag{5.21}$$

- **Local Variation (LV)**:
  This metric is designed to determine the intrinsic temporal dynamics of spike trains. LV compares temporal variations with local rates and is defined for non-stationary processes [108]. In Formula 5.22, each value τ denotes the time of an observed spike, while N represents the total number of spikes in a spike train. Compared to the CV, it provides more robust results to distinguish the activity of different neurons. The formula compares each pair of consecutive ISIs, measuring how much one interval changes relative to the previous one, giving an indication of the variability of ISIs. It takes a value close to 0 when the firing pattern is regular and close to 1 if irregular:
  $$LV = \frac{3}{N-2} \sum_{n=0}^{N-1} \left(\frac{(\tau_{n+1} - \tau_n) - (\tau_n - \tau_{n-1})}{(\tau_{n+1} - \tau_n) + (\tau_n - \tau_{n-1})} \right)^2 \tag{5.22}$$

- **Mean of the ISI distribution (ISI_mean)**:
  The mean value of the ISI distribution represents the average temporal distance between two successive spikes of a neural structure, calculated as in Formula 5.23:
  $$ISI_{\mathrm{mean}} = \mathrm{shape}_{\mathrm{param}} \cdot \mathrm{scale}_{\mathrm{param}} \tag{5.23}$$

- **Standard Deviation of the ISI distribution (ISI_std)**:
  To define the dispersion around the mean of the ISI distribution, the standard deviation is calculated using Formula 5.24. This biomarker indicates the uncertainty of the duration between two successive spikes in spike trains. A greater dispersion around the ISI distribution indicates a wider range of temporal distances between spikes of the neuron:
  $$ISI_{\mathrm{std}} = \sqrt{\mathrm{shape}_{\mathrm{param}} \cdot \mathrm{scale}^2_{\mathrm{param}}} \tag{5.24}$$

- **Skewness of the ISI distribution (ISI_skewness)**:
  Skewness is a measure of the asymmetry of a function and how much the gamma distribution fitted to it deviates from a normal distribution. It is calculated as in Formula 5.25:
  $$ISI_{\mathrm{skewness}} = \frac{2}{\sqrt{\mathrm{shape}_{\mathrm{param}}}} \tag{5.25}$$

- **Pause Index**:
  The Pause Index measures the ratio between ISIs greater than 50 ms and those less than or equal to 50 ms.

- **Pause Ratio**:
  The Pause Ratio compares the total time of ISIs greater than 50 ms with that of ISIs less than or equal to 50 ms.

- **Burst Index (BI)**:
  The burst index is a metric used to evaluate possible variations in neural activation patterns, calculated as in Formula 12 [109, 110]:

$$\mathrm{BI} = \frac{\mathrm{mean}(ISI)}{\mathrm{mod}(ISI)} \tag{12}$$

Burst Features

A series of features were also computed based on the activity of neurons classified as bursting type. "Bursting" is a state in which a neuron repeatedly fires in groups or bursts of action potentials in a short temporal window.

There are various approaches in the scientific literature to detect bursting. In this case, a method called Rank Surprise (RS) [111] was used, as described below.

Let t_n be the occurrence time of the n-th spike in a sequence of $N+1$ spikes. The inter-spike interval (ISI) is defined as:

$$\mathrm{ISI}_n = t_{n+1} - t_n \tag{5.26}$$

Each ISI value is assigned a rank R_n, where the lowest value receives rank 1 and the highest value receives rank N. Under the assumption that ISIs are independent, the rank values R_n should also be independent and uniformly distributed between 1 and N.

A burst corresponds to a sequence of consecutive low R_n values. For a given firing sequence containing at least 3 spikes, the Rank Surprise (RS) statistic is computed as the log-likelihood:

$$RS = -\log\left(P_T(q \leq u)\right) \tag{5.27}$$

where $P_T(q \leq u)$ represents the Cumulative Distribution Function (CDF) of a discrete uniform sum distribution. The distribution of T_q, the sum of q discrete uniform variates between 1 and N, is given by:

$$P(T_q \leq u) = \frac{1}{N^q} \sum_{k=0}^{\lfloor (u-q)/N \rfloor} (-1)^k \frac{(u-kN)!}{k!(q-k)!(u-kN-q)!} \tag{5.28}$$

Thanks to the Central Limit Theorem, for $q \geq 30$, the following approximation can be used:

$$P(T_q \leq u) \approx \Phi\left(\frac{u - \frac{q(N+1)}{2}}{\sqrt{q(N^2-1)/12}}\right) \tag{5.29}$$

where Φ is the cumulative distribution function of the standard normal distribution.

A burst is detected when:

$$RS > RS_\alpha \tag{5.30}$$

where:

$$RS_\alpha = -\log(\alpha) \tag{5.31}$$

When RS exceeds a user-defined threshold RS_α, the interval is classified as bursting activity.

To enhance the detection of bursts, an approach called Exhaustive Surprise Maximization (ESM) was used. Before running the algorithm, two parameters are fixed:
- The maximum ISI value that can be considered within a burst (denoted as limit).
- A minimum significance level for the RS statistic, defined as $-\log(\alpha)$.

The algorithm follows these steps:
1. Identify the first sequence of ISIs where values are below the predefined limit.
2. Perform an exhaustive search to identify the subsequence that maximizes the RS statistic.
3. If the maximum RS statistic exceeds $-\log(\alpha)$, the corresponding subsequence is labeled as a burst.
4. Continue searching for additional bursts in the remaining ISI subsequences following the same criteria.
5. The process repeats until no further subsequence satisfies the significance threshold.
6. The search then moves to the next sequence of ISIs below limit, repeating the process.

To ensure validity, the 75th percentile of the ISI histogram was chosen as the minimum ISI value required for a burst. Additionally, a significance level of $\alpha = 0.03$ was set as the minimum threshold to validate a burst region.

From the algorithm's output, the following features were calculated:

- **Bursting spike proportion**:
  This metric represents the proportion of spikes occurring within bursting intervals relative to the total number of spikes in the spike train, as shown in the equation:

$$\text{bspike\_proportion} = \frac{\sum_{n=1}^{N_{\text{bursts}}} \text{count}_n(\text{spikes})}{\text{count(all spikes)}} \tag{5.32}$$

- **Average number of spikes per burst**:
  This metric represents the average number of spikes observed within each bursting interval:

$$\text{burst\_avg\_spikes} = \frac{1}{N_{\text{bursts}}} \sum_{n=1}^{N_{\text{bursts}}} \text{count}_n(\text{spikes}) \tag{5.33}$$

- **Inter-Burst Interval**:
  This metric represents the average temporal distance between two consecutive bursts:

$$\text{interbi} = \frac{1}{N_{\text{bursts}} - 1} \sum_{n=1}^{N_{\text{bursts}}} (\tau_{\text{burst\_start},n+1} - \tau_{\text{burst\_finish},n}) \tag{5.34}$$

- **Intra-Burst Frequency**:
  This metric represents the average firing frequency during bursting periods:

$$\text{intrabf} = \frac{1}{N_{\text{bursts}}} \sum_{n=1}^{N_{\text{bursts}}} \frac{\text{count}_n(\text{spikes})}{(\tau_{\text{finish},n} - \tau_{\text{start},n})} \tag{5.35}$$

- **Intra-Burst Interval**:
  This metric represents the average duration of bursting activity within the spike train:

$$\text{intrabi} = \frac{1}{N_{\text{bursts}}} \sum_{n=1}^{N_{\text{bursts}}} (\tau_{\text{burst\_finish},n} - \tau_{\text{burst\_start},n}) \tag{5.36}$$

Figure 5.13 illustrates an example of bursting activity detected using the RS method.

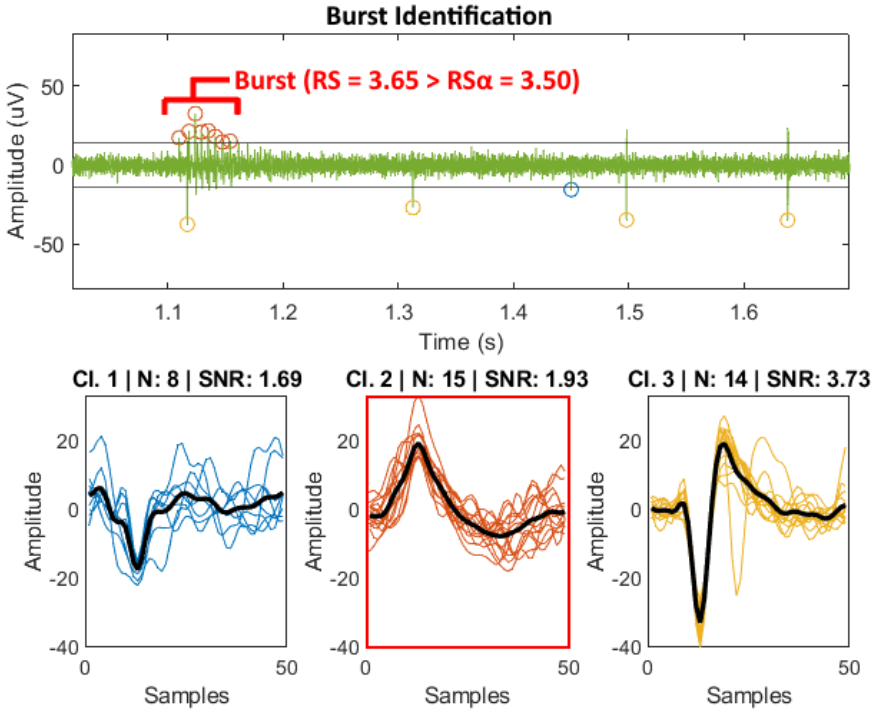

Figure 5.13: First row: example of bursting activity detected using the Burst Surprise method. The sequence highlighted in red has an RS value greater than RS alpha and is therefore considered a "burst". On the second row are represented the clusters identified from MER, with the bursting neuron highlighted in red. Example taken from Patient 1, left side, anterior electrode, depth -4.5 mm.

5.3.4 Spike-Independent Features

Multi-Unit-Activity Spectral Features

Neural oscillations are influenced by synchronization across different scales, ranging from individual neurons to larger networks [112]. Several studies have shown that MER recordings in human PD patients reveal increased power in the Beta band in the STN region that provides the greatest therapeutic benefits for PD patients undergoing DBS. Therefore,frequency information could be valuable to precisely identify the electrode implantation site [113, 114]. In this study the following frequency bands were analyzed: Delta (1-4 Hz), Theta (4-8 Hz), Alpha (8-12 Hz), Beta (12-30 Hz) [115]. The MUA signal was analyzed using steps aimed at extracting and quantifying spectral features. Starting from the denoised signal (as explained in the previous section), which is filtered in the 300-5000 Hz bandwidth, the signal was rectified. From the rectified signal the envelope was obtained using a 4th

order low-pass Butterworth filter, with a cut-off frequency of 100 Hz [116, 117]. A schematization of this process to compute the MUA envelope is shown in Figure 5.14.

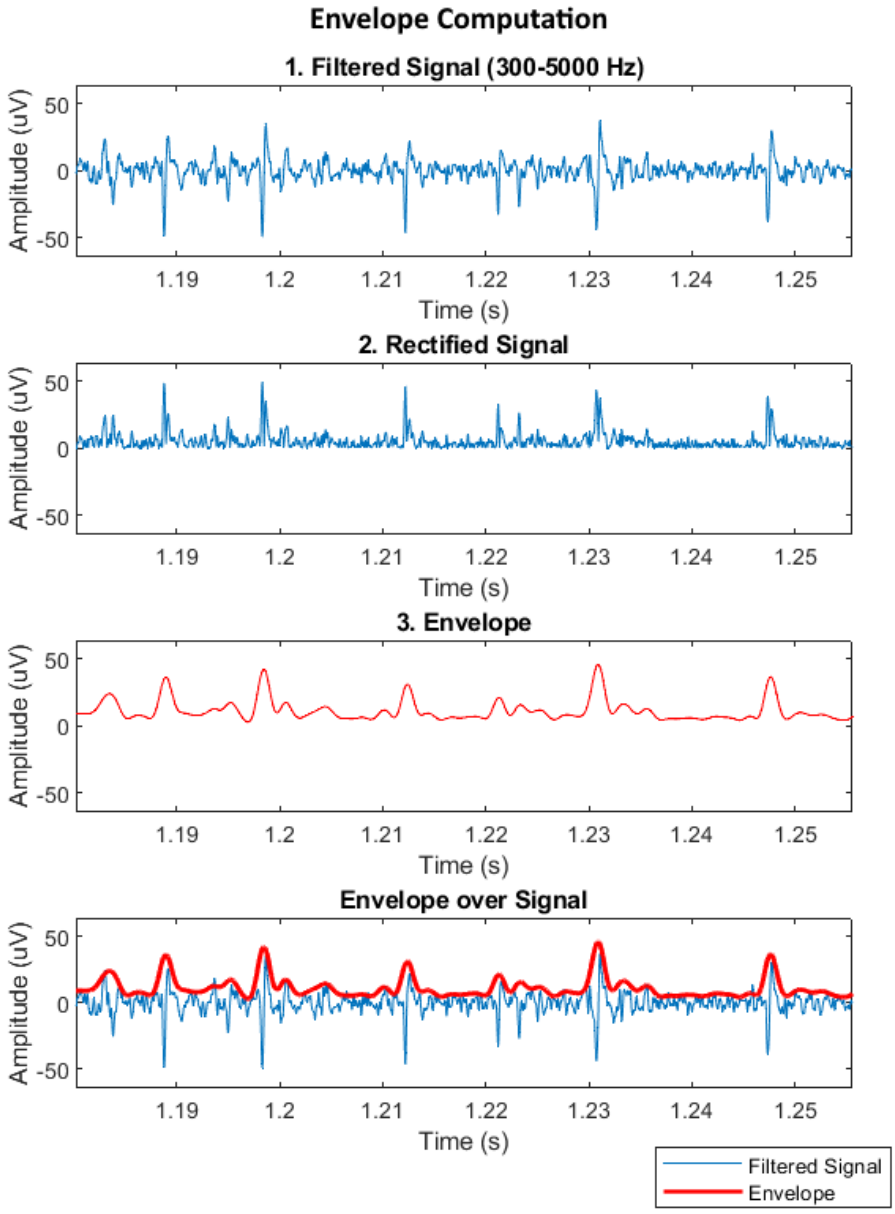

Figure 5.14: Steps used to obtain the envelope. (1) Original filtered signal. (2) Signal after rectification. (3) Envelope of the signal, obtained usgin a low-pass filter. (4) Envelope (r) overimposed to the original 300-5000 Hz signal (blue).

Once the envelope was obtained, the Power Spectral Density (PSD) was computed using Welch's method and a Hanning window of 1 s [118], with an overlap of 50%. The PSD was represented using a number of points double the length of the window, resulting in an apparent spectral resolution of 0.5 Hz. The PSD was normalized over the sum of the PSD all over frequency values.

The frequency band of interest were: Delta (0.4-4 Hz), Theta (4-8 Hz), Alpha (8-12 Hz), Beta (12-30 Hz), and Gamma (30-100 Hz)). For each band these features were computed: peak power, frequency of the peak power, minimum power and mean power.

Additonally, significant oscillations in a frequency band were identified, using a binary feature. This was done calculating the median within the 0-100 Hz frequency band, which represent the baseline signal level. The InterQuantile Range (IQR) of this baseline was obtained,and if a peak exceeding the baseline + 3*IQR was present, the oscillation in that band was considered significant, indicated by a 1. If no significant oscillation was present in the frequency band, 0 was assigned to the feature for that band.

Global Temporal Features

Finally, additional features were computed based on temporal dynamics of the whole signal, which are state of the art features used for STN localization in PD patients using MER [119, 120]. For a given MER, considered as a data vector containing N samples:

$$x = [x_1, x_2, \ldots, x_N]$$

the following features were calculated:

- **Total Spike**: The total number of spikes that exceed the detection threshold, without additional processing for neuron separation.
- **Curve Length**: The Curve Length measures the overall length of the signal curve by summing the distances between consecutive data points in the vector. The curve length for a data vector is given by:

$$\text{Curve Length} = \sum_{i=1}^{N-1} |x_{i+1} - x_i| \tag{5.37}$$

- **Root Mean Square Amplitude (RMS)**: The Root Mean Square Amplitude (RMS) is the square root of the mean of the squared signal values, computed as:

$$\text{RMS} = \sqrt{\frac{1}{N} \sum_{i=1}^{N} x_i^2} \tag{5.38}$$

- **Average Nonlinear Energy**: The Average Nonlinear Energy measures the nonlinear variation of the signal, considering the difference between current and neighboring values:

$$\text{Average Nonlinear Energy} = \frac{1}{N-2}\sum_{i=2}^{N-1} x_i^2 - x_{i-1} \cdot x_{i+1} \tag{5.39}$$

- **Zero Crossings**: Represents the number of times the signal crosses zero. This metric helps evaluate the frequency and regularity of signal oscillations:

$$\text{Zero Crossing} = \frac{1}{2}\sum_{i=1}^{N-1} |\text{sgn}(x_{i+1}) - \text{sgn}(x_i)| \tag{5.40}$$

- **Threshold**: Represents the average deviation of data points from the overall mean, indicating how much the values deviate from the mean:

$$\text{Threshold} = 3\sqrt{\frac{1}{N-1}\sum_{i=1}^{N}(x_i - \bar{x})^2} \tag{5.41}$$

These features were normalized according to signal duration in seconds.

In Table 5.6 are summarized all the features computed for MER and neurons analysis.

5.3.5 Statistical Analysis

In the following subsection, the term 'target' will be used for referring to the trajectory and implantation depth as chosen by the surgeon during the surgery. To characterize the neurons of the GPi, the SUA feature values of each neuron were analyzed, including also the presence of significant oscillations for the MER track in which the neuron was found. For the analysis of MER traces at different depths, MUA features, Global features and the mean of the neuron features present in each trace were considered. After computing the features, they were analyzed using MATLAB to investigate significant differences based on trajectory, target/non-target depth and outcome.

Since many recordings did not exhibit spikes and, therefore, did not show detectable neuronal activity, the stability features, firing rate, and burst count were set to zero for these recordings, while the other features were marked as missing values using NaNs. If a neuron was detectable but did not exhibit bursts, the burst count and the number of samples in bursts were set to zero, while the remaining

Macro Category	Category	Feature
Spike-dependent Features	**Stability Features**	SNR
		Num. Spikes
		Percentage of Close Spikes
	SUA Features	Firing Rate (λ)
		Regularity
		Coefficient of Variation (CV)
		Local Variation (LV)
		ISI Mean
		ISI Std
		ISI Skewness
		Pause Index
		Pause Ratio
		Burst Index
	For 'Burst' Neurons	Burst Spike Proportion
		Burst Avg. Spikes
		Inter-Burst Interval
		Intra-Burst Frequency
		Intra-Burst Interval
Spike-independent Features	**Spectral MUA Features**	(Delta, Theta, Alpha, Beta, Gamma)
		Mean Power
		Min Power
		Max Power
		Peak Frequency
		Significance
	Temporal Features	Curve Length
		RMS
		Average Nonlinear Energy
		Zero Crossings
		Threshold
		Total Spikes

Table 5.6: Macro categories, categories, and features, in three columns.

burst-related features were assigned NaN values. This approach was chosen to avoid contamination of the averages with non-representative data, which would have occurred if a value of zero had been assigned instead. For the statistical analysis and when computing averages of neurons within recordings, NaN values were ignored, and only valid values were considered.

Initially, features of MER from the trajectory chosen by the surgeon were compared with the features of the non-selected ones. Subsequently, the features were studied based on the depth from the target for MER recordings from the chosen trajectories of patients with a positive outcome. Finally, the neurons in the target zone and its surrounding region [-4,0] mm were characterized by comparing patients with a positive outcome to the patient with a negative outcome.

To compare the trajectory chosen by the surgeon with the others, the cumulative total number of spikes in the trajectory was initially used as a reference measure. The objective was to verify the hypothesis that the selected trajectory presented a distinctive trend compared to the others in terms of neuronal activation [121]. All selected trajectories were grouped and compared with the non-selected ones in patients with a positive outcome to determine if the surgeon's choice was supported by a statistically significant difference in terms of cumulative numer of spikes and other MER features.

After identifying the significant features for the trajectory selected by the surgeon in patients with a positive outcome, the value of these features along the trajectory was calculated for each trajectory and for each side of patient 1 with a negative outcome. The aim was to compare the surgeon's chosen trajectory with one that demonstrated the features previously identified as significant.

Patients who had a successful outcome were then selected, and the signals recorded at various depths along the surgeon's selected trajectory were examined, with the hypothesis that the target had been accurately identified for these patients. A comparison was made between the recordings obtained at a distance from the surgically identified target of 0 mm and those at other depths, to identify depth-dependent significant features.

Next, the presence of significant features was analyzed by comparing the GPi neurons of the patient with a negative outcome with those of the patients with a positive outcome. This was done considering the region between –4 mm and 0 mm from the target [122]. This decision was motivated by the fact that the main target of the DBS intervention in the GPi is the sensorimotor region of the GPi, often considered located along its postero-ventral border [123, 124]. Therefore, for a correct characterization of the GPi, it is necessary to also include depths superior to the target identified intraoperatively. Features froms stable individual neurons within the identified region were selected and examined in patients with positive and negative outcomes.

The features were compared between groups after assessing normality using

the Lilliefors test [125]. If both features were normally distributed, the Student's t-test was used [126]; otherwise, the Wilcoxon rank-sum test was applied [127]. For categorical features (firing pattern and presence of significant features in a certain spectral band), the Chi-square test [128] was employed. The results are expressed as mean and standard error of the mean.

Before conducting the statistical analysis, a preliminary check was performed to ensure the reliability of the data. Specifically, it was verified that both analysed groups contained sufficient valid data points of the features, with each group having more than three non-missing values. Only when both groups met these criteria was the data considered suitable for further analysis.

The significant differences were further evaluated based on the obtained p-value, with the assignment of one, two, or three asterisks depending on the level of significance: a p-value lower than 0.001 was associated with three asterisks ***, one lower than 0.01 but greater than 0.001 with two asterisks **, and one lower than 0.05 but greater than 0.01 with a single asterisk *. In the absence of statistical significance, the result was labeled as "ns" (not significant).

Chapter 6

Results

Of 486 available MERs, 3 of them were removed as they were corrupted from noise, so 483 MER were used for the following analysis. From these MER, a total of 479 stable neurons were identified.

6.1 Analysis of Chosen Implantation Trajectory

The activity of the trajectories was initially evaluated in terms of the cumulative total number of spikes along each trajectory, plotting the number of spikes for each patient and side, as seen in Figure 6.1. The chosen trajectory coincides with the one that shows the highest activity in terms of the number of spikes in 70% of cases considering all patients, and in 75% of cases considering only patients with a positive outcome. Specifically, the chosen trajectory coincides with the one with the highest activity in two out of five patients for the left hemisphere and in five out of five patients for the right hemisphere.

Numerical significant features were identified in the differences between the set of selected trajectories and those not selected in patients with a positive outcome. A higher total number of spikes, lower delta peak frequency, lower alpha minimum power, higher alpha and beta band peak frequency were found in the MER traces of chosen trajectories. These results are presented in Figure 6.2 through box plots. Table 6.1 reports the significant p-values obtained from statistical tests, along with the type of test applied.

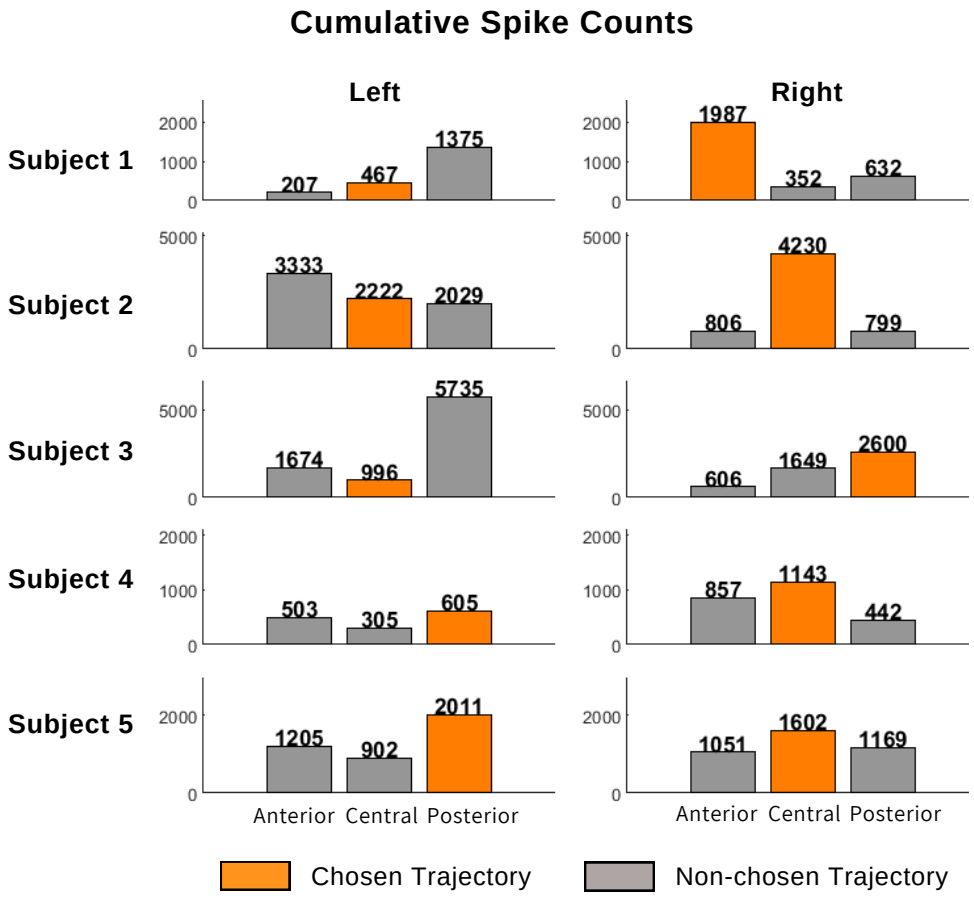

Figure 6.1: Cumulative total number of spikes along every chosen (orange) and non-chosen (grey) trajectory.

Feature	p-value	Chosen Traj.	Non-chosen Traj.	Test
Total Spike	0.0311	131.70±20.13	98.57±9.55	w
Delta Peak Frequency (Hz)	0.0484	1.51±0.08	1.75±0.07	w
Alpha Min Power	0.0404	0.0038±0.0002	0.0043±0.0002	w
Alpha Peak Frequency (Hz)	0.0022	9.76±0.13	9.30±0.08	w
Beta Peak Frequency	0.0126	20.96±0.62	19.19±0.40	w

Table 6.1: Statistical results for significant numerical features differentiating chosen and non-chosen trajectories, including p-values, means with standard errors, and the statistical test used (w = Wilcoxon Rank-Sum).

No categorical significant features were found for this comparison.

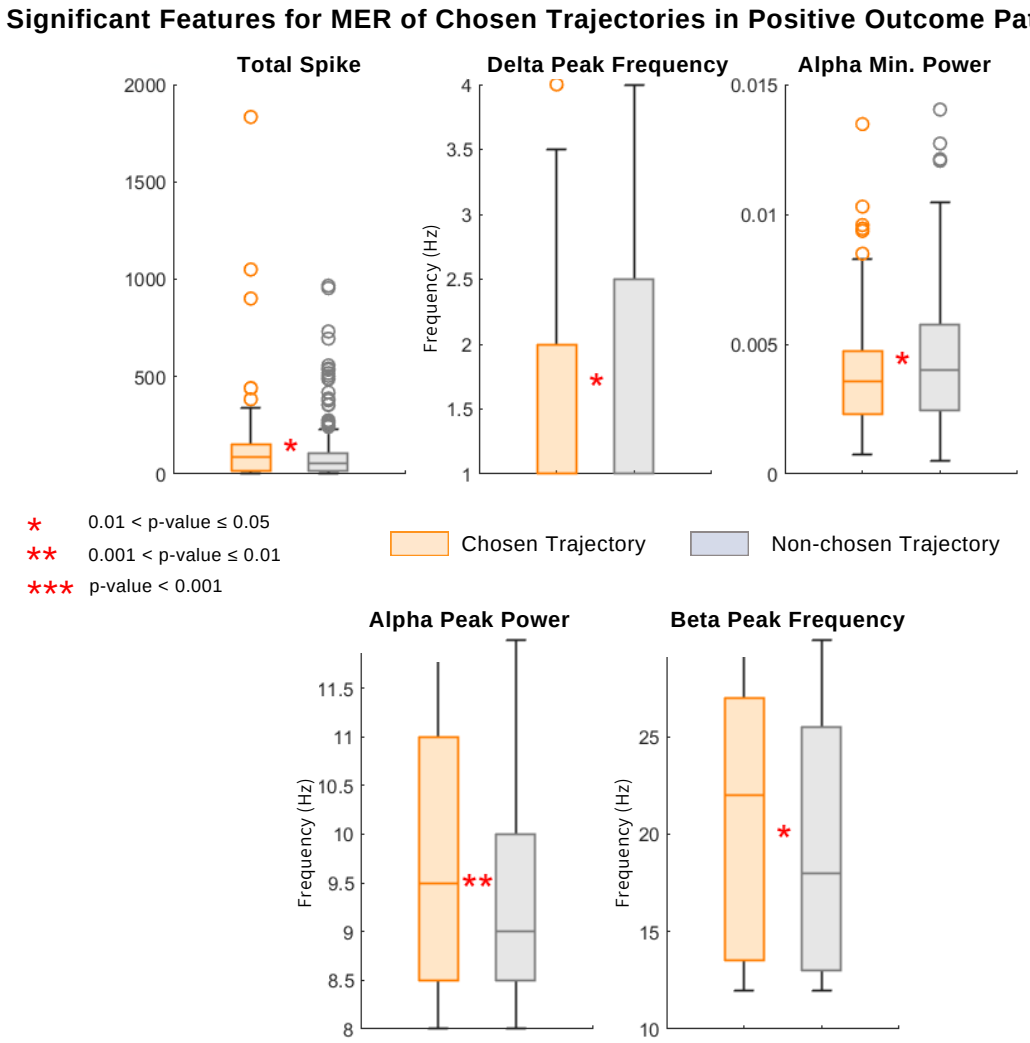

Figure 6.2: Significant features identified in the statistical analysis of numerical features for the comparison between chosen and non-chosen trajectories in positive outcome patients.

After identifying the significant features for trajectory selection in patients with a positive outcome, the value of these features was calculated for each trajectory of patient 1 with a negative outcome, as shown in Figure 6.3. For each side, we searched for the trajectory presenting the expected behaviour (higher total number of spikes, lower delta peak frequency, lower alpha minimum power, higher alpha and beta band peak frequency), based on positive outcome patient analysis.

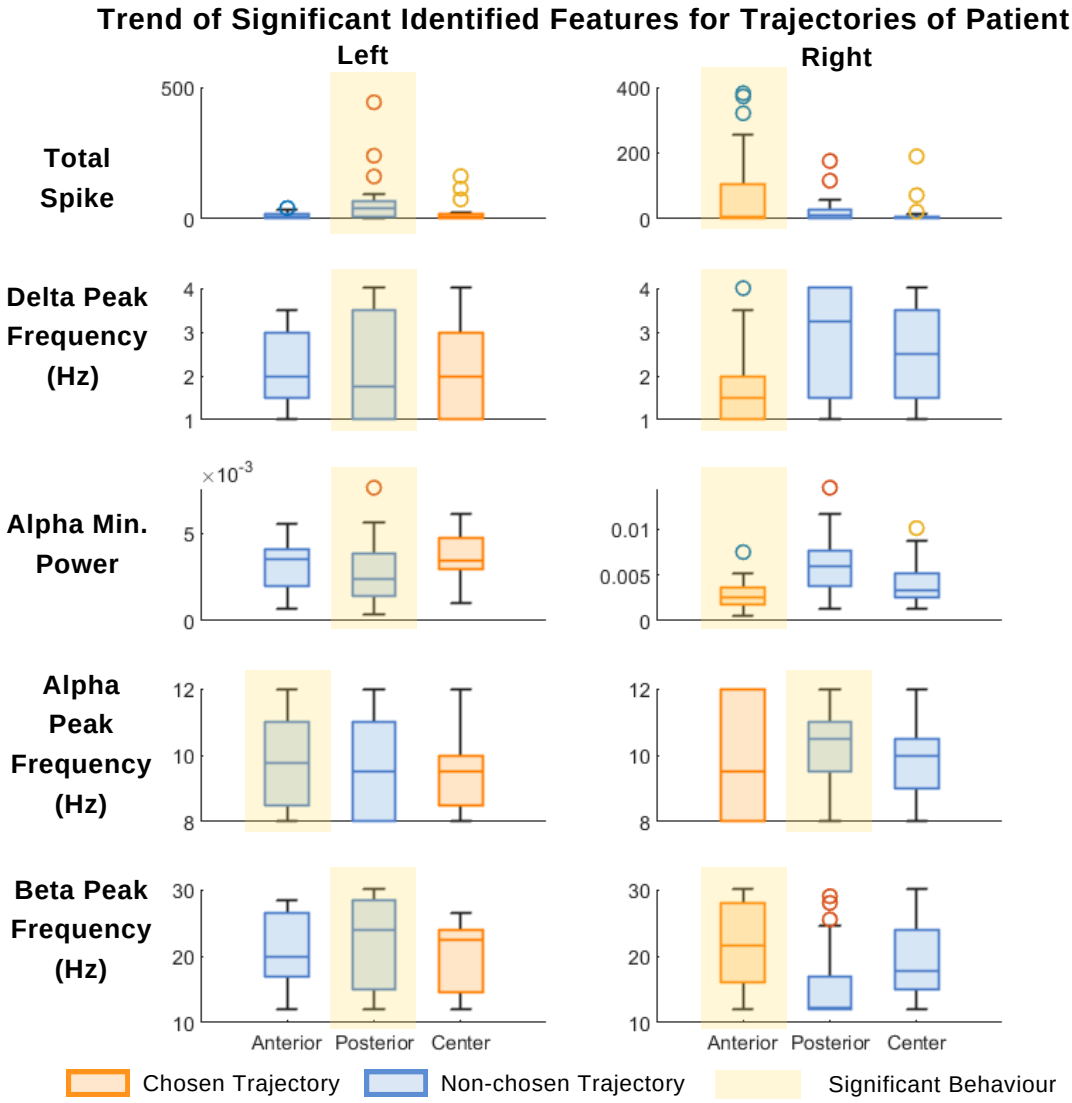

Figure 6.3: Boxplot of the feature values of patient 1 (with negative outcome) for each feature identified as significant in the previous comparison between chosen and non-chosen trajectories in positive patients. In yellow are highlighted the trajectories presenting the significant behaviour for each side. Chosen trajectories are further filled with an orange color, while non-chosen trajectories are shown in blue.

The same information is reported using one heatmap for each hemisphere containing the median value of each feature for each trajectory in Figure 6.4.

Trend of Significant Identified Features for Patient 1

Left Side

	Total Spike	Delta Peak Frequency (Hz)	Alpha Min. Power	Alpha Peak Power	Beta Peak Frequency (Hz)
Anterior	6.00 ± 3.04	2.00 ± 0.20	0.0035 ± 0.0033	**9.75 ± 0.0.34**	20.00 ± 1.24
Posterior	**42.50 ± 25.92**	**1.75 ± 0.29**	**0.0024 ± 0.0041**	9.50 ± 0.36	**24.00 2 ± 1.65**
Center	10.00 ± 10.62	2.00 ± 0.22	0.0034 ± 0.0042	9.50 ± 0.32	22.50 2 ± 1.28

Right Side

	Total Spike	Delta Peak Frequency (Hz)	Alpha Min. Power	Alpha Peak Power	Beta Peak Frequency (Hz)
Anterior	**9.00 ± 23.055**	**1.50 ± 0.18**	**0.0026 ± 0.0031**	9.50 ± 0.35	**21.50 ± 1.22**
Posterior	9.00 ± 7.91	3.25 ± 0.24	0.0059 ± 0.0062	**10.50 ± 0.2**	12.25 ± 1.08
Center	2.00 ± 7.59	2.50 ± 0.22	0.0033 ± 0.0043	10.00 ± 0.24	17.75 ± 1.13

Significance of Behaviour

Figure 6.4: Heatmap showing the significance of the behaviour for each trajectory and each feature of the left hemisphere of patient 1. The intensity of the yellow color shows the significance of the behaviour. In red is underlined the trajectory chosen by the surgeon for the final electrode implant for the left hemisphere, which shows no significant behaviour. In green are underlined the trajectories showing the most number of features with highest significant behaviours.

Finally, Table 6.2 and Table 6.3 show all the p-values obtained for the statistical analysis between the chosen and non-chosen trajectory groups in the study of positive outcome patients, respectively for numerical and categorical features.

Feature	p-value	Chosen Traj.	Non-chosen Traj.	Test
SNR	0.3097	1.50±0.14	1.36±0.09	w
Close Spikes	0.1843	0.42±0.08	0.43±0.07	w
Firing Rate	0.6579	14.49±4.37	12.55±4.41	w
Regularity	0.1279	0.044±0.046	0.16±0.033	t
CV	0.0598	1.34±0.064	1.14±0.027	w
ISI Mean	0.3847	200.60±14.32	233.24±12.70	w
ISI Std	0.9270	259.14±22.75	265.72±16.86	w
ISI Skewness	0.1307	2.03±0.047	1.92±0.030	w
LV	0.8781	0.89±0.035	0.88±0.022	w
Num Bursts	0.4239	0.093±0.031	0.082±0.026	w
Burst Avg Spikes	0.4120	1.35±0.41	0.55±0.11	w
Pause Index	0.7627	3.12±0.30	3.37±0.25	w
Pause Ratio	0.5009	86.08±15.00	80.21±15.86	w
Interbi	0.9220	143.25±130.64	567.19±165.58	w
Intrabf	0.4439	11.08±2.80	8.54±2.07	w
Intrabi	0.4628	17.23±6.04	9.79±2.67	w
Curve Length	0.4067	37405.68±686.09	37891.85±444.68	w
RMS Amplitude	0.9942	0.69±0.046	0.70±0.039	w
Avg Nonlinear Energy	0.6744	4800.74±4630.11	4710.81±4440.10	w
Zero Crossings	0.4713	4010.48±39.27	3971.61±27.58	w
Threshold feature	0.5903	75629.13±2231.58	76274.99±1360.85	w
Total Spike	0.0311	131.70±20.13	98.57±9.55	w
Delta Mean Power	0.1032	0.0135±0.0011	0.0146±0.0007	w
Delta Min Power	0.0716	0.0076±0.0007	0.0086±0.0005	w
Delta Peak Power	0.3517	0.0257±0.0025	0.0261±0.0016	w
Delta Peak Frequency	0.0484	1.51±0.0835	1.75±0.0696	w
Theta Mean Power	0.1452	0.0101±0.0006	0.0108±0.0004	w
Theta Min Power	0.0614	0.0050±0.0004	0.0057±0.0003	w
Theta Peak Power	0.3392	0.0247±0.0023	0.0238±0.0014	w
Theta Peak Frequency	0.6148	5.91±0.1490	5.80±0.1071	w
Alpha Mean Power	0.3967	0.0140±0.0014	0.0134±0.0009	w
Alpha Min Power	0.0404	0.0038±0.0002	0.0043±0.0002	w
Alpha Peak Power	0.4929	0.0310±0.0041	0.0282±0.0025	w
Alpha Peak Frequency	0.0022	9.76±0.1300	9.30±0.0837	w
Beta Mean Power	0.8869	0.0044±0.0001	0.0044±0.0001	w
Beta Min Power	0.5614	0.0022±0.0001	0.0022±0.0001	w
Beta Peak Power	0.8334	0.0081±0.0003	0.0083±0.0002	w
Beta Peak Frequency	0.0126	20.96±0.6153	19.19±0.3982	w
Gamma Mean Power	0.7594	0.0034±0.0001	0.0034±0.0001	w
Gamma Min Power	0.8966	0.0007±0.0000	0.0007±0.0000	w
Gamma Peak Power	0.1874	0.0130±0.0008	0.0122±0.0006	w
Gamma Peak Frequency	0.4165	58.21±2.26	59.78±1.54	w

Table 6.2: Statistical results for all numerical features differentiating chosen and non-chosen trajectories, including p-values, means with standard errors, and the statistical test used (w = Wilcoxon Rank-Sum, t = Student's t-test).

Feature	p-value	Chi2 Stat	Chosen Traj. (0 / 1)	Non-chosen Traj. (0 / 1)
Delta Significance	0.8694	0.0270	30.77% / 69.23%	29.91% / 70.09%
Theta Significance	0.1071	2.5965	47.01% / 52.99%	38.03% / 61.97%
Alpha Significance	0.3636	0.8254	57.27% / 42.73%	52.14% / 47.86%
Beta Significance	0.5098	0.4344	88.03% / 11.97%	85.47% / 14.53%
Gamma Significance	0.3696	0.8050	65.81% / 34.19%	70.51% / 29.49%

Table 6.3: Statistical significance for MUA delta, theta, alpha, beta, and gamma with p-values, Chi-squared values, and group percentages for chosen and not chosen trajectories for postive outcome patients.

6.2 Analysis of Chosen Target Depth

In the comparison between the target area and other depths, one significant feature was identified: lower Peak Power in theta band. This result is visible in the box plot shown in Figure 6.5. Total Spike Count, even if not significant, presented a low p-value of 0.0827, so it was also plotted. Additionally, the p-value obtained for significant features for this comparison are reported in Table 6.4.

Feature	p-value	Chosen Depth	Non-chosen Depth	Test
Total Spike	0.0827	69.29±46.65	135.67±21.19	w
Theta PeakFrequency	0.0455	4.79±0.58	5.99±0.15	w

Table 6.4: Statistical results for significant features comparing chosen and non-chosen implant depth of positive outcome patients, including p-values, means with standard errors, and the statistical test used (w = Wilcoxon Rank-Sum test).

Additionally, the value of these identified significant or almost significant features was plotted along the distance from identified surgical target for each trajectory of each positive outcome patient using a spline interpolation of data points and normalized over the range. The trend was averaged over subjects, and is shown in Figure 6.6.

All the p-values obtained from statistical analysis for depth are reported in Table 6.5 for numerical features and 6.6 for categorical features.

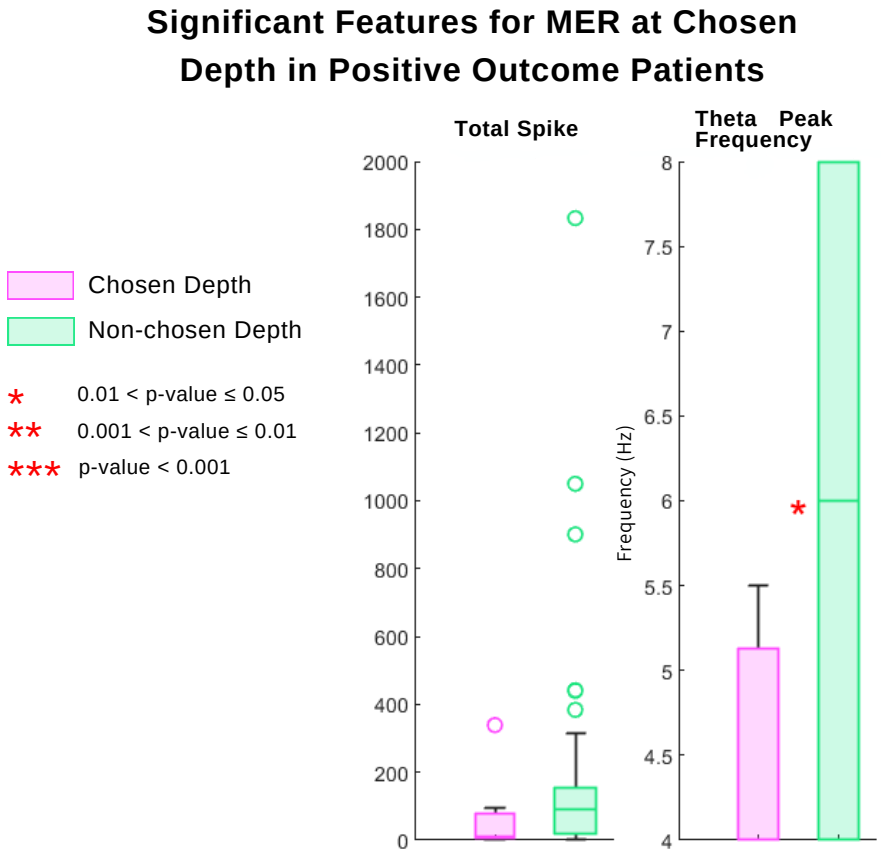

Figure 6.5: Significant and almost significant features identified in the statistical analysis of numerical features for the comparison between chosen (pink) and non-chosen (green) depths in positive outcome patients.

Feature	p-value	Chi2 Stat	Chosen Depth (0 / 1)	Chosen Depth (0 / 1)
Delta Significance	0.4748	0.5107	42.86% / 57.14%	30.00% / 70.00%
Theta Significance	0.5795	0.3070	57.14% / 42.86%	46.36% / 53.64%
Alpha Significance	0.9946	0.0001	57.14% / 42.86%	57.27% / 42.73%
Beta Significance	0.8454	0.0380	85.71% / 14.29%	88.18% / 11.82%
Gamma Significance	0.6180	0.2487	57.14% / 42.86%	66.36% / 33.64%

Table 6.6: Statistical significance for Delta, Theta, Alpha, Beta, and Gamma features with p-values, Chi-squared values, and group percentages for Chosen and Non-chosen implantation depth.

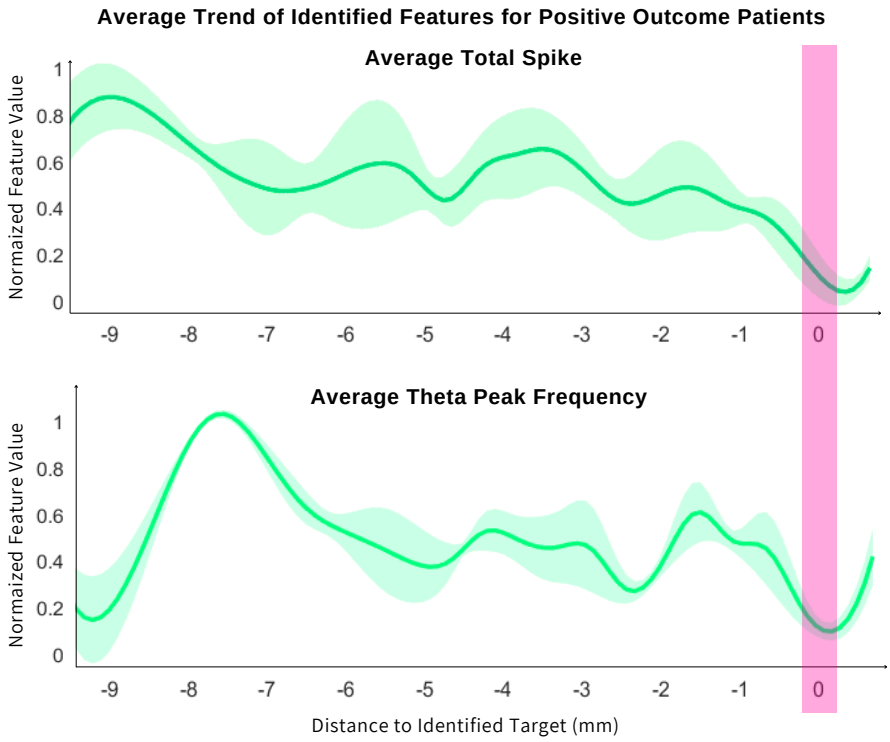

Figure 6.6: Plot showing the average trend of Theta Peak Frequency and Total Spike over the distance from identified target for positive outcome patients' trajectories. In pink is highlighted the point where distance to target is equal to 0 mm.

6.3 Comparison of GPi of Positive and Negative Outcome Patients

Finally, from the recordings taken between -4 mm and 0 mm from the target, 81 GPi neurons were identified in the four patients with a positive outcome and 21 GPi neurons in the patient with a negative outcome. A statistical comparison was performed between the two groups, and significant features were identified. To analyze the firing pattern, a tonic pattern was associated with 1, a bursting pattern with 2 and irregular patterns with 3. Figure 6.7 presents the results of the analysis through box plots for significant numerical features, while 6.7 contains the p-values obtained from the statistical tests.

Feature	p-value	Chosen Depth	Non-chosen Depth	Test Type
Spike Count	0.2162	55.29±47.77	44.40±6.61	w
SNR	0.1284	0.63±0.42	1.56±0.14	w
Firing Rate	0.2297	58.17±56.69	11.71±3.03	w
Curve Length	0.4655	36332.84±2942.38	37473.95±708.37	w
RMS Amplitude	0.2576	0.63±0.22	0.69±0.05	w
Avg Nonlinear Energy	0.3315	50.29±24.89	5103.04±4924.68	w
Zero Crossings	0.5427	4105.78±122.48	4004.41±41.08	t
Threshold Feature	0.5236	70522.24±6093.19	75954.11±2343.24	w
Total Spike	0.0827	69.29±46.65	135.67±21.19	w
Delta Mean Power	0.4941	0.0121±0.0040	0.0136±0.0012	w
Delta Min Power	0.8677	0.0091±0.0035	0.0075±0.0007	w
Delta Peak Power	0.4516	0.0172±0.0047	0.0263±0.0027	w
Delta Peak Frequency	0.9001	1.71±0.47	1.50±0.08	w
Theta Mean Power	0.8406	0.0096±0.0023	0.0101±0.0006	w
Theta Min Power	0.4447	0.0056±0.0016	0.0050±0.0004	w
Theta Peak Power	0.5236	0.0202±0.0085	0.0250±0.0023	w
Theta Peak Frequency	0.0455	4.79±0.58	5.99±0.15	w
Alpha Mean Power	0.4178	0.0111±0.0051	0.0142±0.0015	w
Alpha Min Power	0.8767	0.0039±0.0010	0.0038±0.0002	w
Alpha Peak Power	0.5694	0.0232±0.0146	0.0315±0.0043	w
Alpha Peak Frequency	0.9169	9.93±0.70	9.75±0.13	w
Beta Mean Power	0.9222	0.0045±0.0005	0.0044±0.0002	w
Beta Min Power	0.3490	0.0025±0.0004	0.0022±0.0001	w
Beta Peak Power	0.9799	0.0081±0.0008	0.0081±0.0003	t
Beta Peak Frequency	0.6204	20.29±2.64	21.00±0.64	w
Gamma Mean Power	0.2124	0.0038±0.0004	0.0034±0.0001	w
Gamma Min Power	0.8406	0.0007±0.0001	0.0007±0.0000	w
Gamma Peak Power	0.4941	0.0130±0.0024	0.0129±0.0009	w
Gamma Peak Frequency	0.9081	55.79±9.03	58.37±2.35	w

Table 6.5: All statistical results for numerical features comparing chosen and non-chosen implant depth for positive outcome patients, including p-values, means with standard errors, and the statistical test used (w = Wilcoxon Rank-Sum test, t = Student's t-test).

Feature	p-value	Positive	Negative	Test
SNR	0.0016	2.53 ± 0.13	3.63 ± 0.36	w
Firing Rate	0.0001	19.90 ± 5.29	109.43 ± 73.70	w
ISI Mean	0.00003	177.54 ± 17.47	63.20 ± 14.13	w
ISI Std	0.0003	231.32 ± 23.83	82.65 ± 11.53	w
LV	0.0013	0.85 ± 0.044	0.55 ± 0.07	w
Pause Index	0.00002	2.82 ± 0.49	1.20 ± 0.76	w
Pause Ratio	0.00003	61.95 ± 14.77	13.12 ± 7.51	w

Table 6.7: Statistical values for numerical significant features with their p-values, means, standard error for the two groups (positive and negative outcome), and the test used (w = Wilcoxon Rank-Sum test).

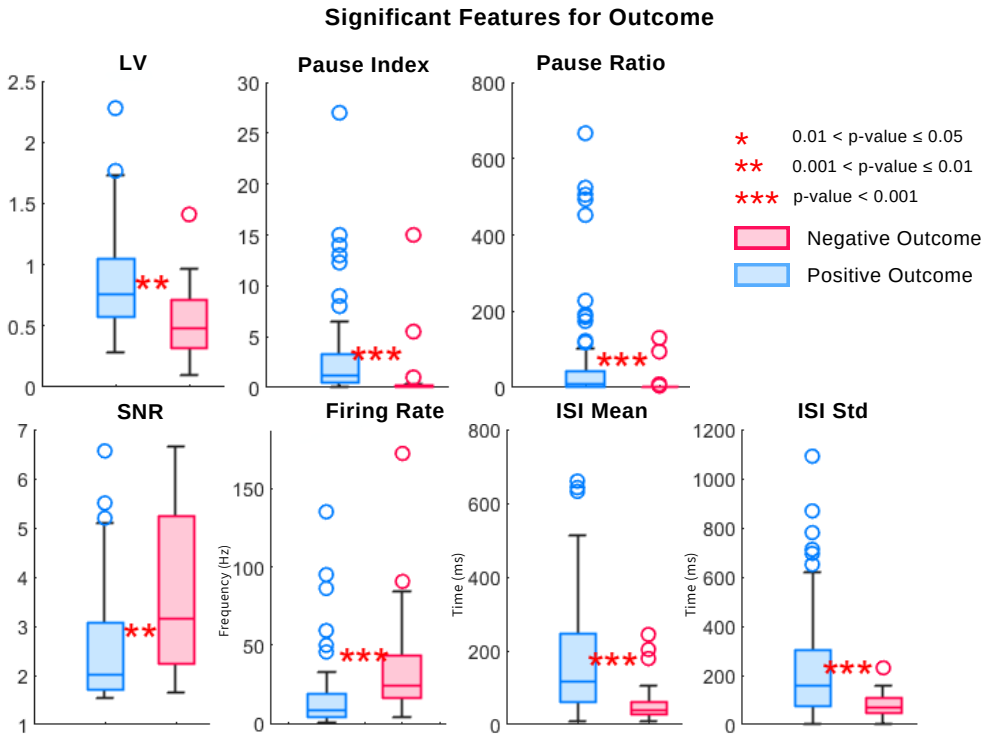

Figure 6.7: Significant features identified in the statistical analysis of numerical features for the comparison between positive (blue) and negative (pink) outcome patients neurons.

Regarding categorical features, two significant features were identified, as shown in Figure 6.8 and Table 6.8.

Feature	p-value	Chi2 Stat	Positive (0 / 1)	Negative (0 / 1)
Alpha Significance	0.00005	16.6136	43.68% / 54.31%	95.24% / 4.76%
Theta Significance	0.0071	7.2557	43.21% / 56.79%	76.19% / 23.81%

Table 6.8: Statistical significance for MUA alpha, and theta with p-values, Chi-squared values, and group percentages for positive and negative outcome neurons.

Finally, the percentage of Bursting, Irregular and Tonic neurons and the number of burst of the neurons were plotted using pie charts, as shown in Figure 6.9. Differences were not significant, as reported in Table 6.9 and 6.10.

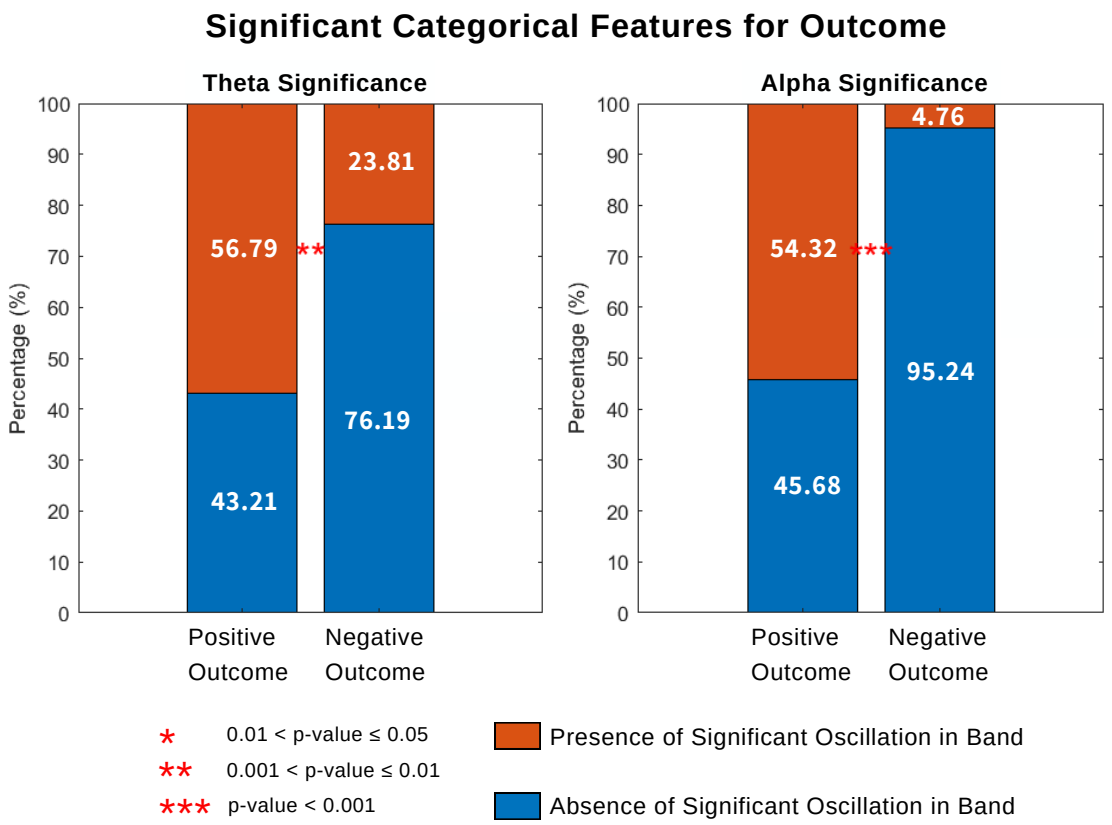

Figure 6.8: Significant categorical features identified in the statistical analysis of categorical features for the positive outcome patients and the negative outcome patient. In orange is the percentage of significant (1) oscillations in the frequency band, in blue the absence (0).

Feature	**p-value**	**Chi2 Stat**	**Positive** (Tonic, Irr., Burst.)	**Negative** (Tonic, Irr., Burst.)
Firing Pattern	0.2071	3.15	30.86%, 29.63%, 39.51%	38.10%, 42.86%, 19.05%

Table 6.9: Statistical data for the Firing Pattern feature (Irr. = irregular, Burst. = Bursting, Tonic), including p-values, Chi-squared values, and group percentages for bursting, tonic and irregular neurons in positive and negative outcome neurons.

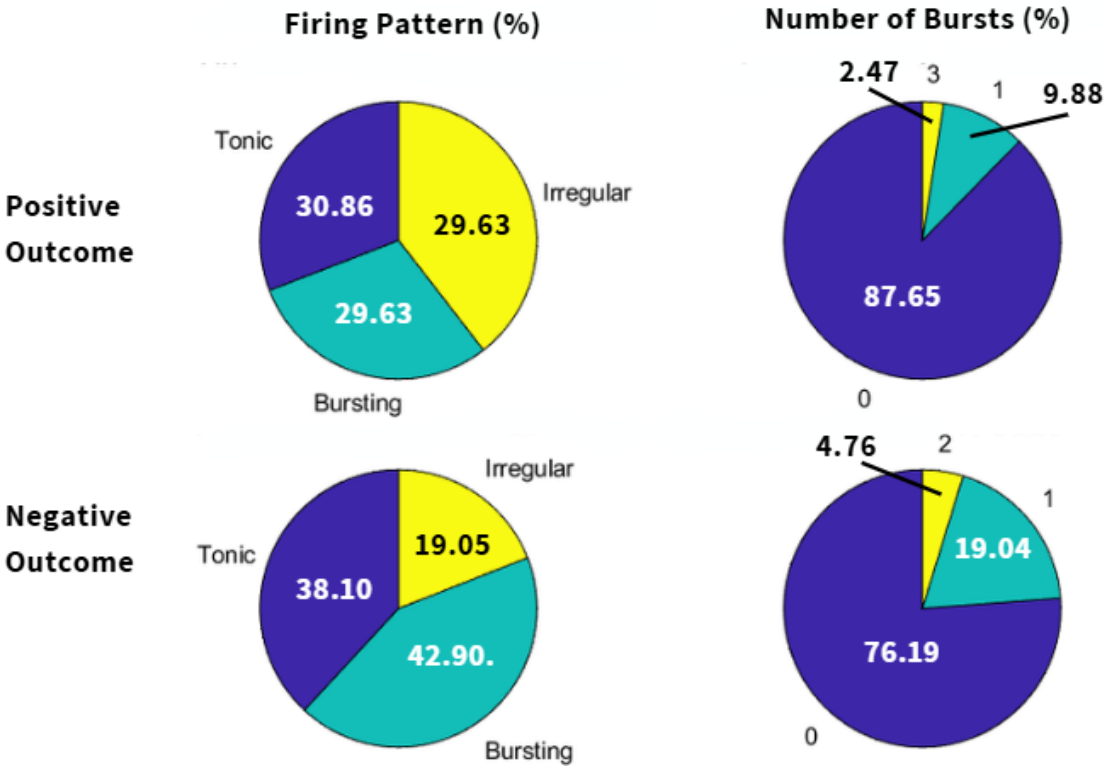

Figure 6.9: Pie Chart showing the percentages of Irregular, Tonic and Bursting neurons and the number of bursts in Positive and Negative outcome neurons.

Feature	**p-value**	**Chi2 Stat**	**Positive** (0, 1, 2, 3)	**Negative** (0, 1, 2, 3)
Num Bursts	0.1204	5.82	87.65%, 9.88%, 0%, 2.47%	76.19%, 19.05%, 4.76%, 0%

Table 6.10: Statistical data for the Number of Bursts feature, including p-values, Chi-squared values, and group percentages for 0, 1, 2, 3 bursts in positive and negative outcome neurons.

In Table 6.12 and 6.11 are reported all p-values obtained from statistic analysis between positive and outcome groups, respectively for numerical and categorical features.

Feature	p-value	Chi2 Stat	Positive (0 / 1)	Negative (0 / 1)
Delta Significance	0.2847	1.14	30.86% / 69.14%	19.05% / 80.95%
Theta Significance	0.0071	7.26	43.21% / 56.79%	76.19% / 23.81%
Alpha Significance	0.00005	16.61	45.68% / 54.32%	95.24% / 4.76%
Gamma Significance	0.1068	2.60	67.90% / 32.10%	85.71% / 14.29%

Table 6.11: Statistical data for the MUA features, including p-values, Chi-squared values, and group percentages for presence (1) or absence (0) neurons in positive and negative outcome neurons.

Feature	p-value	Chi2 Stat	Positive	Negative
Spike Count	0.4664	72.00 ± 7.66	77.00 ± 14.86	w
SNR	0.0016	2.53 ± 0.13	3.63 ± 0.36	w
Close Spikes	0.2442	0.32 ± 0.09	0.08 ± 0.05	w
Firing Rate	0.0001	19.90 ± 5.29	109.43 ± 73.70	w
Firing Pattern	0.1680	2.09 ± 0.09	1.81 ± 0.16	w
Regularity	0.9275	0.03 ± 0.06	0.28 ± 0.22	w
CV	0.0822	1.47 ± 0.12	1.71 ± 0.20	w
ISI Mean	0.0001	177.54 ± 17.47	63.20 ± 14.13	w
ISI Std	0.0003	231.32 ± 23.83	82.65 ± 11.53	w
ISI Skewness	0.9275	2.04 ± 0.06	1.92 ± 0.15	w
LV	0.0013	0.85 ± 0.04	0.55 ± 0.07	w
Num Bursts	0.1962	0.17 ± 0.06	0.29 ± 0.12	w
Burst Avg Spikes	0.2090	1.01 ± 0.34	1.43 ± 0.58	w
Pause Index	0.0002	2.82 ± 0.49	1.20 ± 0.76	w
Pause Ratio	0.0003	61.95 ± 14.77	13.12 ± 7.51	w
Interbi	0.4723	319.39 ± 192.25	1158.15 ± 911.23	w
Intrabf	0.1835	20.21 ± 6.77	38.57 ± 16.29	w
Intrabi	0.2266	7.54 ± 2.68	10.01 ± 4.43	w

Table 6.12: Statistical data for various features, including p-values, Chi-squared statistics, and feature values for positive and negative outcome group neurons, and the statistical test used (w = Wilcoxon Rank-Sum test)

6.4 Computational Time

For each patient and side, the computational time required to obtain the feature table was computed and compared, as shown in Table 6.13. The elaboration time for 1 s of MER is also reported, with a mean of 2.08 s of elaboration for 1 s of MER signal.

Patient	**Hemisphere**	**Total Time (min)**	**Time for 1 s of MER (s)**
Patient 1	Left	4.76	1.76
	Right	11.42	2.92
Patient 2	Left	12.39	1.07
	Right	21.98	2.44
Patient 3	Left	11.80	1.31
	Right	18.32	3.05
Patient 4	Left	2.52	1.86
	Right	6.20	3.44
Patient 5	Left	3.20	0.96
	Right	9.02	2.00

Table 6.13: Total analysis time (in minutes) and average time per second of MER for each side of each patient.

Chapter 7

Discussion

This chapter will discuss the previous analysis and results. Firstly, it can be observed that most of the available recordings were not so corrupted as to be excluded, since only 3 out of the total were unusable for analysis.

Results obtained from the analysis of surgically chosen trajectory shows that, as suggested by the hypotheses, neuronal activity was crucial in the selection [121], which in the present study was evaluated using the cumulative number of spikes along the trajectory. Figure 6.1 shows that the chosen trajectory corresponded to the one with the highest number of spikes in 70% of cases, increasing to 75% when considering only patients with a positive outcome. Considering all five patients, the chosen trajectory coincided with the one with the greatest number of spikes in 5 out of 5 patients for the right hemisphere and in 2 out of 5 for the left hemisphere.

Regarding the significant features obtained from trajectory analysis in positive outcome patients, these include the total spike count, which was higher for the chosen trajectories (131.70 ± 20.13 vs 98.57 ± 9.55, $p < 0.05$) compared to the non-chosen ones. This indicates that to track the correct trajcetory for the identification of the globus pallidus, spikes have to be present in the trajectory. If the trajectory presents no spikes, it is improbable that the trajectory is correct. Oscillatory features also proved to be significant, particularly lower Delta Peak Frequency for chosen trajectories ($p<0.05$), lower Alpha Min Power ($p<0.05$), higher Alpha Peak Frequency ($p<0.01$), and higher Beta Peak Frequency ($p<0.05$).

Beta frequency has been studied in literature regarding dystonia, but has not been rielably correlated with severity of distonic symptoms [129]. In a study from Fasano et a. (2022) [130], delta LFP peak power correlated with the severity of dystonia. Alpha frequency range was found in most distonic patients in a study from Moll et al. (2014) [131], which analyzed 13 distonic adult distonic patients.

Yokochi et al. (2018) in his study divided distonic patient in phasic and tonic subgroups, showing that alpha frequency band content was present in patients in the phasic group and delta frequency band content in patients from the tonic group [132].

After determining significant features for trajectory identification in positive outcome patients, we examined the trajectories of Patient 1, who had a negative outcome. The aim was to determine if there was a trajectory with behavior or trend similar to the one identified in the positive outcome patient group. The analysis showed that for the right side, the trajectory chosen by the surgeon (anterior) for electrode implantation exhibited 4/5 of the expected features behaviors, while for the left side, the chosen trajectory (central) did not show the exptected trend. In contrast, the posterior trajectory of left side displayed 4/5 correct trends, as shown in Figure 6.3. This suggests that the best trajectory for implantation in Patient 1's left side may have been the posterior one, rather than the central one.

Regarding the study of the final electrode positioning, Theta Peak Frequency tends to be higher at different depths compared to the depth used for electrode implantation. This demonstrates that the Theta Peak Frequency varies significantly with depth, with the lowest peak corresponding to the implantation target, suggesting its potential utility in studying depth. The results highlight the importance of the Theta band for the identification of the GPi, as also suggested by the literature [133, 131]. The lower peak at the implantation depth might be due to the fact that the target is located at the postero-ventral border of the globus pallidus, where fewer spikes are present [83, 121]. This suggests that the Theta band might show a reduced value at the target depth. Therefore, for accurate identification of the target region, it would be necessary to first identify a region with high Theta activity and then locate the depth at which this activity decreases, as this would indicate the border of the GPi, which is also characterized by a lower number of spikes.

Starting with the assumption that the primary target of GPi-DBS is the sensorimotor region of the GPi located along the postero-ventral border, the analysis interval for GPi neurons was defined as between 0 mm and -4 mm relative to the chosen surgical depth [122, 123, 124], these neurons were studied to search differences related to surgical outcome. Regarding the firing rate, which in this study is significantly lower in the GPi of patients with a positive outcome, a similar result was also reported by Sedov et al. (2021) [134]. In this study, it was shown that there is a better response to GPi-DBS in neurons with a lower firing rate. Furthermore, the literature suggests that the GPi in dystonic patients appears to be characterized by bursting-type activity [135, 134]. In the present study, this characteristic was not found to be statistically significant in distinguishing patient

groups or depths. However, GPi neurons identified in patients with a positive outcome exhibited an irregular firing pattern, observable from the LV value closer to 1, along with more frequent pauses. These aspects of irregular firing patterns and long pauses observed in the dystonic GPi are also found in several other studies, such as those by Tang et al. (2007) [136], Bour et al. (2010) [121], Vitek et al. (1999) [137], and Zhuang et al. (2004) [138]. Multiple studies have identified a significant correlation between theta/alpha frequency band power with severity of dystonia [129], which is linked to the result of the positive outcome patients neurons having higher percentage of significant oscillations in these bands.

The pie chart shows that positive outcome group neurons have about the same percentage of presence between tonic, irregular and bursting firing patterns, with a prevalence for irregular patterns. Neurons from negative outcome patient GPi showed less presence of irregular firing pattern, with the rest of the neurons having the same percentages of bursting and regular neurons. Most of the analyzed neurons did not show a burst, with more neurons in the negative patient GPi showing at least 1 burst.

Computational time analisys shows that the average elaboration time for 1 s of MER signal is about 2 s, making it possible for the surgeon to use these automatically obtained features during DBS surgery to refine electrode positioning using quantitative informations.

Chapter 8

Conclusions and Future Developments

This study performed an automatic analysis of MER signals obtained from pediatric patients affected by dystonia during GPi-DBS procedures. Statistically relevant features have been identified regarding the choice of the trajectory to follow and the final depth for inserting the definitive electrode in GPi-DBS procedures, as well as the possible outcome of the surgery itself. This suggests that the results obtained could be highly useful for surgeons when implanting the final DBS electrode. Using automatic obtained features can minimize the human error and render the procedure more repetable and quantitative. However, it should be noted that this study is based on a small number of participating patients, and it would be necessary to analyze a larger sample to obtain more meaningful results that better reflect population variability. Only one patient in the analyzed sample presented a negative outcome. This supports the effectiveness of GPi-DBS in treating dystonia but, with regard to this study, provided limited information for the analysis and characterization of MER signals for outcome. Therefore, it would be useful to conduct a similar study on a larger patients sample in order to confirm the actual significance of these features and to potentially use them in real-time in the future to support the surgeon during DBS electrode implantation.

Bibliography

[1] A. Albanese, K. Bhatia, S. B. Bressman, M. R. DeLong, and S. Fahn. «Phenomenology and classification of dystonia: a consensus update». In: *Mov. Disord.* 28.7 (June 2013), pp. 863–873. DOI: 10.1002/mds.25475 (cit. on pp. 1, 5, 6, 8).

[2] Caring Medical. *Getting Help for Cervical Dystonia (Spastic Torticollis)*. Accessed: 30-Jan-2025. 2025. URL: https://caringmedical.com/prolotherapy-news/getting-help-cervical-dystonia-spastic-torticollis/ (cit. on p. 1).

[3] Q. N. Luc and J. Querubin. «Clinical Management of Dystonia in Childhood». In: *Paediatr Drugs* 19.5 (Oct. 2017), pp. 447–461. DOI: 10.1007/s40272-017-0243-3 (cit. on p. 2).

[4] C. Gorodetsky and A. Fasano. «Approach to the Treatment of Pediatric Dystonia». In: *Dystonia* 1 (Aug. 2022), Special Issue: Inaugural Issue of Dystonia. DOI: 10.3389/dyst.2022.10287 (cit. on p. 2).

[5] M.A. Thenganatt and J. Jankovic. «Treatment of dystonia». In: *Neurotherapeutics* 11.1 (2014), pp. 139–152. DOI: 10.1007/s13311-013-0231-4 (cit. on p. 2).

[6] M. A. Wedemeyer and M. A. Liker. «Deep Brain Stimulation for Pediatric Dystonia». In: *Cerebral Palsy*. First Online: 02 October 2020. Springer, 2020, pp. 679–687. DOI: 10.1007/978-3-030-35741-6_88 (cit. on p. 2).

[7] Kenhub. *Globus Pallidus - Anatomy and Function*. Accessed: 30-Jan-2025. 2025. URL: https://www.kenhub.com/en/library/anatomy/globus-pallidus (cit. on p. 2).

[8] Boston Children's Hospital. *Deep Brain Stimulation (DBS)*. Accessed: 2025-01-30. 2025. URL: https://www.childrenshospital.org/treatments/deep-brain-stimulation (cit. on p. 3).

[9] *Electrode implantation for deep brain stimulation in Parkinson's disease*. Accessed: Jan 30, 2025. 2025. URL: https://www.researchgate.net/figure/Electrode-implantation-for-deep-brain-stimulation-in-Parkinsons-disease_fig2_371034152 (cit. on p. 3).

[10] T. M. Kinfe and J. Vesper. «The impact of multichannel microelectrode recording (MER) in deep brain stimulation of the basal ganglia». In: *Acta Neurochir. Suppl.* 117 (2013), pp. 27–33. DOI: 10.1007/978-3-7091-1482-7_5 (cit. on p. 3).

[11] P. A. Karthick, K. R. Wan, A. S. A. Qi, J. Dauwels, and N. K. Kam King. «Automated detection of subthalamic nucleus in deep brain stimulation surgery for Parkinson's disease using microelectrode recordings and wavelet packet features». In: *J. Neurosci. Methods* 343 (Sept. 2020), p. 108826. DOI: 10.1016/j.jneumeth.2020.108826 (cit. on p. 3).

[12] L. Xiao, C. Li, Y. Wang, W. Si, D. Zhang, et al. «Automatic identification of sweet spots from MERs for electrodes implantation in STN-DBS». In: *Int J Comput Assist Radiol Surg* 16.5 (May 2021), pp. 809–818. DOI: 10.1007/s11548-021-02377-2 (cit. on p. 4).

[13] H. Oppenheim. «About a rare spasm disease of childhood and young age (Dysbasia lordotica progressiva, dystonia musculorum deformans)». In: *Neurol Centralblatt* 30 (1911), pp. 1090–1107 (cit. on p. 5).

[14] P.L. Kramer, D. de Leon, L. Ozelius, et al. «Dystonia gene in Ashkenazi Jewish population is located on chromosome 9q32-34». In: *Annals of Neurology* 27.2 (1990), pp. 114–120. DOI: 10.1002/ana.410270203 (cit. on pp. 5, 6).

[15] C. Marras, A. Lang, B. P. van de Warrenburg, et al. «Nomenclature of genetic movement disorders: Recommendations of the international Parkinson and movement disorder society task force». In: *Movement Disorders* 31.4 (2016), pp. 436–457. DOI: 10.1002/mds.26527 (cit. on p. 6).

[16] A. Domingo, R. Yadav, and L. J. Ozelius. «Isolated dystonia: clinical and genetic updates». In: *J Neural Transm (Vienna)* 128.4 (2021), pp. 405–416. DOI: 10.1007/s00702-020-02268-x (cit. on p. 8).

[17] A. Weissbach, G. Saranza, and A. Domingo. «Combined dystonias: clinical and genetic updates». In: *J Neural Transm (Vienna)* 128.4 (2021), pp. 417–429. DOI: 10.1007/s00702-020-02269-w (cit. on p. 8).

[18] R. Herzog, A. Weissbach, T. Bäumer, and A. Münchau. «Complex dystonias: an update on diagnosis and care». In: *J Neural Transm (Vienna)* 128.4 (2021), pp. 431–445. DOI: 10.1007/s00702-020-02275-y (cit. on p. 8).

[19] E Mulroy, B Balint, and KP Bhatia. «Tardive syndromes». In: *Pract Neurol* 20.5 (2020), pp. 368–376. DOI: 10.1136/practneurol-2020-002566 (cit. on p. 8).

[20] K. Grütz and C. Klein. «Dystonia updates: definition, nomenclature, clinical classification, and etiology». In: *Journal of Neural Transmission* 128.4 (2021), pp. 395–404. DOI: 10.1007/s00702-021-02314-2 (cit. on pp. 8–11).

[21] K Rostasy, SJ Augood, JW Hewett, and et al. «TorsinA protein and neuropathology in early onset generalized dystonia with GAG deletion». In: *Neurobiol Dis* 12.1 (2003), pp. 11–24. DOI: 10.1016/s0969-9961(02)00010-4 (cit. on p. 8).

[22] R Paudel, J Hardy, T Revesz, JL Holton, and H Houlden. «Review: genetics and neuropathology of primary pure dystonia». In: *Neuropathol Appl Neurobiol* 38.6 (2012), pp. 520–534. DOI: 10.1111/j.1365-2990.2012.01298.x (cit. on p. 8).

[23] R Paudel, A Li, J Hardy, KP Bhatia, H Houlden, and J Holton. «DYT6 Dystonia: A Neuropathological Study». In: *Neurodegener Dis* 16.3-4 (2016), pp. 273–278. DOI: 10.1159/000440863 (cit. on p. 8).

[24] C. Klein, K. Lohmann, C. Marras, and A. Münchau. *Hereditary Dystonia Overview*. Ed. by Margaret P Adam, Jerry Feldman, Ghayda M Mirzaa, Roberta A Pagon, Stephanie E Wallace, and Anne Amemiya. Updated June 22, 2017. Seattle (WA): University of Washington, Oct. 2003 (cit. on p. 9).

[25] T. Fuchs, R. Saunders-Pullman, I. Masuho, et al. «Mutations in GNAL cause primary torsion dystonia». In: *Nature Genetics* 45.1 (2013), pp. 88–92. DOI: 10.1038/ng.2496 (cit. on p. 11).

[26] G. Charlesworth, V. Plagnol, K. M. Holmström, et al. «Mutations in ANO3 Cause Dominant Craniocervical Dystonia: Ion Channel Implicated in Pathogenesis». In: *American Journal of Human Genetics* 91.6 (2012), pp. 1041–1050. DOI: 10.1016/j.ajhg.2012.10.024 (cit. on p. 11).

[27] E. Meyer, K.J. Carss, J. Rankin, et al. «Mutations in the histone methyltransferase gene KMT2B cause complex early-onset dystonia». In: *Nature Genetics* 49.2 (2017), pp. 223–237. DOI: 10.1038/ng.3740 (cit. on p. 11).

[28] H. A. Jinnah, A. Albanese, K. P. Bhatia, et al. «Treatable Inherited Rare Movement Disorders». In: *Movement Disorders* 33.1 (2018), pp. 21–35. DOI: 10.1002/mds.27140 (cit. on p. 11).

[29] M. Thomsen, L. M. Lange, M. Zech, and K. Lohmann. «Genetics and Pathogenesis of Dystonia». In: *Annual Review of Pathology: Mechanisms of Disease* 19 (2024), pp. 99–131. DOI: 10.1146/annurev-pathmechdis-051122-110756 (cit. on pp. 12, 13, 16–18).

[30] D. Dressler, E. Altenmüller, R. Giess, J. K. Krauss, and F. Adib Saberi. «The epidemiology of dystonia: the Hannover epidemiology study». In: *J Neurol* 269.12 (2022), pp. 6483–6493. DOI: 10.1007/s00415-022-11310-9 (cit. on p. 12).

[31] A. Medina, C. Nilles, D. Martino, C. Pelletier, and T. Pringsheim. «The Prevalence of Idiopathic or Inherited Isolated Dystonia: A Systematic Review and Meta-Analysis». In: *Mov Disord Clin Pract* 9.7 (2022), pp. 860–868. DOI: 10.1002/mdc3.13524 (cit. on p. 12).

[32] T. D. Steeves, L. Day, J. Dykeman, N. Jette, and T. Pringsheim. «The prevalence of primary dystonia: a systematic review and meta-analysis». In: *Mov Disord* 27.14 (2012), pp. 1789–1796. DOI: 10.1002/mds.25244 (cit. on p. 12).

[33] C. D. Stephen. «The Dystonias». In: *Continuum (Minneapolis, Minn)* 28.5 (2022), p. 1435. DOI: 10.1212/CON.0000000000001159 (cit. on pp. 12, 15–17, 20).

[34] M. R. DeLong. «Primate models of movement disorders of basal ganglia origin». In: *Trends in Neurosciences* 13.7 (1990), pp. 281–285. DOI: 10.1016/0166-2236(90)90110-v (cit. on p. 12).

[35] V. K. Neychev, R. E. Gross, S. Lehéricy, E. J. Hess, and H. A. Jinnah. «The functional neuroanatomy of dystonia». In: *Neurobiology of Disease* 42.2 (2011), pp. 185–201. DOI: 10.1016/j.nbd.2011.01.026 (cit. on p. 13).

[36] H. A. Jinnah, V. Neychev, and E. J. Hess. «The Anatomical Basis for Dystonia: The Motor Network Model». In: *Tremor and Other Hyperkinetic Movements* 7 (2017), p. 506. DOI: 10.7916/D8V69X3S (cit. on p. 13).

[37] K. L. Poston and D. Eidelberg. «Functional brain networks and abnormal connectivity in the movement disorders». In: *Neuroimage* 62.4 (2012), pp. 2261–2270. DOI: 10.1016/j.neuroimage.2011.12.021 (cit. on p. 13).

[38] J. L. Lanciego, N. Luquin, and J. A. Obeso. «Functional neuroanatomy of the basal ganglia». In: *Cold Spring Harb Perspect Med* 2.12 (2012), a009621. DOI: 10.1101/cshperspect.a009621 (cit. on p. 13).

[39] M. A. Stacy. *Handbook of Dystonia*. 2006. DOI: 10.1212/Wnl.47.1.313-b (cit. on pp. 13, 14).

[40] A. Fazl and J. Fleisher. «Anatomy, Physiology, and Clinical Syndromes of the Basal Ganglia: A Brief Review». In: *Seminars in Pediatric Neurology* 25 (2018), pp. 2–9. DOI: 10.1016/j.spen.2017.12.005 (cit. on pp. 14, 15).

[41] A. Nambu, H. Tokuno, and M. Takada. «Functional significance of the cortico-subthalamo-pallidal "hyperdirect" pathway». In: *Neuroscience Research* 43.2 (2002), pp. 111–117. DOI: 10.1016/s0168-0102(02)00027-5 (cit. on p. 15).

[42] J Koptielow, E Szyłak, O Szewczyk-Roszczenko, et al. «Genetic Update and Treatment for Dystonia». In: *International Journal of Molecular Sciences* 25.7 (2024), p. 3571. DOI: 10.3390/ijms25073571 (cit. on p. 19).

[43] A. Batla. «Dystonia: A review». In: *Neurology India* 66.Suppl 1 (2018), S48. DOI: 10.4103/0028-3886.226439 (cit. on p. 15).

[44] J. Rosset-Llobet, S. Fàbregas-Molas, and A. Pascual-Leone. «Transcranial direct current stimulation improves neurorehabilitation of task-specific dystonia: a pilot study». In: *Medical Problems of Performing Artists* 29.1 (2014), pp. 16–18. DOI: 10.21091/mppa.2014.1004 (cit. on p. 17).

[45] J.L. Pool. «Psychosurgery in older people». In: *J Am Geriatr Soc* 2.7 (1954), pp. 456–466. DOI: 10.1111/j.1532-5415.1954.tb02138.x (cit. on pp. 21, 22).

[46] A. Fasano, C.C. Aquino, J.K. Krauss, C.R. Honey, and B.R. Bloem. «Axial disability and deep brain stimulation in patients with Parkinson disease». In: *Nat Rev Neurol* 11.2 (2015), pp. 98–110. DOI: 10.1038/nrneurol.2014.252 (cit. on p. 21).

[47] E. Moro, C. LeReun, J.K. Krauss, et al. «Efficacy of pallidal stimulation in isolated dystonia: a systematic review and meta-analysis». In: *Eur J Neurol* 24.4 (2017), pp. 552–560. DOI: 10.1111/ene.13255 (cit. on p. 21).

[48] P. Limousin and T. Foltynie. «Long-term outcomes of deep brain stimulation in Parkinson disease». In: *Nat Rev Neurol* 15.4 (2019), pp. 234–242. DOI: 10.1038/s41582-019-0145-9 (cit. on p. 21).

[49] D. Fontaine, C. Vandersteen, D. Magis, and M. Lanteri-Minet. «Neuromodulation in cluster headache». In: *Adv Tech Stand Neurosurg* 42 (2015), pp. 3–21. DOI: 10.1007/978-3-319-09066-5_1 (cit. on p. 21).

[50] E.A.C. Pereira and T.Z. Aziz. «Neuropathic pain and deep brain stimulation». In: *Neurotherapeutics* 11.3 (2014), pp. 496–507. DOI: 10.1007/s13311-014-0278-x (cit. on p. 21).

[51] D.J. Lee, C.S. Lozano, R.F. Dallapiazza, and A.M. Lozano. «Current and future directions of deep brain stimulation for neurological and psychiatric disorders». In: *J Neurosurg* 131.2 (2019), pp. 333–342. DOI: 10.3171/2019.4.JNS181761 (cit. on p. 21).

[52] I.E. Harmsen, G.J.B. Elias, M.E. Beyn, et al. «Clinical trials for deep brain stimulation: Current state of affairs». In: *Brain Stimulation: Basic, Translational, and Clinical Research in Neuromodulation* 13.2 (2020), pp. 378–385. DOI: 10.1016/j.brs.2019.11.008 (cit. on p. 21).

[53] F. Steigerwald, L. Müller, S. Johannes, C. Matthies, and J. Volkmann. «Directional deep brain stimulation of the subthalamic nucleus: A pilot study using a novel neurostimulation device». In: *Mov Disord* 31.8 (2016), pp. 1240–1243. DOI: 10.1002/mds.26669 (cit. on p. 21).

[54] J. Frey, J. Cagle, K. A. Johnson, J. K. Wong, J. D. Hilliard, C. R. Butson, M. S. Okun, and C. de Hemptinne. «Past, Present, and Future of Deep Brain Stimulation: Hardware, Software, Imaging, Physiology and Novel Approaches». In: *Frontiers in Neurology* 13 (Mar. 2022). Section: Movement Disorders, Part of the Research Topic: Horizons in Neurology. DOI: 10.3389/fneur.2022.825178 (cit. on pp. 21, 28, 29).

[55] V. A. Sironi. «Origin and Evolution of Deep Brain Stimulation». In: *Frontiers in Integrative Neuroscience* 5 (Aug. 2011), p. 42. DOI: 10.3389/fnint.2011.00042 (cit. on p. 21).

[56] J. K. Krauss et al. «Technology of deep brain stimulation: current status and future directions». In: *Nature Reviews Neurology* 17.2 (Nov. 2020), pp. 75–87. DOI: 10.1038/s41582-020-00426-z (cit. on pp. 21, 23, 26, 27, 30).

[57] M. I. Hariz, P. Blomstedt, and L. Zrinzo. «Deep brain stimulation between 1947 and 1987: the untold story». In: *Neurosurg Focus* 29.E1 (2010). DOI: 10.3171/2010.4.FOCUS10106. URL: https://doi.org/10.3171/2010.4.FOCUS10106 (cit. on p. 21).

[58] A. Cohen-Gadol. *Stereotactic Brain Biopsy*. Accessed: February 7, 2025. n.d. URL: https://www.aaroncohen-gadol.com/en/patients/stereotactic-brain-biopsy (cit. on p. 22).

[59] G. Mazars, L. Mérienne, and C. Cioloca. «Use of thalamic stimulators in the treatment of various types of pain [French]». In: *Ann Med Interne* 126 (1975), pp. 869–871 (cit. on p. 22).

[60] Y. Hosobuchi, J.E. Adams, and B. Rutkin. «Chronic thalamic stimulation for the control of facial anesthesia dolorosa». In: *Arch Neurol* 29 (1973), pp. 158–161. DOI: 10.1001/archneur.1973.00490270040005 (cit. on p. 22).

[61] J. Gardner. «A history of deep brain stimulation: technological innovation and the role of clinical assessment tools». In: *Soc Stud Sci* 43 (2013), pp. 707–728. DOI: 10.1177/0306312713483678 (cit. on p. 22).

[62] A. L. Benabid, P. Pollak, A. Louveau, S. Henry, and J. de Rougemont. «Combined (thalamotomy and stimulation) stereotactic surgery of the VIM thalamic nucleus for bilateral Parkinson disease». In: *Appl Neurophysiol* 50 (1987), pp. 344–346. DOI: 10.1159/000100803 (cit. on p. 22).

[63] A. Sarem-Aslani and K. Mullett. «Industrial perspective on deep brain stimulation: history, current state, and future developments». In: *Front Integr Neurosci* 5 (2011), p. 46. DOI: 10.3389/fnint.2011.00046 (cit. on p. 23).

[64] T. M. Herrington, J. J. Cheng, and E. N. Eskandar. «Mechanisms of deep brain stimulation». In: *J Neurophysiol* 115 (2016), pp. 19–38. DOI: 10.1152/jn.00281.2015 (cit. on p. 23).

[65] J. Whitestone, A. Salih, and T. Goswami. «Investigation of a Deep Brain Stimulator (DBS) System». In: *Bioengineering* 10.10 (2023), p. 1160. DOI: 10.3390/bioengineering10101160 (cit. on pp. 24, 28).

[66] C. Sarica et al. «Implantable Pulse Generators for Deep Brain Stimulation: Challenges, Complications, and Strategies for Practicality and Longevity». In: *Frontiers in Human Neuroscience* 15 (2021). This article is part of the Research Topic "Deep Brain Stimulation Think Tank: Updates in Neurotechnology and Neuromodulation, Volume II", p. 708481. DOI: 10.3389/fnhum.2021.708481. URL: https://doi.org/10.3389/fnhum.2021.708481 (cit. on pp. 24, 25).

[67] J.M. Bronstein et al. «The rationale driving the evolution of deep brain stimulation to constant-current devices». In: *Neuromodulation* 18.2 (2015), pp. 85–88. DOI: 10.1111/ner.12227 (cit. on p. 26).

[68] H.A.M. Ali, S.S. Abdullah, and M. Faraj. «An In-Vitro Study of Electrodes Impedance in Deep Brain Stimulation». In: *Journal of Physics: Conference Series* 1829.1 (2021), p. 012019. DOI: 10.1088/1742-6596/1829/1/012019 (cit. on p. 27).

[69] T. Goswami, M. Markl, and R.J. Guthrie. «Investigation of A Neuro-Stimulator Retrieved Posthumously». In: *Biomedical Journal of Scientific and Technical Research* 23 (2019), pp. 17522–17527. DOI: 10.26717/BJSTR.2019.23.003923 (cit. on p. 28).

[70] C. Nurimanov, I. Mammadinova, K. Menlibayeva, and S. Aidarov. «Managing Lead Fractures in Deep Brain Stimulation for Movement Disorders: A Decade-Long Case Series from a National Neurosurgical Centre». In: *Journal of Clinical Medicine* 13.24 (Dec. 2024), p. 7509. DOI: 10.3390/jcm13247509 (cit. on p. 30).

[71] A.A. Mohamed, S. Faragalla, A. Khan, et al. «Neurosurgical and pharmacological management of dystonia». In: *World Journal of Psychiatry* 14.5 (2024), pp. 624–634. DOI: 10.5498/wjp.v14.i5.624 (cit. on p. 29).

[72] M. L . F. Janssen and M. J. Bos. «Microelectrode assisted deep brain stimulation: Considerations for anesthesia». In: *Deep Brain Stimulation* 4 (June 2024), pp. 13–23. DOI: 10.1016/j.jdbs.2023.12.006 (cit. on p. 31).

[73] C. S. Lozano, M. Ranjan, A. Boutet, D. S. Xu, W. Kucharczyk, et al. «Imaging alone versus microelectrode recording-guided targeting of the STN in patients with Parkinson's disease». In: *J Neurosurg* 130.6 (Aug. 2018), pp. 1847–1852. DOI: 10.3171/2018.2.JNS172186 (cit. on p. 31).

[74] A. Izzo et al. «Intraoperative microelectrode recording during asleep deep brain stimulation of subthalamic nucleus for Parkinson Disease. A case series with systematic review of the literature». In: *Neurosurgical Review* 47.1 (2024), p. 342. DOI: 10.1007/s10143-024-02563-1 (cit. on p. 31).

[75] E. B. Montgomery Jr. *Intraoperative Neurophysiological Monitoring for Deep Brain Stimulation: Principles, Practice and Cases*. Published online: August 2014, Published in print: July 2014. Oxford University Press, 2014. DOI: 10.1093/med/9780199351008.001.0001 (cit. on pp. 31, 34–36, 38, 39, 55).

[76] C. R. Camalier, P. Konrad, C. E. Gill, and C. Kao. «Methods for Surgical Targeting of the STN in Early-Stage Parkinson's Disease». In: *Frontiers in Neurology* 5 (Mar. 2014), p. 25. DOI: 10.3389/fneur.2014.00025 (cit. on p. 32).

[77] S. Bus, G. Pal, B. Ouyang, P. van den Munckhof, M. Bot, S. Sani, and L. Verhagen Metman. «Accuracy of Microelectrode Trajectory Adjustments during DBS Assessed by Intraoperative CT». In: *Stereotact Funct Neurosurg* 96.4 (2018), pp. 231–238. DOI: 10.1159/000489945 (cit. on p. 38).

[78] inomed. *MicroDrive for Functional Neurosurgery*. Accessed: 2024-02-09. 2024. URL: https://www.en.inomed.com/products/functional-neurosurgery/microdrive/ (cit. on p. 39).

[79] N. Ahmadi, T. G. Constandinou, and C. S. Bouganis. «Inferring entire spiking activity from local field potentials». In: *Scientific Reports* 11 (Sept. 2021), p. 19045. DOI: 10.1038/s41598-021-98349-1 (cit. on p. 38).

[80] H. Supèr and P. R. Roelfsema. «Chronic multiunit recordings in behaving animals: advantages and limitations». In: *Progress in Brain Research* 147 (2005), pp. 263–282. DOI: 10.1016/S0079-6123(04)47020-4 (cit. on p. 38).

[81] A. Al Awadhi, R. Tyrand, A. Horn, A. Kibleur, J. Vincentini, A. Zacharia, P. R. Burkhard, S. Momjian, and C. Boëx. «Electrophysiological confrontation of Lead-DBS-based electrode localizations in patients with Parkinson's disease undergoing deep brain stimulation». In: *NeuroImage: Clinical* 34 (Feb. 2022), p. 102971. DOI: 10.1016/j.nicl.2022.102971 (cit. on pp. 39, 56).

[82] A. E. L. Warren, L. J. Dalic, W. Thevathasan, A. Roten, K. J. Bulluss, and J. Archer. «Targeting the centromedian thalamic nucleus for deep brain stimulation». In: *Journal of Neurology, Neurosurgery and Psychiatry* 91.4 (Apr. 2020), pp. 339–349. DOI: 10.1136/jnnp-2019-322030 (cit. on pp. 39, 56).

[83] F. I. Alanazi, T. M. Al-Ozzi, S. K. Kalia, M. Hodaie, A. M. Lozano, M. Cohn, and W. D. Hutchison. «Neurophysiological responses of globus pallidus internus during the auditory oddball task in Parkinson's disease». In: *Neurobiology of Disease* 159 (Nov. 2021), p. 105490. DOI: 10.1016/j.nbd.2021.105490 (cit. on pp. 39, 92).

[84] N. Maling and C. McIntyre. «Local Field Potential Analysis for Closed-Loop Neuromodulation». In: *Closed Loop Neuroscience*. Academic Press, Dec. 2016, pp. 67–80. DOI: 10.1016/B978-0-12-802452-2.00005-6 (cit. on p. 39).

[85] A. Shmuel and A. Maier. «Locally Measured Neuronal Correlates of Functional MRI Signals». In: *Biological Magnetic Resonance*. Springer, 2015, pp. 105–128. DOI: 10.1007/978-1-4899-7591-1_6 (cit. on p. 40).

[86] H. G. Rey, C. Pedreira, and R. Quian Quiroga. «Past, present and future of spike sorting techniques». In: *Brain Research Bulletin* 119.Part B (2015), pp. 106–117. DOI: 10.1016/j.brainresbull.2015.04.007 (cit. on pp. 40, 41).

[87] R. Quian Quiroga, Z. Nadasdy, and Y. Ben-Shaul. «Unsupervised spike detection and sorting with wavelets and superparamagnetic clustering». In: *Neural Computation* 16.8 (Aug. 2004), pp. 1661–1687. DOI: 10.1162/089976604774201631 (cit. on pp. 42, 56).

[88] H. Hotelling. «Analysis of a complex of statistical variables into principal components». In: *Journal of Educational Psychology* 24 (1933), pp. 417–441. DOI: 10.1037/h0071325 (cit. on p. 43).

[89] S. Madala. *Principal Component Analysis (PCA)*. Online. [Accessed 29 July 2024]. Jan. 2023. URL: https://www.scaler.com/topics/nlp/what-is-pca/ (cit. on p. 43).

[90] R. Bestel, A. W. Daus, and C. Thielemann. «A novel automated spike sorting algorithm with adaptable feature extraction». In: *Journal of Neuroscience Methods* 211 (2012), pp. 168–178. DOI: 10.1016/j.jneumeth.2012.08.023 (cit. on p. 44).

[91] J. B. MacQueen. «Some methods for classification and analysis of multivariate observations». In: *Proceedings of the 5th Berkeley Symposium on Mathematical Statistics and Probability*. Vol. 1. Berkeley: University of California Press, 1967, pp. 281–297 (cit. on p. 44).

[92] M. Johanna Kuiper et al. «The Burke-Fahn-Marsden Dystonia Rating Scale is age-dependent in healthy children». In: *Movement Disorders Clinical Practice* 3.6 (2016), pp. 580–586. DOI: 10.1002/mdc3.12339 (cit. on p. 48).

[93] Medtronic. *Medtronic Italia*. https://www.medtronic.com/it-it/index.html. Accessed: 2025-01-12 (cit. on p. 48).

[94] NeuroSmart. *NeuroSmart*. https://www.alphaomega-eng.com/NeuroSmart2. Accessed: 2025-01-15 (cit. on p. 48).

[95] The MathWorks Inc. *MATLAB*. Version 2024a. Natick, Massachusetts, 2024 (cit. on p. 50).

[96] N. Koirala, L. Serrano, S. Paschen, D. Falk, A. R. Anwar, P. Kuravi, G. Deuschl, S. Groppa, and M. Muthuraman. «Mapping of subthalamic nucleus using microelectrode recordings during deep brain stimulation». In: *Scientific Reports* 10 (Nov. 2020), p. 19241. DOI: 10.1038/s41598-020-76105-0 (cit. on p. 55).

[97] R. Toosi, M. A. Akhaee, and M. R. A. Dehaqani. «An automatic spike sorting algorithm based on adaptive spike detection and a mixture of skew-t distributions». In: *Scientific Reports* 11 (July 2021), p. 13925. DOI: 10.1038/s41598-021-93134-1 (cit. on pp. 55, 57).

[98] E. Keogh and A. Mueen. «Curse of Dimensionality». In: *Encyclopedia of Machine Learning and Data Mining*. Ed. by Claude Sammut and Geoffrey I. Webb. Boston, MA: Springer, 2017. DOI: 10.1007/978-1-4899-7687-1_192 (cit. on p. 57).

[99] R. Tibshirani, G. Walther, and T. Hastie. «Estimating the number of clusters in a data set via the Gap statistic». In: *Journal of the Royal Statistical Society: Series B (Statistical Methodology)* 63.2 (2001), pp. 411–423. DOI: 10.1111/1467-9868.00293 (cit. on p. 58).

[100] C. Pedreira, J. Martinez, M. J. Ison, and R. Quian Quiroga. «How many neurons can we see with current spike sorting algorithms?» In: *Journal of Neuroscience Methods* 211.1 (2012), pp. 58–65. DOI: 10.1016/j.jneumeth.2012.07.010 (cit. on p. 60).

[101] C. Pouzat. *An experimental illustration from projection neurons in the locust antennal lobe*. Les Houches, Course 15 - Technique(s) for Spike-Sorting. 2005 (cit. on p. 62).

[102] N.J. Hall, D.J. Herzfeld, and S.G. Lisberger. «Evaluation and resolution of many challenges of neural spike sorting: a new sorter». In: *J Neurophysiol* 126.6 (2021), pp. 1900–1912. DOI: 10.1152/jn.00047.2021 (cit. on p. 63).

[103] A. Kaymak et al. «Patterns of neural activity and clinical outcomes in a juvenile Huntington's Disease patient undergoing Deep Brain Stimulation of the subthalamic nucleus». In: *Deep Brain Stimul* 1 (2023), pp. 15–19. DOI: 10.1016/j.jdbs.2023.05.004 (cit. on p. 64).

[104] W. Chaovalitwongse, Y. Jeong, M.K. Jeong, S. Danish, and S. Wong. «Pattern recognition approaches for identifying subcortical targets during deep brain stimulation surgery». In: *IEEE Intell Syst* 26.5 (2011), pp. 37–44. DOI: 10.1109/MIS.2011.39 (cit. on p. 64).

[105] Y. Mochizuki, T. Onaga, H. Shimazaki, et al. «Similarity in neuronal firing regimes across mammalian species». In: *J Neurosci* 36.21 (2016), pp. 5736–5747. DOI: 10.1523/JNEUROSCI.0230-16.2016 (cit. on p. 64).

[106] M. Vissani and et al. «Spatio-temporal structure of single neuron subthalamic activity identifies DBS target for anesthetized Tourette syndrome patients». In: *Journal of Neural Engineering* 16 (2019), p. 066011 (cit. on p. 64).

[107] J. Lengler and A. Steger. «Note on the coefficient of variations of neuronal spike trains». In: *Biological Cybernetics* 111.3 (2017), pp. 229–235 (cit. on p. 65).

[108] S. Shinomoto, K. Shima, and J. Tanji. «Differences in spiking patterns among cortical neurons». In: *Neural Computation* 15.12 (2003), pp. 2823–2842. DOI: 10.1162/089976603322518759 (cit. on p. 65).

[109] W. D. Hutchison, A. E. Lang, J. O. Dostrovsky, and A. M. Lozano. «Pallidal neuronal activity: Implications for models of dystonia». In: *Annals of Neurology* 53.4 (2003), pp. 480–488. DOI: 10.1002/ana.10534 (cit. on p. 66).

[110] W. D. Hutchison, R. Levy, J. O. Dostrovsky, A. M. Lozano, and A. E. Lang. «Effects of apomorphine on globus pallidus neurons in parkinsonian patients». In: *Annals of Neurology* 42.5 (1997), pp. 767–775. DOI: 10.1002/ana.410420516 (cit. on p. 66).

[111] B. Gourévitch and J. J. Eggermont. «A nonparametric approach for detection of bursts in spike trains». In: *Journal of Neuroscience Methods* 160.2 (2007), pp. 349–358. DOI: 10.1016/j.jneumeth.2006.09.024 (cit. on p. 66).

[112] C. S. Herrmann, M. M. Murray, S. Ionta, A. Hutt, and J. Lefebvre. «Shaping intrinsic neural oscillations with periodic stimulation». In: *Journal of Neuroscience* 36.19 (2016), pp. 5328–5337. DOI: 10.1523/JNEUROSCI.0236-16.2016 (cit. on p. 69).

[113] A. Zaidel, A. Spivak, L. Shpigelman, H. Bergman, and Z. Israel. «Delimiting subterritories of the human subthalamic nucleus by means of microelectrode recordings and a hidden Markov model». In: *Movement Disorders* 24.12 (2009), pp. 1785–1793. DOI: 10.1002/mds.22685 (cit. on p. 69).

[114] A. Zaidel, A. Spivak, B. Grieb, H. Bergman, and Z. Israel. «Subthalamic span of beta oscillations predicts deep brain stimulation efficacy for patients with Parkinson's disease». In: *Brain* 133.7 (2010), pp. 2007–2021. DOI: 10.1093/brain/awq144 (cit. on p. 69).

[115] D. Sirica, A. L. Hewitt, C. G. Tarolli, M. T. Weber, C. Zimmerman, A. Santiago, and et al. «Neurophysiological biomarkers to optimize deep brain stimulation in movement disorders». In: *Neurodegenerative Disease Management* 11.4 (2021), pp. 315–328. DOI: 10.2217/nmt-2021-0002 (cit. on p. 69).

[116] A. Tepper, M. C. Henrich, L. Schiaffino, A. Rosado Muñoz, A. Gutiérrez, and J. Guerrero Martínez. «Selection of the optimal algorithm for real-time estimation of beta band power during DBS surgeries in patients with Parkinson's disease». In: *Computer Intelligence in Neuroscience* 2017 (2017), p. 1512504. DOI: 10.1155/2017/1512504 (cit. on p. 70).

[117] A. Moran and I. Bar-Gad. «Revealing neuronal functional organization through the relation between multi-scale oscillatory extracellular signals». In: *Journal of Neuroscience Methods* 184.2 (2009), pp. 182–196. DOI: 10.1016/j.jneumeth.2009.10.024 (cit. on p. 70).

[118] A. Moran, H. Bergman, Z. Israel, and I. Bar-Gad. «Subthalamic nucleus functional organization revealed by parkinsonian neuronal oscillations and synchrony». In: *Brain* 131.12 (2008), pp. 3395–3409 (cit. on p. 71).

[119] M. Khosravi, S. F. Atashzar, G. Gilmore, M. S. Jog, and R. V. Patel. «Intraoperative localization of STN during DBS surgery using a data-driven model». In: *IEEE Journal of Translational Engineering in Health and Medicine* 8 (2020), p. 2500309. DOI: 10.1109/JTEHM.2020.2969152 (cit. on p. 71).

[120] S. Wong, G. H. Baltuch, J. L. Jaggi, and S. F. Danish. «Functional localization and visualization of the subthalamic nucleus from microelectrode recordings acquired during DBS surgery with unsupervised machine learning». In: *Journal of Neural Engineering* 6.2 (2009), p. 026006. DOI: 10.1088/1741-2560/6/2/026006 (cit. on p. 71).

[121] L. J. Bour, M. F. Contarino, E. M. J. Foncke, R. M. A. de Bie, P. van den Munckhof, J. D. Speelman, and P. R. Schuurman. «Long-term experience with intraoperative microrecording during DBS neurosurgery in STN and GPi». In: *Acta Neurochirurgica (Wien)* 152.12 (2010), pp. 2069–2077. DOI: 10.1007/s00701-010-0835-y (cit. on pp. 74, 91–93).

[122] A. Giorni, F. Windels, P. G. Stratton, R. Cook, P. Silberstein, T. Coyne, P. A. Silburn, and P. Sah. «Single-unit activity of the anterior globus pallidus internus in Tourette patients and posterior globus pallidus internus in Dystonic patients». In: *Clinical Neurophysiology* (2017). DOI: 10.1016/j.clinph.2017.10.003 (cit. on pp. 74, 92).

[123] S. Tisch, L. Zrinzo, P. Limousin, K. P. Bhatia, N. Quinn, K. Ashkan, and M. Hariz. «Effect of electrode contact location on clinical efficacy of pallidal deep brain stimulation in primary generalised dystonia». In: *Journal of Neurology, Neurosurgery & Psychiatry* 78.12 (2007), pp. 1314–1319. DOI: 10.1136/jnnp.2006.109694 (cit. on pp. 74, 92).

[124] E. H. Middlebrooks, I. S. Tuna, S. S. Grewal, L. Almeida, M. G. Heckman, E. R. Lesser, and et al. «Segmentation of the globus pallidus internus using probabilistic diffusion tractography for deep brain stimulation targeting in Parkinson disease». In: *AJNR American Journal of Neuroradiology* 39.6 (2018), pp. 1127–1134. DOI: 10.3174/ajnr.A5641 (cit. on pp. 74, 92).

[125] H. W. Lilliefors. «On the Kolmogorov-Smirnov test for normality with mean and variance unknown». In: *Journal of the American Statistical Association* 62.318 (1967), pp. 399–402. DOI: 10.1080/01621459.1967.10501821 (cit. on p. 75).

[126] Student. «The probable error of a mean». In: *Biometrika* 6.1 (1908), pp. 1–25. DOI: 10.2307/2331554 (cit. on p. 75).

[127] F. Wilcoxon. «Individual comparisons by ranking methods». In: *Biometrics Bulletin* 1.6 (1945), pp. 80–83. DOI: 10.2307/3001968 (cit. on p. 75).

[128] R. L. Plackett. «Karl Pearson and the Chi-Squared Test». In: *International Statistical Review* 51.1 (1983), pp. 59–72. DOI: 10.2307/1402731 (cit. on p. 75).

[129] D. Ledingham, M. Baker, and N. Pavese. «Local field potentials: Therapeutic implications for DBS in dystonia including adaptive DBS for dystonia». In: *Deep Brain Stimulation* 5 (2024). Under a Creative Commons license, pp. 4–19. DOI: 10.1016/j.jdbs.2024.03.003. URL: https://doi.org/10.1016/j.jdbs.2024.03.003 (cit. on pp. 91, 93).

[130] A. Fasano et al. «Local field potential-based programming: A proof-of-concept pilot study». In: *Neuromodulation* 25.2 (2022), pp. 271–275. DOI: 10.1111/ner.13520 (cit. on p. 91).

[131] C. K. E. Moll et al. «Asymmetric pallidal neuronal activity in patients with cervical dystonia». In: *Frontiers in Systems Neuroscience* 8 (2014), p. 15. DOI: 10.3389/fnsys.2014.00015 (cit. on pp. 91, 92).

[132] F. Yokochi et al. «Resting-State Pallidal-Cortical Oscillatory Couplings in Patients With Predominant Phasic and Tonic Dystonia». In: *Frontiers in Neurology* 9 (2018). Sec. Movement Disorders. DOI: 10.3389/fneur.2018.00375. URL: https://doi.org/10.3389/fneur.2018.00375 (cit. on p. 92).

[133] Y. Guo, C. Park, R. M. Worth, and L. L. Rubchinsky. «Basal ganglia modulation of thalamocortical relay in Parkinson's disease and dystonia». In: *Frontiers in Computational Neuroscience* 7 (2013), p. 124. DOI: 10.3389/fncom.2013.00124 (cit. on p. 92).

[134] A. Sedov, V. Popov, A. Gamaleya, U. Semenova, A. Tomskiy, H.A. Jinnah, and A.G. Shaikh. «Pallidal neuron activity determines responsiveness to deep brain stimulation in cervical dystonia». In: *Clinical Neurophysiology* 132.12 (2021). Author manuscript available in PMC: 2022 Dec 1, pp. 3190–3196. DOI: 10.1016/j.clinph.2021.07.032 (cit. on p. 92).

[135] M. Baláž, J. Búřil, T. Jurková, E. Koriťáková, D. Hrabovský, J. Kunst, P. Bártová, and J. Chrastina. «Intraoperative electrophysiological monitoring determines the final electrode position for pallidal stimulation in dystonia patients». In: *Frontiers in Surgery* 10 (2023), p. 1206721. DOI: 10.3389/fsurg.2023.1206721 (cit. on p. 92).

[136] J.K.H. Tang, E. Moro, N. Mahant, W.D. Hutchison, A.E. Lang, A.M. Lozano, and J.O. Dostrovsky. «Neuronal firing rates and patterns in the globus pallidus internus of patients with cervical dystonia differ from those with Parkinson's disease». In: *Journal of Neurophysiology* 98.2 (2007), pp. 720–729. DOI: 10.1152/jn.01107.2006 (cit. on p. 93).

[137] J.L. Vitek et al. «Neuronal activity in the basal ganglia in patients with generalized dystonia and hemiballismus». In: *Annals of Neurology* 46.1 (1999), pp. 22–35. DOI: 10.1002/1531-8249(199907)46:1<22::aid-ana6>3.0.co;2-z (cit. on p. 93).

[138] P. Zhuang, Y. Li, and M. Hallett. «Neuronal activity in the basal ganglia and thalamus in patients with dystonia». In: *Clinical Neurophysiology* 115.11 (2004), pp. 2542–2557. DOI: 10.1016/j.clinph.2004.06.006 (cit. on p. 93).